EUROPEAN LABORATORY FOR PARTICLE PHYSICS

CERN-PPE/97-101
29th July 1997

Tests of the Standard Model and Constraints on New Physics from Measurements of Fermion-pair Production at 130–172 GeV at LEP

The OPAL Collaboration

Abstract

Production of events with hadronic and leptonic final states has been measured in e^+e^- collisions at centre-of-mass energies of 130–172 GeV, using the OPAL detector at LEP. Cross-sections and leptonic forward-backward asymmetries are presented, both including and excluding the dominant production of radiative $Z\gamma$ events, and compared to Standard Model expectations. The ratio R_b of the cross-section for $b\bar{b}$ production to the hadronic cross-section has been measured. In a model-independent fit to the Z lineshape, the data have been used to obtain an improved precision on the measurement of γ-Z interference. The energy dependence of α_{em} has been investigated. The measurements have also been used to obtain limits on extensions of the Standard Model described by effective four-fermion contact interactions, to search for t-channel contributions from new massive particles and to place limits on chargino pair production with subsequent decay of the chargino into a light gluino and a quark pair.

Submitted to Z. Phys. C

The OPAL Collaboration

K. Ackerstaff[8], G. Alexander[23], J. Allison[16], N. Altekamp[5], K.J. Anderson[9], S. Anderson[12], S. Arcelli[2], S. Asai[24], D. Axen[29], G. Azuelos[18,a], A.H. Ball[17], E. Barberio[8], R.J. Barlow[16], R. Bartoldus[3], J.R. Batley[5], S. Baumann[3], J. Bechtluft[14], C. Beeston[16], T. Behnke[8], A.N. Bell[1], K.W. Bell[20], G. Bella[23], S. Bentvelsen[8], S. Bethke[14], O. Biebel[14], A. Biguzzi[5], S.D. Bird[16], V. Blobel[27], I.J. Bloodworth[1], J.E. Bloomer[1], M. Bobinski[10], P. Bock[11], D. Bonacorsi[2], M. Boutemeur[34], B.T. Bouwens[12], S. Braibant[12], L. Brigliadori[2], R.M. Brown[20], H.J. Burckhart[8], C. Burgard[8], R. Bürgin[10], P. Capiluppi[2], R.K. Carnegie[6], A.A. Carter[13], J.R. Carter[5], C.Y. Chang[17], D.G. Charlton[1,b], D. Chrisman[4], P.E.L. Clarke[15], I. Cohen[23], J.E. Conboy[15], O.C. Cooke[8], M. Cuffiani[2], S. Dado[22], C. Dallapiccola[17], G.M. Dallavalle[2], R. Davis[30], S. De Jong[12], L.A. del Pozo[4], K. Desch[3], B. Dienes[33,d], M.S. Dixit[7], E. do Couto e Silva[12], M. Doucet[18], E. Duchovni[26], G. Duckeck[34], I.P. Duerdoth[16], D. Eatough[16], J.E.G. Edwards[16], P.G. Estabrooks[6], H.G. Evans[9], M. Evans[13], F. Fabbri[2], M. Fanti[2], A.A. Faust[30], F. Fiedler[27], M. Fierro[2], H.M. Fischer[3], I. Fleck[8], R. Folman[26], D.G. Fong[17], M. Foucher[17], A. Fürtjes[8], D.I. Futyan[16], P. Gagnon[7], J.W. Gary[4], J. Gascon[18], S.M. Gascon-Shotkin[17], N.I. Geddes[20], C. Geich-Gimbel[3], T. Geralis[20], G. Giacomelli[2], P. Giacomelli[4], R. Giacomelli[2], V. Gibson[5], W.R. Gibson[13], D.M. Gingrich[30,a], D. Glenzinski[9], J. Goldberg[22], M.J. Goodrick[5], W. Gorn[4], C. Grandi[2], E. Gross[26], J. Grunhaus[23], M. Gruwé[8], C. Hajdu[32], G.G. Hanson[12], M. Hansroul[8], M. Hapke[13], C.K. Hargrove[7], P.A. Hart[9], C. Hartmann[3], M. Hauschild[8], C.M. Hawkes[5], R. Hawkings[27], R.J. Hemingway[6], M. Herndon[17], G. Herten[10], R.D. Heuer[8], M.D. Hildreth[8], J.C. Hill[5], S.J. Hillier[1], P.R. Hobson[25], R.J. Homer[1], A.K. Honma[28,a], D. Horváth[32,c], K.R. Hossain[30], R. Howard[29], P. Hüntemeyer[27], D.E. Hutchcroft[5], P. Igo-Kemenes[11], D.C. Imrie[25], M.R. Ingram[16], K. Ishii[24], A. Jawahery[17], P.W. Jeffreys[20], H. Jeremie[18], M. Jimack[1], A. Joly[18], C.R. Jones[5], G. Jones[16], M. Jones[6], U. Jost[11], P. Jovanovic[1], T.R. Junk[8], D. Karlen[6], V. Kartvelishvili[16], K. Kawagoe[24], T. Kawamoto[24], P.I. Kayal[30], R.K. Keeler[28], R.G. Kellogg[17], B.W. Kennedy[20], J. Kirk[29], A. Klier[26], S. Kluth[8], T. Kobayashi[24], M. Kobel[10], D.S. Koetke[6], T.P. Kokott[3], M. Kolrep[10], S. Komamiya[24], T. Kress[11], P. Krieger[6], J. von Krogh[11], P. Kyberd[13], G.D. Lafferty[16], R. Lahmann[17], W.P. Lai[19], D. Lanske[14], J. Lauber[15], S.R. Lautenschlager[31], J.G. Layter[4], D. Lazic[22], A.M. Lee[31], E. Lefebvre[18], D. Lellouch[26], J. Letts[12], L. Levinson[26], S.L. Lloyd[13], F.K. Loebinger[16], G.D. Long[28], M.J. Losty[7], J. Ludwig[10], A. Macchiolo[2], A. Macpherson[30], M. Mannelli[8], S. Marcellini[2], C. Markus[3], A.J. Martin[13], J.P. Martin[18], G. Martinez[17], T. Mashimo[24], P. Mättig[3], W.J. McDonald[30], J. McKenna[29], E.A. Mckigney[15], T.J. McMahon[1], R.A. McPherson[8], F. Meijers[8], S. Menke[3], F.S. Merritt[9], H. Mes[7], J. Meyer[27], A. Michelini[2], G. Mikenberg[26], D.J. Miller[15], A. Mincer[22,e], R. Mir[26], W. Mohr[10], A. Montanari[2], T. Mori[24], M. Morii[24], U. Müller[3], S. Mihara[24], K. Nagai[26], I. Nakamura[24], H.A. Neal[8], B. Nellen[3], R. Nisius[8], S.W. O'Neale[1], F.G. Oakham[7], F. Odorici[2], H.O. Ogren[12], A. Oh[27], N.J. Oldershaw[16], M.J. Oreglia[9], S. Orito[24], J. Pálinkás[33,d], G. Pásztor[32], J.R. Pater[16], G.N. Patrick[20], J. Patt[10], M.J. Pearce[1], R. Perez-Ochoa[8], S. Petzold[27], P. Pfeifenschneider[14], J.E. Pilcher[9], J. Pinfold[30], D.E. Plane[8], P. Poffenberger[28], B. Poli[2], A. Posthaus[3], D.L. Rees[1], D. Rigby[1], S. Robertson[28], S.A. Robins[22], N. Rodning[30], J.M. Roney[28], A. Rooke[15], E. Ros[8], A.M. Rossi[2], P. Routenburg[30], Y. Rozen[22], K. Runge[10], O. Runolfsson[8], U. Ruppel[14], D.R. Rust[12], R. Rylko[25], K. Sachs[10], T. Saeki[24], E.K.G. Sarkisyan[23], C. Sbarra[29], A.D. Schaile[34], O. Schaile[34], F. Scharf[3], P. Scharff-Hansen[8], P. Schenk[34], J. Schieck[11], P. Schleper[11], B. Schmitt[8], S. Schmitt[11], A. Schöning[8], M. Schröder[8], H.C. Schultz-Coulon[10], M. Schumacher[3],

C. Schwick[8], W.G. Scott[20], T.G. Shears[16], B.C. Shen[4], C.H. Shepherd-Themistocleous[8], P. Sherwood[15], G.P. Siroli[2], A. Sittler[27], A. Skillman[15], A. Skuja[17], A.M. Smith[8], G.A. Snow[17], R. Sobie[28], S. Söldner-Rembold[10], R.W. Springer[30], M. Sproston[20], K. Stephens[16], J. Steuerer[27], B. Stockhausen[3], K. Stoll[10], D. Strom[19], P. Szymanski[20], R. Tafirout[18], S.D. Talbot[1], S. Tanaka[24], P. Taras[18], S. Tarem[22], R. Teuscher[8], M. Thiergen[10], M.A. Thomson[8], E. von Törne[3], S. Towers[6], I. Trigger[18], Z. Trócsányi[33], E. Tsur[23], A.S. Turcot[9], M.F. Turner-Watson[8], P. Utzat[11], R. Van Kooten[12], M. Verzocchi[10], P. Vikas[18], E.H. Vokurka[16], H. Voss[3], F. Wäckerle[10], A. Wagner[27], C.P. Ward[5], D.R. Ward[5], P.M. Watkins[1], A.T. Watson[1], N.K. Watson[1], P.S. Wells[8], N. Wermes[3], J.S. White[28], B. Wilkens[10], G.W. Wilson[27], J.A. Wilson[1], G. Wolf[26], T.R. Wyatt[16], S. Yamashita[24], G. Yekutieli[26], V. Zacek[18], D. Zer-Zion[8]

[1]School of Physics and Space Research, University of Birmingham, Birmingham B15 2TT, UK
[2]Dipartimento di Fisica dell' Università di Bologna and INFN, I-40126 Bologna, Italy
[3]Physikalisches Institut, Universität Bonn, D-53115 Bonn, Germany
[4]Department of Physics, University of California, Riverside CA 92521, USA
[5]Cavendish Laboratory, Cambridge CB3 0HE, UK
[6] Ottawa-Carleton Institute for Physics, Department of Physics, Carleton University, Ottawa, Ontario K1S 5B6, Canada
[7]Centre for Research in Particle Physics, Carleton University, Ottawa, Ontario K1S 5B6, Canada
[8]CERN, European Organisation for Particle Physics, CH-1211 Geneva 23, Switzerland
[9]Enrico Fermi Institute and Department of Physics, University of Chicago, Chicago IL 60637, USA
[10]Fakultät für Physik, Albert Ludwigs Universität, D-79104 Freiburg, Germany
[11]Physikalisches Institut, Universität Heidelberg, D-69120 Heidelberg, Germany
[12]Indiana University, Department of Physics, Swain Hall West 117, Bloomington IN 47405, USA
[13]Queen Mary and Westfield College, University of London, London E1 4NS, UK
[14]Technische Hochschule Aachen, III Physikalisches Institut, Sommerfeldstrasse 26-28, D-52056 Aachen, Germany
[15]University College London, London WC1E 6BT, UK
[16]Department of Physics, Schuster Laboratory, The University, Manchester M13 9PL, UK
[17]Department of Physics, University of Maryland, College Park, MD 20742, USA
[18]Laboratoire de Physique Nucléaire, Université de Montréal, Montréal, Quebec H3C 3J7, Canada
[19]University of Oregon, Department of Physics, Eugene OR 97403, USA
[20]Rutherford Appleton Laboratory, Chilton, Didcot, Oxfordshire OX11 0QX, UK
[22]Department of Physics, Technion-Israel Institute of Technology, Haifa 32000, Israel
[23]Department of Physics and Astronomy, Tel Aviv University, Tel Aviv 69978, Israel
[24]International Centre for Elementary Particle Physics and Department of Physics, University of Tokyo, Tokyo 113, and Kobe University, Kobe 657, Japan
[25]Brunel University, Uxbridge, Middlesex UB8 3PH, UK
[26]Particle Physics Department, Weizmann Institute of Science, Rehovot 76100, Israel
[27]Universität Hamburg/DESY, II Institut für Experimental Physik, Notkestrasse 85, D-22607 Hamburg, Germany
[28]University of Victoria, Department of Physics, P O Box 3055, Victoria BC V8W 3P6, Canada

[29]University of British Columbia, Department of Physics, Vancouver BC V6T 1Z1, Canada
[30]University of Alberta, Department of Physics, Edmonton AB T6G 2J1, Canada
[31]Duke University, Dept of Physics, Durham, NC 27708-0305, USA
[32]Research Institute for Particle and Nuclear Physics, H-1525 Budapest, P O Box 49, Hungary
[33]Institute of Nuclear Research, H-4001 Debrecen, P O Box 51, Hungary
[34]Ludwigs-Maximilians-Universität München, Sektion Physik, Am Coulombwall 1, D-85748 Garching, Germany

[a] and at TRIUMF, Vancouver, Canada V6T 2A3
[b] and Royal Society University Research Fellow
[c] and Institute of Nuclear Research, Debrecen, Hungary
[d] and Department of Experimental Physics, Lajos Kossuth University, Debrecen, Hungary
[e] and Department of Physics, New York University, NY 1003, USA

1 Introduction

Fermion-pair production in e^+e^- collisions is one of the basic processes of the Standard Model, and deviations of measured cross-sections from the predicted values could be a first indication of new physics beyond the Standard Model. Measurements up to 161 GeV centre-of-mass energy [1, 2] have shown no significant deviations from Standard Model expectations. In this paper we present new measurements of hadronic and leptonic final states in e^+e^- collisions at a centre-of-mass energy $\sqrt{s}$ of 172 GeV, and improved results for the same final states at 130, 136, and 161 GeV, using the OPAL detector at LEP. Cross-sections have been measured for hadronic, $b\overline{b}$, e^+e^-, $\mu^+\mu^-$, and $\tau^+\tau^-$ final states, together with the forward-backward asymmetries for the leptonic final states. We present values both including and excluding the production of radiative $Z\gamma$ events. In general, we define a 'non-radiative' sample as events with $s'/s > 0.8$, whereas 'inclusive' measurements are corrected to $s'/s > 0.01$, where $\sqrt{s'}$ is defined as the centre-of-mass energy of the e^+e^- system after initial-state radiation.

In these analyses, we have introduced a well-defined treatment of the interference between initial- and final-state photon radiation, and an improved method of taking account of the contributions from four-fermion production. While both of these effects are small ($\mathcal{O}(1\%)$) compared with the statistical precision of the current data, they will become significant with the increased luminosity expected at LEP in the future, especially when combining results with other experiments [3]. We have reanalysed our data at 130–136 GeV [1] and 161 GeV [2] using the same treatment of interference and four-fermion effects, in order to provide a uniform sample of measurements for comparison with Standard Model predictions.

The revised results at 130–136 GeV also benefit from several improvements to the analysis. In particular, we benefit from an improved understanding of the background in the inclusive hadronic samples arising from two-photon events. The separation of 'non-radiative' hadronic events has been improved. The main changes to the lepton analyses include increased efficiency for the selection of tau pair events, and the use of a Monte Carlo generator with multiple photon emission for simulating the $e^+e^- \to e^+e^-(n\gamma)$ process instead of one containing only single photon production. There have also been improvements to the detector calibration, which particularly benefit the measurement of R_b, the ratio of the cross-section for $b\overline{b}$ production to the hadronic cross-section. Most of these improvements are already included in the published results at 161 GeV [2].

As has been shown previously [1, 2], the comparable size of the photon exchange and Z exchange amplitudes at these centre-of-mass energies allows constraints to be placed on the size of the interference terms between them. In this paper we improve our previous constraints by including the data at 172 GeV. In an alternative treatment, we assume the Standard Model form of the amplitudes and use the data to investigate the energy dependence of the electromagnetic coupling constant, $\alpha_{\rm em}$. We have also used the data to search for evidence for physics beyond the Standard Model. Firstly we do this within a general framework in which possible contributions from extensions of the Standard Model are described by an effective four-fermion contact interaction. This analysis is essentially the same as those performed in references [2, 4], but the inclusion of data at 172 GeV centre-of-mass energy gives significant improvements to the limits presented there. In the previous analysis of the hadronic cross-section we assumed the contact interaction was flavour-blind; here we extend the study to include the case where the new physics couples exclusively to one up-type quark or one down-type quark. In a second, more specific analysis, we set limits on the coupling strength of a new heavy particle which

might be exchanged in t-channel production of hadronic final states. Such a particle could be a squark, the supersymmetric partner of a quark, in theories where R-parity is violated, or a leptoquark, which is predicted in many theories which connect the quark and lepton sector of the Standard Model. In this analysis we assume that the new physics involves only one isomultiplet of heavy particles coupling with defined helicity. These studies are of topical interest in view of the indication of an anomaly at large momentum transfers in e^+p collisions reported by the HERA experiments [5]. Contact interactions or production of a heavy particle have both been suggested as possible explanations [6–8]. Finally, we place limits on gaugino pair production with subsequent decay of the chargino or neutralino into a light gluino and a quark pair in supersymmetric extensions to the Standard Model.

The paper is organized as follows. In section 2 we describe Monte Carlo simulations, the treatment of interference effects between initial- and final-state radiation and of the contributions from four-fermion final states. In section 3 detailed descriptions of the luminosity measurement and the analysis of hadronic events, of each lepton channel and of the measurement of $R_{\rm b}$ are given. In section 4 we compare measured cross-section and asymmetry values with Standard Model predictions, and use them to place constraints γ-Z interference and $\alpha_{\rm em}$. Finally, in section 5 we use our measurements to place limits on extensions of the Standard Model.

2 Theoretical Considerations and Simulation

2.1 Monte Carlo Simulations

The estimation of efficiencies and background processes makes extensive use of Monte Carlo simulations of many different final states. For studies of $e^+e^- \to$ hadrons we used the PYTHIA5.7 [9] program with input parameters that have been optimized by a study of global event shape variables and particle production rates in Z decay data [10]. For $e^+e^- \to e^+e^-$ we used the BHWIDE [11] Monte Carlo program, and for $e^+e^- \to \mu^+\mu^-$ and $e^+e^- \to \tau^+\tau^-$ the KORALZ4.0 program [12]. Four-fermion events were modelled with the grc4f [13], FERMISV [14] and EXCALIBUR [15] generators, with PYTHIA used to check the separate contributions from WW and Weν diagrams. Two-photon background processes with hadronic final states were simulated using PYTHIA and PHOJET [16] at low Q^2. At high Q^2 the TWOGEN [17] program with the 'perimiss' option [18] was found to give the best description of data; PYTHIA and HERWIG [19] were also used for comparison. The Vermaseren generator [20] was used to simulate purely leptonic final states in two-photon processes. The $e^+e^- \to \gamma\gamma$ background in the e^+e^- final state was modelled with the RADCOR [21] program, while the contribution from $e^+e^-\gamma$ where the photon and one of the charged particles are inside the detector acceptance was modelled with TEEGG [22]. All samples were processed through the OPAL detector simulation program [23] and reconstructed as for real data. For the measurement of the luminosity, the cross-section for small-angle Bhabha scattering was calculated using the Monte Carlo program BHLUMI [24], using generated events processed through a simulation program for the forward calorimetry.

2.2 Initial-final State Photon Interference

A feature of e^+e^- collision data at energies well above the Z mass is a tendency for radiative return to the Z. If one or more initial-state radiation photons are emitted which reduce the effective centre-of-mass energy of the subsequent e^+e^- collision $\sqrt{s'}$ to the region of the Z resonance, the cross-section is greatly enhanced. In order to test the Standard Model at the highest possible energies, we separate clearly radiative events from those with $\sqrt{s'} \sim \sqrt{s}$ using methods similar to those in previous analyses [2]. In this separation, $\sqrt{s'}$ is defined as the centre-of-mass energy of the e^+e^- system after initial-state radiation. The existence of interference between initial- and final-state radiation means that there is an ambiguity in this definition. The Monte Carlo generators used to determine experimental efficiencies and acceptances do not include interference between initial- and final-state radiation, but these programs are used to correct the data, which do include interference. Therefore further corrections have to be applied to the data before measurements can be compared with theoretical predictions.

For Standard Model predictions (for all channels except e^+e^-, which is described below) we use the ZFITTER [25] program, which has an option either to enable or to disable interference between initial- and final-state radiation. We choose to use the option with interference disabled for our comparisons, and correct our measurements to account for this as explained below. This choice has the advantage of making the definition of s' unambiguous, and is more suitable for interpreting the measurements in terms of theoretical parameters. For example, the S-matrix ansatz used to fit the data, described in section 4.1, is unsuitable when the non-resonant part of the interference between initial- and final-state radiation contributes [26].

To determine corrections to the measured cross-sections, we define a differential 'interference cross-section' ($\mathrm{d}^2\sigma_{\mathrm{IFSR}}$ / $\mathrm{d}m_{\mathrm{f\bar{f}}}\,\mathrm{d}\cos\theta$) as the difference between the differential cross-section including initial-final state interference, ($\mathrm{d}^2\sigma_{\mathrm{int}}$ / $\mathrm{d}m_{\mathrm{f\bar{f}}}\,\mathrm{d}\cos\theta$), and that excluding interference, ($\mathrm{d}^2\sigma_{\mathrm{noint}}$ / $\mathrm{d}m_{\mathrm{f\bar{f}}}\,\mathrm{d}\cos\theta$), as calculated by ZFITTER using the appropriate flag settings[1]. The differential interference cross-section may be either positive or negative, depending on the values of the cosine of the angle θ between the fermion and the electron beam direction, and the invariant mass of the fermion pair $m_{\mathrm{f\bar{f}}}$. We then estimate the fraction of this cross-section accepted by our selection cuts by assuming that, as a function of $\cos\theta$ and $m_{\mathrm{f\bar{f}}}$, its selection efficiency

$$\epsilon_{\mathrm{IFSR}}(\cos\theta, m_{\mathrm{f\bar{f}}}) = \epsilon_{\mathrm{noint}}(\cos\theta, m_{\mathrm{f\bar{f}}}), \tag{1}$$

where $\epsilon_{\mathrm{noint}}$ has been determined from Monte Carlo events which do not include interference. The corrected cross-section σ_{corr} is obtained from the measured cross-section after background subtraction and efficiency correction σ_{meas} as:

$$\frac{\mathrm{d}\sigma_{\mathrm{corr}}}{\mathrm{d}\cos\theta} = \frac{\mathrm{d}\sigma_{\mathrm{meas}}}{\mathrm{d}\cos\theta} - \frac{\mathrm{d}\sigma_{\mathrm{noint}}}{\mathrm{d}\cos\theta} \frac{\int \epsilon_{\mathrm{IFSR}}(\cos\theta, m_{\mathrm{f\bar{f}}}) \frac{\mathrm{d}^2\sigma_{\mathrm{IFSR}}}{\mathrm{d}m_{\mathrm{f\bar{f}}}\mathrm{d}\cos\theta}\mathrm{d}m_{\mathrm{f\bar{f}}}}{\int \epsilon_{\mathrm{noint}}(\cos\theta, m_{\mathrm{f\bar{f}}}) \frac{\mathrm{d}^2\sigma_{\mathrm{noint}}}{\mathrm{d}m_{\mathrm{f\bar{f}}}\mathrm{d}\cos\theta}\mathrm{d}m_{\mathrm{f\bar{f}}}}. \tag{2}$$

In practice the integrals were evaluated in appropriate bins of $\cos\theta$ and $m_{\mathrm{f\bar{f}}}$. As the accepted cross-section is estimated as a function of $\cos\theta$, the method is easily applied to total cross-sections, angular distributions or asymmetry measurements.

[1] Cross-sections including interference are obained by setting `INTF`=1, those excluding interference by setting `INTF`=0. For hadrons, we also set `INCL`=0 to enable the `INTF` flag.

Interference Corrections ($s'/s > 0.8$)				
	130.25 GeV	136.22 GeV	161.34 GeV	172.12 GeV
$\Delta\sigma_{\rm had}/\sigma_{\rm SM}$ (%)	$+1.0 \pm 0.3 \pm 0.4$	$+1.2 \pm 0.4 \pm 0.5$	$+1.3 \pm 0.4 \pm 0.6$	$+1.2 \pm 0.3 \pm 0.5$
$\Delta\sigma_{\mu\mu}/\sigma_{\rm SM}$ (%)	-1.6 ± 0.5	-1.8 ± 0.6	-1.7 ± 0.5	-1.8 ± 0.5
$\Delta\sigma_{\tau\tau}/\sigma_{\rm SM}$ (%)	-1.3 ± 0.4	-1.4 ± 0.4	-1.4 ± 0.4	-1.4 ± 0.4

Table 1: Corrections $\Delta\sigma$, which have to be applied to the measured non-radiative cross-sections in order to remove the contribution from initial-final state interference. They are expressed as a percentage fraction of the expected Standard Model cross-section. The first error reflects the uncertainty from modelling the selection efficiency for the interference cross-section, the second one our estimate of possible additional QCD corrections for the hadrons.

The systematic error on this procedure was assessed by repeating the estimate modifying the assumption of eq. 1 to

$$\epsilon_{\rm IFSR}(\cos\theta, m_{\rm f\bar{f}}) = \frac{\epsilon_{\rm noint}(\cos\theta, m_{\rm f\bar{f}}) + \epsilon_{\rm noint}(\cos\theta, \sqrt{s})}{2}, \qquad (3)$$

i.e. for each bin of $\cos\theta$ and $m_{\rm f\bar{f}}$ the average of the efficiency in that bin and the efficiency in the bin including $m_{\rm f\bar{f}} = \sqrt{s}$ for the same $\cos\theta$ range was used. This was motivated as follows. The efficiencies $\epsilon_{\rm noint}$ used for the interference correction are an average over events with initial-state radiation and events with final-state radiation, and are a good approximation to the true $\epsilon_{\rm IFSR}$ if these efficiencies are similar. For large $m_{\rm f\bar{f}}$ this is the case, but for small $m_{\rm f\bar{f}}$ the efficiency for the relatively rare events with final-state radiation may be significantly higher than that for events with initial-state radiation. To account for this, the error on $\epsilon_{\rm IFSR}$ is taken as half the difference between the average efficiency $\epsilon_{\rm noint}(\cos\theta, m_{\rm f\bar{f}})$, and the largest possible efficiency, $\epsilon_{\rm noint}(\cos\theta, \sqrt{s})$ at a given value of $\cos\theta$.

For the hadrons there is an additional uncertainty due to QCD effects. We have taken this additional uncertainty to be 100% of the correction without an s' cut. The basic assumption here is that the near-cancellation between virtual (box) and real interference effects without cuts (Kinoshita-Lee-Nauenberg theorem [27]) is not completely destroyed by large QCD corrections to both. This has been proven for pure final-state radiation [28], but not yet for initial-final state interference. In the absence of a theoretical calculation we allow the asymptotic value to change by 100%.

The corrections to inclusive ($s'/s > 0.01$) cross-sections are small, reflecting the Kinoshita-Lee-Nauenberg cancellation. They typically amount to (-0.36 ± 0.04)% for muon pairs, (-0.5 ± 0.1)% for tau pairs and $(+0.1 \pm 0.1)$% for hadrons, where the statistical errors are small compared to the systematic errors, derived as described above. For non-radiative events ($s'/s > 0.8$) the corrections are rather larger, and are given in detail in table 1. The differences between the muon and tau corrections reflect the different acceptance cuts in $\cos\theta$ used in the event selection; the hadron corrections are of opposite sign from those of the leptons because of the quark charges. The corrections change the lepton asymmetry values by typically -0.006 ± 0.001 for $s'/s > 0.01$ and -0.015 ± 0.005 for $s'/s > 0.8$. All corrections depend only very weakly on $\sqrt{s}$.

We have checked the results of the above correction procedure by comparing them to an independent estimate using the KORALZ [12] Monte Carlo generator. We generated two samples of muon pair events at 171 GeV, and subjected them to the full detector simulation,

reconstruction and event selection procedures. Both samples were generated with only single photon emission. In the first sample there was no interference between initial- and final-state radiation, while in the second sample interference was enabled. The differences between the observed cross-sections and asymmetries agreed with the estimates from ZFITTER described above within one standard deviation, for both the inclusive ($s'/s > 0.01$) and non-radiative ($s'/s > 0.8$) cases.

The above correction procedure has been applied to all cross-sections, asymmetry measurements and angular distributions, except for those for the e^+e^- final state. In this case, we do not use a cut on s' so there is no ambiguity in its definition. Both the Standard Model calculations and the Monte Carlo program used to calculate efficiency and acceptance corrections include interference between initial- and final-state radiation. Results for e^+e^- are therefore presented including such effects.

2.3 Four-fermion Effects

Contributions from four-fermion production $f\bar{f}f'\bar{f'}$ to the process $e^+e^- \to f\bar{f}$ pose non-trivial problems both experimentally and theoretically. While four-fermion final states arising from the 'two-photon' (multiperipheral) diagrams, for example, can be considered background to two-fermion production, those arising from the emission of low mass $f'\bar{f'}$ pairs in s-channel diagrams may in some circumstances be considered signal, in the same way as is emission of photons. A clean separation is not possible because of interference between diagrams contributing to the same final state.

The correct experimental treatment of the four-fermion contribution depends on whether or not the theoretical calculation with which the experimental measurement is to be compared includes emission of fermion pairs. For example, ALIBABA [29] does not include such emission. By default ZFITTER includes initial-state pair emission via virtual photons, although this can be disabled. However, pair emission via virtual Z bosons is not included. By comparing the predictions of ZFITTER with and without pair emission[2], we estimate that the effect of including it increases the cross-sections for $s'/s > 0.01$ by about 1% and decreases those for $s'/s > 0.8$ by about 0.1% at the energies considered here. Similar values are obtained for hadrons and lepton pairs. Final-state pair radiation is not explicitly treated in ZFITTER. The dominant part of its (very small) effect on the cross-section is covered in the inclusive treatment of final state radiation[3]. For corrections to the selection efficiency, however, both initial- and final-state pair radiation have to be considered, as described below.

None of the theoretical calculations to which we compare our data has an option to separate real from virtual fermion pair effects[4]. Therefore two- and four-fermion events have to be treated together in the data analysis. Considering all four-fermion events as background, for example, would not account for the virtual vertex corrections, which can be even larger than the effects of real pair emission. Therefore some four-fermion events always have to be excluded from background estimates.

[2] We have modified the ZFITTER code so that the s' cut acts on fermion pairs as well as photons, since by default hard pair emission leading to $s' < 0.5s$ is not included.

[3] Inclusive treatment of final-state radiation is obtained by setting the flag `FINR`=0.

[4] ZFITTER with the flag `FOT2`=2, like ALIBABA, includes neither real pair emission nor vertex corrections involving virtual pairs. The default setting `FOT2`=3 includes both, summing up beforehand the soft part of real pair emission and the vertex corrections.

In general, we compare our measurements with ZFITTER predictions including pair emission. This means that pair emission via virtual photons from both the initial and final state must be included in efficiency calculations, and be excluded from background estimates. In order to perform the separation, we ignore interference between s- and t-channel diagrams contributing to the same four-fermion final state, and generate separate Monte Carlo samples for the different diagrams for each final state. For a two-fermion final state $\mathrm{f\bar{f}}$ we then include as signal those four-fermion events arising from s-channel processes for which $m_{\mathrm{f\bar{f}}} > m_{\mathrm{f'\bar{f}'}}$, $m_{\mathrm{f'\bar{f}'}} <$ 70 GeV and $m^2_{\mathrm{f\bar{f}}}/s > 0.01$ ($m^2_{\mathrm{f\bar{f}}}/s > 0.8$ in the non-radiative case). This kinematic classification closely models the desired classification of $\mathrm{f\bar{f}f'\bar{f}'}$ in terms of intermediate bosons, in that pairs arising from virtual photons are generally included as signal whereas those arising from virtual Z bosons are not. All events arising from s-channel processes failing the above cuts, together with those arising from the t-channel process (Zee) and two-photon processes are regarded as background. Four-fermion processes involving WW or single W production are also background in all cases. The overall efficiency, ϵ, is calculated as

$$\epsilon = (1 - \frac{\sigma_{\mathrm{f\bar{f}f'\bar{f}'}}}{\sigma_{\mathrm{tot}}})\epsilon_{\mathrm{f\bar{f}}} + \frac{\sigma_{\mathrm{f\bar{f}f'\bar{f}'}}}{\sigma_{\mathrm{tot}}}\epsilon_{\mathrm{f\bar{f}f'\bar{f}'}} \qquad (4)$$

where $\epsilon_{\mathrm{f\bar{f}}}$, $\epsilon_{\mathrm{f\bar{f}f'\bar{f}'}}$ are the efficiencies derived from the two-fermion and four-fermion signal Monte Carlo events respectively, $\sigma_{\mathrm{f\bar{f}f'\bar{f}'}}$ is the generated four-fermion cross-section, and σ_{tot} is the total cross-section from ZFITTER including pair emission. Using this definition of efficiency, effects of cuts on soft pair emission in the four-fermion generator are correctly summed with vertex corrections involving virtual pairs. The inclusion of the four-fermion part of the signal produces negligible changes to the efficiencies for hadronic events and for lepton pairs with $s'/s > 0.8$. The efficiencies for lepton pairs with $s'/s > 0.01$ are decreased by about 0.5%.

The discussion in the above paragraph applies to hadronic, muon pair and tau pair final states. In the case of electron pairs, the situation is slightly different. In principle the t-channel process with a second fermion pair arising from the conversion of a virtual photon emitted from an initial- or final-state electron should be included as signal. As this process is not included in any program we use for comparison we simply ignore such events: they are not included as background as this would underestimate the cross-section.

3 Data Analysis

The OPAL detector[5], trigger and data acquisition system are fully described elsewhere [30–34]. Data from three separate data-taking periods are used in this analysis:

- Integrated luminosities of 2.7 pb^{-1} and 2.6 pb^{-1} recorded at $\mathrm{e^+e^-}$ centre-of-mass energies of 130.25 and 136.22 GeV, respectively, in 1995 (LEP1.5). The energy measurements have a common systematic uncertainty of 0.05 GeV [35].

- An integrated luminosity of 10.1 pb^{-1} recorded at an $\mathrm{e^+e^-}$ centre-of-mass energy of 161.34±0.05 GeV [35] during 1996.

[5]OPAL uses a right-handed coordinate system in which the z axis is along the electron beam direction and the x axis is horizontal. The polar angle, θ, is measured with respect to the z axis and the azimuthal angle, ϕ, with respect to the x axis.

- An integrated luminosity of approximately 9.3 pb^{-1} at an e^+e^- centre-of-mass energy of 172.3 GeV and 1.0 pb^{-1} at an energy of 170.3 GeV, recorded during 1996. The data from these two energies have been analysed together; the luminosity-weighted mean centre-of-mass energy has been determined to be 172.12$\pm$0.06 GeV [35].

3.1 Measurement of the Luminosity

The integrated luminosity was measured using small-angle Bhabha scattering events, $e^+e^- \to e^+e^-$, recorded in the forward calorimetry. The primary detector is a silicon-tungsten luminometer [32] which consists of two finely segmented silicon-tungsten calorimeters placed around the beam pipe, symmetrically on the left and right sides on the OPAL detector, 2.4 m from the interaction point. Each calorimeter covers angles from the beam between 25 and 59 mrad. Bhabha scattering events were selected by requiring a high energy cluster in each end of the detector, using asymmetric acceptance cuts. The energy in each calorimeter had to be at least half the beam energy, and the average energy had to be at least three quarters of the beam energy. The two highest energy clusters were required to be back-to-back in ϕ, $||\phi_R - \phi_L| - \pi| <$ 200 mrad, where ϕ_R and ϕ_L are the azimuthal angles of the cluster in the right- and left-hand calorimeter respectively. They were also required to be collinear, by placing a cut on the difference between the radial positions, $\Delta R \equiv |R_R - R_L| < 25$ mm, where R_R and R_L are the radial coordinates of the clusters on a plane approximately 7 radiation lengths into the calorimeter. This cut, corresponding to an acollinearity angle of about 10.4 mrad, effectively defines the acceptance for single-photon radiative events, thus reducing the sensitivity of the measurement to the detailed energy response of the calorimeter. The distribution of ΔR for the 172 GeV data is shown in figure 1(a).

For the 130–136 GeV data, the inner and outer radial acceptance cuts delimited a region between 31 and 52 mrad on one side of the calorimeter, while for the opposite calorimeter a wider zone between 27 and 56 mrad was used. Two luminosity measurements were formed with the narrower acceptance on one side or the other side. The final measurement was the average of the two and has no first order dependence on beam offsets or tilts. Before data-taking started at $\sqrt{s}$=161 GeV, tungsten shields designed to protect the tracking detectors from synchrotron radiation were installed around the beam pipe. The shields, 5 mm thick and 334 mm long, present roughly 50 radiation lengths to particles originating from the interaction region, almost completely absorbing electromagnetically showering particles between 26 and 33 mrad from the beam axis. The fiducial regions for accepting Bhabha events for the 161 and 172 GeV data were therefore reduced, to between 38 and 52 mrad on one side and between 34 and 56 mrad on the opposite side. The distributions of the radial coordinates of the clusters for the 172 GeV data are shown in figure 1(b,c).

The error on the luminosity measurement is dominated by data statistics. For the 130 and 136 GeV data, the acceptance of the luminometer was reduced at the trigger level by a prescaling factor of 16 in order to increase the experimental live time as far as possible, giving a statistical error of 0.9% on the combined 130 and 136 GeV data. For the two higher energies this prescaling factor was reduced to 2 or 4, and the statistical error amounts to 0.42% (0.43%) at 161 (172) GeV. The largest systematic uncertainty arises from theoretical knowledge of the cross-section (0.25%), with detector effects amounting to a further 0.20% (0.23%) at 161 (172) GeV.

A second luminosity measurement was provided by the forward detector, a lead-scintillator sampling calorimeter covering angles from the beam between 40 and 150 mrad. The selection of Bhabha events within the calorimeter acceptance is unchanged from reference [36], but the acceptance was reduced to the region between 65 and 105 mrad from the beam because of the addition of the silicon-tungsten luminometer on the inside front edge of the device. The overall acceptance of the calorimeter was measured by normalizing to the precisely known cross-section for hadronic events at the Z peak, and applying small corrections derived from Monte Carlo simulations to reflect changes in acceptance with centre-of-mass energy. To allow for changes in acceptance between years, this normalization was performed separately for 1995 and 1996 using data recorded at the Z in each year. Knowledge of the hadronic acceptance for the Z data is the main source of systematic error in the forward detector luminosity measurement, which amounts to 0.8% (1.0%) for the data taken in 1995 (1996).

The luminosity measured by the forward detector agreed with that measured by the silicon-tungsten luminometer to within one standard deviation of the combined error for all data samples. For the 130 and 136 GeV data, where the precision of the two measurements was similar, the average luminosity was used; the overall error on this average measurement is 0.7%. At 161 and 172 GeV the silicon-tungsten luminosity was preferred as the more precise; the overall error on this measurement amounts to 0.53% (0.55%) at 161 (172) GeV. The errors on luminosity are included in the systematic errors on all cross-section measurements presented in this paper. Correlations between cross-section measurements arising from errors in the luminosity have been taken into account in the interpretation of the results.

3.2 Hadronic Events

3.2.1 Inclusive Events ($s'/s > 0.01$)

The criteria used to select an inclusive sample of hadronic events with $s'/s > 0.01$ were based on energy clusters in the electromagnetic calorimeter and the charged track multiplicity. Clusters in the barrel region were required to have an energy of at least 100 MeV, and clusters in the endcap detectors were required to contain at least two adjacent lead glass blocks and have an energy of at least 200 MeV. Tracks were required to have at least 20 measured space points. The point of closest approach to the nominal beam axis was found, and required to lie less than 2 cm in the r–ϕ plane and less than 40 cm along the beam axis from the nominal interaction point. Tracks were also required to have a minimum momentum component transverse to the beam direction of 50 MeV.

The following requirements were used to select hadronic candidates.

- To reject leptonic final states, events were required to have high multiplicity: at least 7 electromagnetic clusters and at least 5 tracks.
- Background from two-photon events was reduced by requiring a total energy deposited in the electromagnetic calorimeter of at least 14% of the centre-of-mass energy: $R_{\rm vis} \equiv \Sigma E_{\rm clus}/\sqrt{s} > 0.14$, where $E_{\rm clus}$ is the energy of each cluster.
- Any remaining background from beam-gas and beam-wall interactions was removed, and two-photon events further reduced, by requiring an energy balance along the beam direction which satisfied $R_{\rm bal} \equiv \mid \Sigma(E_{\rm clus} \cdot \cos\theta) \mid /\Sigma E_{\rm clus} < 0.75$, where θ is the polar angle of the cluster.

These criteria are identical to those used previously at 161 GeV [2], but the cut on $R_{\rm bal}$ is somewhat looser than that used previously at 130–136 GeV, resulting in a slightly higher efficiency for radiative return events. Distributions of $R_{\rm vis}$ and $R_{\rm bal}$ for each centre-of-mass energy are shown in figure 2. The efficiency of the selection cuts was determined from Monte Carlo simulations, and the value for each centre-of-mass energy is given in table 2. From comparisons of the data distributions of $R_{\rm bal}$ and $R_{\rm vis}$ with Monte Carlo, at these energies and at energies around the Z peak (LEP1), we estimate the systematic error on the selection efficiency to be 1%.

Above the W-pair threshold, the largest single contribution to the background arises from WW events. No cuts have been applied to reject W-pair events; the expected contribution from these to the visible cross-section has been subtracted, and amounts to (2.4±0.2)% at 161 GeV and (9.6±0.2)% at 172 GeV, where the error arises mainly from the uncertainty in the W mass [37]. Backgrounds to the inclusive hadron samples at all energies arise from other four-fermion events which are not considered part of the signal, in particular two-photon events and the channels Zee and Weν, and tau pairs. These amount to 1.9% at 130 GeV, rising to 4.1% at 172 GeV. The main uncertainty on this background arises from the two-photon events; we assign a 50% error to this contribution, which covers the predictions from all the generators discussed in section 2.1.

The numbers of selected events and the resulting cross-sections are shown in table 2.

3.2.2 Non-radiative events ($s'/s > 0.8$)

The effective centre-of-mass energy $\sqrt{s'}$ of the e^+e^- collision for hadronic events selected as above was estimated as follows. The method is the same as that used in reference [2]. Isolated photons in the electromagnetic calorimeter were identified, and the remaining tracks, electromagnetic and hadron calorimeter clusters formed into jets using the Durham (k_T) scheme [38] with a jet resolution parameter $y_{\rm cut} = 0.02$. If more than four jets were found the number was forced to be four. The jet energies and angles were corrected for double counting using the algorithm described in reference [39]. The jets and observed photons were then subjected to a series of kinematic fits with the constraints of energy and momentum conservation, in which zero, one, or two additional photons emitted close to the beam direction were allowed. The fit with the lowest number of extra photons which gave an acceptable χ^2 was chosen. The value of $\sqrt{s'}$ was then computed from the fitted four-momenta of the jets, i.e. excluding photons identified in the detector or those close to the beam direction resulting from the fit. If none of the kinematic fits gave an acceptable χ^2, $\sqrt{s'}$ was estimated directly from the angles of the jets as in reference [1]. Figure 3 shows $\sqrt{s'}$ distributions at 172 GeV for events with different numbers of photons. Note that this algorithm results in s' equal to s for events which give a good kinematic fit with no photon either in the detector or along the beam direction.

Non-radiative events were selected by demanding $s'/s > 0.8$. The numbers of events selected at each energy are shown in table 2, together with the corresponding efficiencies and the fractions of the $s'/s > 0.8$ sample arising from feedthrough of events with lower s'/s, determined from Monte Carlo simulations.

The estimation of background in the non-radiative samples is less problematic than in the inclusive case, because the contribution from two-photon events is tiny. The largest contribution arises from W-pair events (above the W-pair threshold), and as in the inclusive case

Hadrons ($s'/s > 0.01$)				
	130.25 GeV	136.22 GeV	161.34 GeV	172.12 GeV
Events	832	673	1472	1368
Efficiency (%)	95.8±1.0	95.2±1.0	92.3±0.9	91.2±0.9
Background (pb)	5.9±2.1	5.9±2.1	8.5±1.7	15.6±1.5
$\sigma_{\rm meas}$ (pb)	317±11±5	264±10±4	150±4±2	127±4±2
$\sigma_{\rm corr}$ (pb)	317±11±5	264±10±4	150±4±2	127±4±2
$\sigma_{\rm SM}$ (pb)	330	273	150	125
Hadrons ($s'/s > 0.8$)				
	130.25 GeV	136.22 GeV	161.34 GeV	172.12 GeV
Events	174	166	370	339
Efficiency (%)	91.0±0.7	91.0±0.7	91.8±0.5	91.8±0.5
Feedthrough (%)	8.9±1.9	7.9±1.9	5.2±1.9	4.8±1.9
Background (pb)	1.3±0.1	1.3±0.1	2.73±0.22	6.82±0.26
$\sigma_{\rm meas}$ (pb)	63.5±4.9±1.5	63.1±5.0±1.5	35.1±2.0±0.8	26.7±1.8±0.6
$\sigma_{\rm corr}$ (pb)	64.3±4.9±1.5	63.8±5.0±1.5	35.5±2.0±0.8	27.0±1.8±0.6
$\sigma_{\rm SM}$ (pb)	77.6	62.9	33.7	27.6

Table 2: Numbers of selected events, efficiencies, backgrounds, feedthrough of events from lower s' to the $s'/s > 0.8$ samples and measured cross-sections for hadronic events. The errors on efficiencies, feedthrough and background include Monte Carlo statistics and systematic effects, with the latter dominant. The cross-sections labelled $\sigma_{\rm meas}$ are the measured values without the correction for interference between initial- and final-state radiation, those labelled $\sigma_{\rm corr}$ are with this correction. For the inclusive measurements, the results are the same to the quoted precision. The first error on each measured cross-section is statistical, the second systematic. The Standard Model predictions, $\sigma_{\rm SM}$, are from the ZFITTER [25] program.

the expected contribution has been subtracted. This amounts to (6.0±0.5)% at 161 GeV and (19.8±0.2)% at 172 GeV, where again the dominant error reflects the uncertainty in the W mass. Additional small backgrounds arise from four-fermion production and tau pair events. The total background at each energy is shown in table 2, together with the final non-radiative hadronic cross-sections.

The main systematic error arises from the modelling of the separation of non-radiative from clearly radiative events, and was estimated by comparing eight different methods of separation. For example, the algorithm was changed to allow for only a single radiated photon, the photon identification algorithm was modified, the hadron calorimeter was removed from the analysis or the jet resolution parameter was altered. In each case, the modified algorithm was applied to data and Monte Carlo, and the corrected cross-section computed. The changes observed were in all cases compatible with statistical fluctuations, but to be conservative the largest change (averaged over all beam energies) was taken to define the systematic error, amounting to 2.0%. This error is expected to decrease in future with improved data statistics. The error arising from the subtraction of W-pair background was investigated by performing an alternative analysis in which events identified as W-pairs according to the criteria in reference [40] were rejected. The resulting cross-sections after correcting to no interference, 35.4±1.9±0.8 (26.5±1.7±0.6) pb at 161 (172) GeV are in excellent agreement with those obtained by subtracting the expected

W-pair contribution.

To measure the angular distribution of the primary quark in the hadronic events, we have used as an estimator the thrust axis for each event determined from the observed tracks and clusters. The angular distribution of the thrust axis was then corrected to the primary quark level using bin-by-bin corrections determined from Monte Carlo events. No attempt was made to identify the charge in these events, and thus we measured the folded angular distribution. The measured values for the $s'/s > 0.8$ sample are given in table 3.

Hadrons ($s'/s > 0.8$)				
$\lvert\cos\theta\rvert$	$\mathrm{d}\sigma/\mathrm{d}\lvert\cos\theta\rvert$ (pb)			
	130.25 GeV	136.22 GeV	161.34 GeV	172.12 GeV
$[0.0, 0.1]$	44 ± 13	35 ± 11	28.0 ± 5.5	22.3 ± 5.2
$[0.1, 0.2]$	47 ± 12	57 ± 14	26.9 ± 5.4	21.7 ± 5.3
$[0.2, 0.3]$	58 ± 15	44 ± 13	36.8 ± 6.3	18.0 ± 4.9
$[0.3, 0.4]$	51 ± 13	58 ± 15	28.4 ± 5.5	27.5 ± 5.9
$[0.4, 0.5]$	52 ± 14	38 ± 12	24.3 ± 5.1	26.5 ± 5.8
$[0.5, 0.6]$	53 ± 14	53 ± 14	29.9 ± 5.6	13.8 ± 4.4
$[0.6, 0.7]$	70 ± 16	114 ± 20	42.5 ± 6.6	36.1 ± 6.4
$[0.7, 0.8]$	66 ± 15	57 ± 14	45.5 ± 6.8	32.5 ± 5.9
$[0.8, 0.9]$	84 ± 17	69 ± 16	38.5 ± 6.2	34.6 ± 6.1
$[0.9, 1.0]$	141 ± 31	122 ± 29	57.7 ± 10.3	35.6 ± 8.2

Table 3: Differential cross-sections for $\mathrm{q\overline{q}}$ production. The values are corrected to no interference between initial- and final-state radiation as described in the text. Errors include statistical and systematic effects combined, with the former dominant.

3.3 Electron Pairs

The production of electron pairs is dominated by t-channel photon exchange, for which a definition of s' as for the other channels is less natural. In addition, the increased probability for final-state radiation relative to initial-state radiation renders the separation between initial- and final-state photons more difficult. Events with little radiation were therefore selected by a cut on θ_{acol}, the acollinearity angle between electron and positron. A cut of $\theta_{\mathrm{acol}} < 10^\circ$ roughly corresponds to a cut on the effective centre-of-mass energy of $s'/s > 0.8$, for the s-channel contribution. We measure cross-sections for three different acceptance regions, defined in terms of the angle of the electron, θ_{e^-}, or positron, θ_{e^+}, with respect to the incoming electron direction, and the acollinearity angle:

- **A:** $\lvert\cos\theta_{\mathrm{e}^-}\rvert < 0.9$, $\lvert\cos\theta_{\mathrm{e}^+}\rvert < 0.9$, $\theta_{\mathrm{acol}} < 170^\circ$; this is a loose 'inclusive' measurement;
- **B:** $\lvert\cos\theta_{\mathrm{e}^-}\rvert < 0.7$, $\theta_{\mathrm{acol}} < 10^\circ$; this acceptance region is expected to be enriched in the s-channel contribution, and is used for asymmetry measurements; in addition, we measure the angular distribution for $\lvert\cos\theta_{\mathrm{e}^-}\rvert < 0.9$ and $\theta_{\mathrm{acol}} < 10^\circ$;

- **C:** $|\cos\theta_{e^-}| < 0.96$, $|\cos\theta_{e^+}| < 0.96$, $\theta_{\rm acol} < 10^\circ$; this 'large acceptance' selection acts as a check on the luminosity measurements.

The selection of electron pair events is identical to previous analyses [2]. Events selected as electron pairs are required to have at least two and not more than eight clusters in the electromagnetic calorimeter, and not more than eight tracks in the central tracking chambers. At least two clusters must have an energy exceeding 20% of the beam energy, and the total energy deposited in the electromagnetic calorimeter must be at least 50% of the centre-of-mass energy. For selections A and B, at least two of the three highest energy clusters must each have an associated central detector track. If a cluster has more than one associated track, the highest momentum one is chosen. If all three clusters have an associated track, the two highest energy clusters are chosen to be the electron and positron. For the large acceptance selection, C, no requirement is placed on the association of tracks to clusters, but the requirement on the total electromagnetic energy is increased to 70% of the centre-of-mass energy.

These cuts have a very high efficiency for e^+e^- events while providing excellent rejection of backgrounds, which either have high multiplicity or lower energy deposited in the electromagnetic calorimeter. The efficiency of the selection cuts, and small acceptance corrections, have been determined using Monte Carlo events generated with the BHWIDE [11] program. These are found to be independent of energy over the range considered here. Remaining backgrounds arise from $\tau^+\tau^-$ events and, in the case of the loose acollinearity cut, also from electron pairs in two-photon events and from radiative Bhabha scattering events in which one electron is outside the detector acceptance but the photon is within the acceptance. In the case of the large acceptance selection, C, which does not require tracks, the main background arises from $\gamma\gamma$ final states. The efficiencies and backgrounds at the three energies are summarized in table 4. In figure 4(a,b) we show distributions of total electromagnetic calorimeter energy, after all other cuts, for acceptance regions B and C at 172 GeV, showing reasonable agreement between data and Monte Carlo. The degraded energy resolution in acceptance region C arises from the increased amount of material in front of the electromagnetic calorimeter at large $|\cos\theta|$, where the events are concentrated. The acollinearity angle distribution for the inclusive selection, A, is shown in figure 4(c), and we see good agreement between data and Monte Carlo expectation, including the peak corresponding to radiative s-channel return to the Z.

The numbers of selected events and resulting cross-sections are shown in table 4. The following sources of systematic error in the cross-section measurements have been considered.

- Deficiencies in the simulation of the selection cuts. As shown in figure 4(b), the total calorimeter energy distribution is slightly broader in data than Monte Carlo for the large acceptance selection, C. The effect of this on the efficiency of this selection has been estimated by varying the cut in the range 40% to 75% of the centre-of-mass energy. In the other two selections, a more important effect is the efficiency for finding two tracks, which has been investigated using events in which only one cluster has an associated track.

- Knowledge of the acceptance correction and how well the edge of the acceptance is modelled. Because of the steeply falling distribution, any bias in the measurement of θ has a significant effect on the cross-sections, particularly for the large acceptance selection. This has been investigated by comparing measurements of θ made using central detector tracks, calorimeter clusters and the outer muon chambers. In addition, in each case the

full size of the acceptance correction derived from Monte Carlo has been included as a systematic error.

- Uncertainties in the background contributions. For selections A and B these have been assessed by considering the numbers of events failing the total energy cut. Data and Monte Carlo are consistent within the statistical precision of 30%. The background in the large acceptance selection is almost all from $\gamma\gamma$ final states, which is much less uncertain.

The total systematic error in selections A and B amounts to 1.4% and 0.8% respectively, of which the largest contribution arises from uncertainty in the track matching efficiency (0.8% and 0.5% respectively). In the large acceptance selection, the largest component in the total systematic error of 1.1% arises from uncertainty in modelling the edge of the acceptance (0.9%).

$\mathbf{e^+e^-}$**(A:** $\mathbf{\lvert\cos\theta\rvert < 0.9}$**,** $\mathbf{\theta_{acol} < 170^\circ}$**)**				
	130.25 GeV	136.22 GeV	161.34 GeV	172.12 GeV
Events	591	514	1587	1397
Efficiency (%)	98.2±1.3			
Background (pb)	3.7±1.1	3.4±1.0	2.3±0.7	1.9±0.6
$\sigma_{\rm meas}$ (pb)	220±9±3	197±9±3	158±4±2	135±4±2
$\sigma_{\rm SM}$ (pb)	237	217	154	135
$\mathbf{e^+e^-}$**(B:** $\mathbf{\lvert\cos\theta_{e^-}\rvert < 0.7}$**,** $\mathbf{\theta_{acol} < 10^\circ}$**)**				
	130.25 GeV	136.22 GeV	161.34 GeV	172.12 GeV
Events	112	98	285	246
Efficiency (%)	99.2±0.7			
Background (pb)	0.6±0.2	0.5±0.2	0.4±0.1	0.3±0.1
$\sigma_{\rm meas}$ (pb)	41.3±4.0±0.5	37.3±3.8±0.4	28.1±1.7±0.3	23.5±1.5±0.2
$\sigma_{\rm SM}$ (pb)	43.1	39.5	28.1	24.7
$\mathbf{e^+e^-}$**(C:** $\mathbf{\lvert\cos\theta\rvert < 0.96}$**,** $\mathbf{\theta_{acol} < 10^\circ}$**)**				
	130.25 GeV	136.22 GeV	161.34 GeV	172.12 GeV
Events	1686	1542	4446	3870
Efficiency (%)	98.5±1.1			
Background (pb)	21.1±2.1	19.3±1.9	13.9±1.4	12.2±1.2
$\sigma_{\rm meas}$ (pb)	615±16±8	580±15±8	434±7±5	365±6±5
$\sigma_{\rm SM}$ (pb)	645	592	425	375

Table 4: Numbers of selected events, efficiencies, backgrounds and measured cross-sections for e^+e^- events. The efficiencies are effective values combining the efficiency of selection cuts for events within the acceptance region and the effect of acceptance corrections. The errors on the efficiencies and backgrounds include Monte Carlo statistics and all systematic effects, the latter being dominant. The first error on each measured cross-section is statistical, the second systematic. The Standard Model predictions, $\sigma_{\rm SM}$, are from the ALIBABA [29] program. Unlike all other channels, values for e^+e^- include the effect of interference between initial- and final-state radiation.

The measurement of the angular distribution and asymmetry uses the same event selection as above, with the further requirement that the two tracks have opposite charge. This extra

requirement reduces the efficiency by about 2.5% in the region $|\cos\theta| < 0.9$. In addition, to reduce the effect of charge misassignment, events with $\cos\theta_{e^-} < -0.8$ must satisfy two extra criteria: both electron and positron tracks must have momenta of at least 25% of the beam momentum, and there must be only one good track associated with each cluster. These extra criteria reduce the overall correction factor to the angular distribution for $\cos\theta_{e^-} < -0.8$ from about 25% to 5%.

The observed angular distribution of the electron, for events with $\theta_{acol} < 10^\circ$, is shown in figure 4(d). As the variation of the angular distribution with energy is small over the range considered here, we have summed data from all energies for this comparison with Monte Carlo expectation. The corrected distributions in $\cos\theta$ at each energy are given in table 5. Systematic errors, arising mainly from uncertainty in the efficiency for finding two tracks with opposite charge, amount to 1.2% and are included in the errors in table 5. The forward-backward asymmetries for the $\theta_{acol} < 10^\circ$ sample at each energy within the angular range $|\cos\theta_{e^-}| < 0.7$ were evaluated by counting the numbers of events in the forward and backward $\cos\theta_{e^-}$ hemispheres. The measured values are shown in table 6. Again, the errors are predominantly statistical, with small systematic effects arising from charge misassignment, acceptance definition and background included in the values given.

In figure 5(b) we show the distribution of $\sqrt{s'}$ for the inclusive electron pair events at 172 GeV. The value of s' for each event was estimated from the polar angles, θ_1 and θ_2, of the two electrons, assuming massless three-body kinematics to calculate the energy of a possible undetected initial-state photon along the beam direction as $\sqrt{s} \cdot |\sin(\theta_1+\theta_2)|/(|\sin(\theta_1+\theta_2)| + \sin\theta_1 + \sin\theta_2)$. A similar technique was used to calculate s' for muon pairs and tau pairs. In contrast to the other final states, the radiative return peak forms only a very small contribution to this channel.

e^+e^-				
$[\cos\theta_{\min}, \cos\theta_{\max}]$	$d\sigma/d\cos\theta$ (pb)			
	130.25 GeV	136.22 GeV	161.34 GeV	172.12 GeV
$[-0.9, -0.7]$	$6\pm^{6}_{3}$	$6\pm^{6}_{3}$	$4.6\pm^{2.2}_{1.6}$	$1.5\pm^{1.5}_{0.8}$
$[-0.7, -0.5]$	$4\pm^{5}_{2}$	$4\pm^{5}_{3}$	$2.4\pm^{1.7}_{1.1}$	$1.4\pm^{1.4}_{0.8}$
$[-0.5, -0.3]$	$7\pm^{6}_{4}$	$10\pm^{7}_{4}$	$1.4\pm^{1.5}_{0.8}$	$0.4\pm^{1.1}_{0.4}$
$[-0.3, -0.1]$	$6\pm^{6}_{3}$	$8\pm^{6}_{4}$	$2.4\pm^{1.7}_{1.1}$	$3.8\pm^{1.9}_{1.4}$
$[-0.1, \ 0.1]$	$11\pm^{7}_{5}$	$8\pm^{6}_{4}$	$6.0\pm^{2.3}_{1.8}$	$5.3\pm^{2.2}_{1.6}$
$[\ 0.1, \ 0.3]$	$19\pm^{8}_{6}$	$15\pm^{8}_{5}$	16 ± 3	18 ± 3
$[\ 0.3, \ 0.5]$	49 ± 10	$23\pm^{9}_{7}$	32 ± 4	23 ± 3
$[\ 0.5, \ 0.7]$	112 ± 15	121 ± 15	79 ± 6	65 ± 6
$[\ 0.7, \ 0.9]$	795 ± 40	701 ± 38	588 ± 19	506 ± 17
$\mu^+\mu^-$				
$[\cos\theta_{\min}, \cos\theta_{\max}]$	$d\sigma/d\cos\theta$ (pb)			
	130.25 GeV	136.22 GeV	161.34 GeV	172.12 GeV
$[-1.0, -0.8]$	$-1\pm^{3}_{0}$	$0\pm^{3}_{0}$	$1.2\pm^{1.8}_{0.9}$	$-0.1\pm^{0.8}_{0.0}$
$[-0.8, -0.6]$	$5\pm^{6}_{3}$	$0\pm^{2}_{0}$	$0.4\pm^{1.2}_{0.5}$	$1.0\pm^{1.4}_{0.7}$
$[-0.6, -0.4]$	$0\pm^{4}_{2}$	$0\pm^{2}_{0}$	$2.5\pm^{1.8}_{1.2}$	$0.4\pm^{1.2}_{0.4}$
$[-0.4, -0.2]$	$7\pm^{6}_{4}$	$6\pm^{6}_{3}$	$0.1\pm^{1.2}_{0.4}$	$0.3\pm^{1.2}_{0.4}$
$[-0.2, \ 0.0]$	$1\pm^{4}_{2}$	$3\pm^{5}_{3}$	$1.9\pm^{1.6}_{1.0}$	$2.4\pm^{1.7}_{1.1}$
$[\ 0.0, \ 0.2]$	$2\pm^{5}_{2}$	$5\pm^{6}_{3}$	$0.8\pm^{1.4}_{0.7}$	$0.3\pm^{1.2}_{0.4}$
$[\ 0.2, \ 0.4]$	$9\pm^{6}_{4}$	$4\pm^{5}_{3}$	$2.8\pm^{1.8}_{1.2}$	$2.8\pm^{1.8}_{1.2}$
$[\ 0.4, \ 0.6]$	$3\pm^{5}_{3}$	$14\pm^{8}_{5}$	$2.1\pm^{1.8}_{1.2}$	$3.6\pm^{2.1}_{1.5}$
$[\ 0.6, \ 0.8]$	$5\pm^{6}_{3}$	$10\pm^{7}_{5}$	$5.5\pm^{2.4}_{1.8}$	$1.9\pm^{1.8}_{1.2}$
$[\ 0.8, \ 1.0]$	$14\pm^{9}_{6}$	$20\pm^{11}_{8}$	$4.9\pm^{2.9}_{2.1}$	$5.1\pm^{2.9}_{2.0}$
$\tau^+\tau^-$				
$[\cos\theta_{\min}, \cos\theta_{\max}]$	$d\sigma/d\cos\theta$ (pb)			
	130.25 GeV	136.22 GeV	161.34 GeV	172.12 GeV
$[-1.0, -0.8]$	$-1\pm^{19}_{0}$	$0\pm^{21}_{0}$	$-0.1\pm^{3.5}_{0.0}$	$-0.4\pm^{3.8}_{0.0}$
$[-0.8, -0.6]$	$0\pm^{3}_{0}$	$0\pm^{3}_{0}$	$1.4\pm^{1.9}_{1.0}$	$0.5\pm^{1.7}_{0.6}$
$[-0.6, -0.4]$	$0\pm^{3}_{0}$	$0\pm^{3}_{0}$	$0.7\pm^{1.6}_{0.6}$	$0.7\pm^{1.6}_{0.6}$
$[-0.4, -0.2]$	$0\pm^{3}_{0}$	$0\pm^{3}_{0}$	$1.6\pm^{2.1}_{1.2}$	$0.3\pm^{1.6}_{0.6}$
$[-0.2, \ 0.0]$	$2\pm^{6}_{2}$	$0\pm^{3}_{0}$	$3.4\pm^{2.3}_{1.5}$	$2.3\pm^{2.1}_{1.3}$
$[\ 0.0, \ 0.2]$	$5\pm^{7}_{3}$	$6\pm^{7}_{4}$	$1.9\pm^{2.0}_{1.2}$	$2.2\pm^{2.1}_{1.3}$
$[\ 0.2, \ 0.4]$	$1\pm^{6}_{2}$	$3\pm^{6}_{2}$	$6.1\pm^{2.9}_{2.1}$	$2.6\pm^{2.2}_{1.3}$
$[\ 0.4, \ 0.6]$	$10\pm^{8}_{5}$	$11\pm^{9}_{5}$	$1.5\pm^{2.0}_{1.2}$	$1.9\pm^{2.0}_{1.1}$
$[\ 0.6, \ 0.8]$	$9\pm^{9}_{5}$	$8\pm^{8}_{5}$	$5.4\pm^{2.9}_{2.1}$	$1.8\pm^{2.3}_{1.4}$
$[\ 0.8, \ 1.0]$	$-2\pm^{14}_{0}$	$5\pm^{31}_{11}$	$5.8\pm^{8.8}_{4.3}$	$2.4\pm^{8.1}_{2.9}$

Table 5: Differential cross-sections for lepton pair production. The values for e^+e^- are for $\theta_{\rm acol} < 10^\circ$; those for $\mu^+\mu^-$ and $\tau^+\tau^-$ are for $s'/s > 0.8$ and are corrected to no interference between initial- and final-state radiation as described in the text. Errors include statistical and systematic effects combined, with the former dominant.

$e^+e^-(|\cos\theta_{e^-}| < 0.7, \theta_{acol} < 10^\circ)$				
	130.25 GeV	136.22 GeV	161.34 GeV	172.12 GeV
N_F	98	84	257	222
N_B	12	13	17	17
A_{FB}^{meas}	0.79±0.06	0.73±0.07	0.88±0.03	0.86±0.04
A_{FB}^{SM}	0.80	0.80	0.81	0.81

Table 6: The numbers of forward (N_F) and backward (N_B) events and measured asymmetry values for electron pairs. The measured asymmetry values include corrections for background and efficiency. The errors shown are the combined statistical and systematic errors; in each case the statistical error is dominant. The Standard Model predictions, A_{FB}^{SM}, are from the ALIBABA [29] program. Unlike all other channels, values for e^+e^- include the effect of interference between initial- and final-state radiation.

3.4 Muon Pairs

The selection of muon pair events is essentially identical to previous analyses [2], except that the cut on visible energy has been made dependent on the centre-of-mass energy, to reduce loss of radiative return events at higher energies. Muon pair events were required to have at least two tracks with momentum greater than 6 GeV and $|\cos\theta| < 0.95$, separated in azimuthal angle by more than 320 mrad, and identified as muons. These tracks must have at least 20 hits in the central tracking chambers and the point of closest approach to the nominal beam axis must lie less than 1 cm in the r–ϕ plane and less than 50 cm along the beam axis from the nominal interaction point. To be identified as a muon, a track had to satisfy any of the following conditions:

- At least 2 muon chamber hits associated with the track within $\Delta\phi = (100 + 100/p)$ mrad, with the momentum p in GeV;
- At least 4 hadron calorimeter strips associated with the track within $\Delta\phi = (20 + 100/p)$ mrad, with p in GeV. The average number of strips in layers containing hits had to be less than 2 to discriminate against hadrons. For $|\cos\theta| < 0.65$, where tracks traverse all 9 layers of strips in the barrel calorimeter, a hit in one of the last 3 layers of strips was required;
- Momentum $p > 15$ GeV and the electromagnetic energy associated to the track within $\Delta\phi < 70$ mrad less than 3 GeV.

If more than one pair of tracks satisfied the above conditions, the pair with the largest total momentum was chosen. Background from high multiplicity events was rejected by requiring that there be no more than one other track in the event with a transverse momentum greater than 0.7 GeV.

Background from cosmic ray events was removed using the time-of-flight (TOF) counters and vertex cuts. In the barrel region, at least one TOF measurement was required within 10 ns of that expected for a particle coming from the interaction point. In addition, back-to-back pairs of TOF counters were used to reject cosmic rays which had traversed the detector. Figure 6(a) shows the distribution of time difference, Δt, between pairs of back-to-back TOF

counters for muon pair events, before applying this cut, clearly showing one peak at the origin from muon pairs and a second peak at about 15 ns from cosmic rays. In the forward region, for which TOF information was not available, the matching of the central detector tracks to the interaction vertex was used in order to remove cosmic ray background. The cosmic ray contamination after all cuts is low. There are no events remaining close to the cosmic ray rejection cut boundaries in the 130 and 136 GeV samples, and one event remaining in each of the 161 and 172 GeV samples.

Background from two-photon events was rejected by placing a cut on the total visible energy, $E_{\rm vis}$, defined as the scalar sum of the momenta of the two muons plus the energy of the highest energy cluster in the electromagnetic calorimeter:

$$R_{\rm vis} \equiv E_{\rm vis}/\sqrt{s} > 0.5(m_{\rm Z}^2/s) + 0.35.$$

The value of this cut is 0.15 below the expected value of $R_{\rm vis}$ for muon pairs in radiative return events where the photon escapes detection, visible as secondary peaks in figure 6(b-d).

The value of s' for each event was estimated from the polar angles of the two muons, as described in section 3.3 for electrons. The observed distribution of $\sqrt{s'}$ at 172 GeV is shown in figure 5(c). A non-radiative sample of events was selected by requiring $s'/s > 0.8$. The selection efficiencies, and feedthrough of events from lower s'/s into the non-radiative sample, were determined from Monte Carlo simulations, and are shown in table 7.

The residual background in the inclusive sample, of around 4% at 130 GeV increasing to 11% at 172 GeV, arises mainly from $\rm e^+e^-\mu^+\mu^-$ final states, while that in the non-radiative sample is predominantly $\tau^+\tau^-$ events and amounts to about 5% in total. Total backgrounds are shown in table 7, together with the numbers of selected events and resulting cross-section measurements.

Systematic errors on the cross-section measurements, which arise from uncertainties in efficiency and backgrounds, are small compared to the statistical errors. In all cases, the dominant systematic error arises from the uncertainty in the background contamination.

The observed angular distribution of the μ^- is shown in figure 7(a) for the $s'/s > 0.01$ sample and figure 7(b) for the $s'/s > 0.8$ sample, for all centre-of-mass energies combined. The angular distributions at each energy were corrected for efficiency and background, including feedthrough of muon pair events from lower s'/s into the non-radiative samples, using Monte Carlo events. The corrected angular distributions are shown in table 5. The final values have been obtained by averaging the distribution measured using the negative muon with that using the positive muon; although this averaging does not reduce the statistical errors on the measurements, it is expected to reduce most systematic effects. The forward-backward asymmetries at each energy were obtained by counting the numbers of events in the forward and backward hemispheres, after correcting for background and efficiency. The data at 130 and 136 GeV have been combined for the asymmetry measurements. Systematic errors were assessed by comparing results obtained using different combinations of tracking and muon chambers to measure the muon angles. The total systematic error, including the contribution from the correction for interference between initial- and final-state radiation, is below 0.01 in all cases, much smaller than the statistical errors. The measured asymmetry values are compared with the Standard Model predictions in table 8.

$\mu^+\mu^-$ $(s'/s > 0.01)$				
	130.25 GeV	136.22 GeV	161.34 GeV	172.12 GeV
Events	55	56	110	82
Efficiency (%)	82.6±0.8	82.2±0.8	79.9±0.7	78.8±0.7
Background (pb)	0.8±0.3	0.7±0.3	0.8±0.2	0.9±0.2
$\sigma_{\rm meas}$ (pb)	23.7±3.2±0.5	25.5±3.4±0.5	12.8±1.2±0.3	9.2±1.0±0.3
$\sigma_{\rm corr}$ (pb)	23.6±3.2±0.5	25.5±3.4±0.5	12.8±1.2±0.3	9.2±1.0±0.3
$\sigma_{\rm SM}$ (pb)	22.0	18.8	11.3	9.6
$\mu^+\mu^-$ $(s'/s > 0.8)$				
	130.25 GeV	136.22 GeV	161.34 GeV	172.12 GeV
Events	26	30	45	37
Efficiency (%)	90.1±0.7	89.7±0.7	89.6±0.6	89.8±0.6
Feedthrough (%)	10.7±0.4	8.9±0.3	6.5±0.2	6.1±0.1
Background (pb)	0.3±0.2	0.3±0.2	0.15±0.06	0.20±0.07
$\sigma_{\rm meas}$ (pb)	9.2±1.8±0.2	11.5±2.1±0.2	4.6±0.7±0.1	3.6±0.6±0.1
$\sigma_{\rm corr}$ (pb)	9.0±1.8±0.2	11.4±2.1±0.2	4.5±0.7±0.1	3.6±0.6±0.1
$\sigma_{\rm SM}$ (pb)	8.0	7.0	4.4	3.8

Table 7: Numbers of selected events, efficiencies, backgrounds, feedthrough of events from lower s' to the $s'/s > 0.8$ samples and measured cross-sections for muon pair events. The errors on efficiencies and background include Monte Carlo statistics and systematic effects. The cross-sections labelled $\sigma_{\rm meas}$ are the measured values without the correction for interference between initial- and final-state radiation, those labelled $\sigma_{\rm corr}$ are with this correction. In some cases, the results are the same to the quoted precision. The first error on each measured cross-section is statistical, the second systematic. The Standard Model predictions, $\sigma_{\rm SM}$, are from the ZFITTER [25] program.

3.5 Tau Pairs

The selection of $e^+e^- \to \tau^+\tau^-$ events is based on that used in previous analyses [1,2], using information from the central tracking detectors and electromagnetic calorimetry to identify events with two collimated, low multiplicity jets. However, the cuts have been optimized and unified for the different energies, giving an improved efficiency at 130–136 GeV. An inclusive sample of events was selected with the following cuts.

- Hadronic events were rejected by demanding low multiplicity: the number of tracks reconstructed in the central tracking detectors had to be at least two and at most six, and the sum of the number of tracks and the number of electromagnetic clusters not more than 15.

- The total energy of an event was restricted in order to reject events from $e^+e^- \to e^+e^-(\gamma)$ and two-photon processes: the total visible energy in the event, derived from the scalar sum of all track momenta plus electromagnetic calorimeter energy, was required to be between $0.3\sqrt{s}$ and $1.1\sqrt{s}$. In addition, the total electromagnetic calorimeter energy was required to be less than $0.7\sqrt{s}$ and the scalar sum of track momenta less than $0.8\sqrt{s}$. In the endcap region, $|\cos\theta| > 0.7$, the upper limit on the visible energy was reduced

$\mu^+\mu^-$ $(s'/s > 0.01)$			
	133.17 GeV	161.34 GeV	172.12 GeV
$N_{\rm F}$	71	63	47
$N_{\rm B}$	38	43	32.5
$A_{\rm FB}^{\rm meas}$	0.31±0.09	0.16±0.10	0.18±0.11
$A_{\rm FB}^{\rm corr}$	0.31±0.09	0.16±0.10	0.17±0.11
$A_{\rm FB}^{\rm SM}$	0.29	0.28	0.28
$\mu^+\mu^-$ $(s'/s > 0.8)$			
	133.17 GeV	161.34 GeV	172.12 GeV
$N_{\rm F}$	42	31	27
$N_{\rm B}$	12	12.5	9
$A_{\rm FB}^{\rm meas}$	0.64±0.11	0.47±0.14	0.57±0.15
$A_{\rm FB}^{\rm corr}$	0.63±0.11	0.45±0.14	0.55±0.15
$A_{\rm FB}^{\rm SM}$	0.69	0.60	0.59
$\tau^+\tau^-$ $(s'/s > 0.01)$			
	133.17 GeV	161.34 GeV	172.12 GeV
$N_{\rm F}$	37	35.5	17
$N_{\rm B}$	12	17.5	9
$A_{\rm FB}^{\rm meas}$	0.43±0.13	0.31±0.13	0.21±0.19
$A_{\rm FB}^{\rm corr}$	0.43±0.13	0.30±0.13	0.21±0.19
$A_{\rm FB}^{\rm SM}$	0.29	0.28	0.28
$\tau^+\tau^-$ $(s'/s > 0.8)$			
	133.17 GeV	161.34 GeV	172.12 GeV
$N_{\rm F}$	21	24.5	15
$N_{\rm B}$	1	10.5	6
$A_{\rm FB}^{\rm meas}$	–	0.51±0.15	0.55±0.20
$A_{\rm FB}^{\rm corr}$	–	0.51±0.15	0.55±0.20
$A_{\rm FB}^{\rm SM}$	0.69	0.60	0.59
Combined $\mu^+\mu^-$ and $\tau^+\tau^-$ $(s'/s > 0.01)$			
	133.17 GeV	161.34 GeV	172.12 GeV
$A_{\rm FB}^{\rm meas}$	0.35±0.08	0.21±0.08	0.18±0.10
$A_{\rm FB}^{\rm corr}$	0.35±0.08	0.21±0.08	0.18±0.10
$A_{\rm FB}^{\rm SM}$	0.29	0.28	0.28
Combined $\mu^+\mu^-$ and $\tau^+\tau^-$ $(s'/s > 0.8)$			
	133.17 GeV	161.34 GeV	172.12 GeV
$A_{\rm FB}^{\rm meas}$	0.71±0.08	0.49±0.10	0.57±0.12
$A_{\rm FB}^{\rm corr}$	0.70±0.08	0.48±0.10	0.55±0.12
$A_{\rm FB}^{\rm SM}$	0.69	0.60	0.59

Table 8: The numbers of forward ($N_{\rm F}$) and backward ($N_{\rm B}$) events and measured asymmetry values for muon and tau pairs. The measured asymmetry values include corrections for background and efficiency and are corrected to the full solid angle. The errors shown are the combined statistical and systematic errors; in each case the systematic error is less than 0.01. The values labelled $A_{\rm FB}^{\rm meas}$ are the measured values without the correction for interference between initial- and final-state radiation, those labelled $A_{\rm FB}^{\rm corr}$ are with this correction. In some cases, the results are the same to the quoted precision. The Standard Model predictions, $A_{\rm FB}^{\rm SM}$, are from the ZFITTER [25] program.

to $1.05\sqrt{s}$ because of the less good electron energy resolution. The distribution of total visible energy, after all other cuts have been applied, is shown in figure 8(a) for all centre-of-mass energies combined.

- Background from two-photon events was further reduced by cuts on the missing momentum and its direction. The missing momentum in the transverse plane to the beam axis, calculated using the electromagnetic calorimeter, was required to exceed 1.5 GeV. The polar angle of the missing momentum calculated using tracks only or electromagnetic clusters only was required to satisfy $|\cos\theta| < 0.95$ and $|\cos\theta| < 0.875$ respectively. Figure 8(b) shows the distribution of $\cos\theta$ of the missing momentum vector calculated using electromagnetic clusters after all other cuts have been applied, for all centre-of-mass energies combined.

- Vertex and TOF cuts were imposed to remove cosmic ray events, as for $\mu^+\mu^-$ events. In addition, $e^+e^- \rightarrow \mu^+\mu^-$ events were removed; these were identified by the criteria described in section 3.4, except that the total visible energy was required to exceed 60% of the centre-of-mass energy.

- Tau pair events are characterized by a pair of narrow 'jets'. Tracks and electromagnetic clusters, each treated as separate particles, were combined in the following way. First the highest energy particle in the event was selected and a cone with a half angle of 35° was defined around it. The particle with the next highest energy inside the cone was combined with the first. The momenta of the combined particles were added and the direction of the sum was used to define a new cone, inside which the next highest energy particle was again looked for. This procedure was repeated until no more particles were found inside the cone. Similarly, starting with the highest energy particle among the remainder, a new cone was initiated and treated in the same way. This process continued until finally all the particles in the event had been assigned to a cone.

- At least one charged particle was required for each cone, and the sum of the energy in the electromagnetic calorimeter and the track momenta in a cone had to be more than 1% of the beam energy. Events which had exactly two such cones were selected as $e^+e^- \rightarrow \tau^+\tau^-$ candidates. The direction of each τ was approximated by that of the total momentum vector of its cone of particles. Events were accepted if the average value of $|\cos\theta|$ for the two τ jets, $|\cos\theta_{\rm av}|$, satisfied $|\cos\theta_{\rm av}| < 0.85$.

- Most of the remaining background from two-photon processes was rejected by a cut on the acollinearity and acoplanarity angles of the two τ cones: the acollinearity angle, in degrees, was required to satisfy

$$\theta_{\rm acol} < (180^\circ - 2\tan^{-1}(2m_{\rm Z}\sqrt{s}/(s - m_{\rm Z}^2))) + 10^\circ$$

  and the acoplanarity angle was required to be less than 30°. The value of the cut on acollinearity was chosen such as to include the peak from radiative return events at each energy; it is 50° at 130 GeV rising to 78° at 172 GeV.

- Remaining background from $e^+e^- \rightarrow e^+e^-(\gamma)$ events was removed by rejecting events if the ratio of the electromagnetic energy to the track momentum in both of the τ cones was between 0.9 and 1.1, as expected for an electron.

- Finally, at 161 and 172 GeV, events classified as W-pair candidates according to the criteria in reference [40] were rejected.

The effective centre-of-mass energy of the e^+e^- collision was estimated from the directions of the two τ jets, as described for e^+e^- events in section 3.3. The distribution for the 172 GeV events is shown in figure 5(d). A non-radiative sample of $\tau^+\tau^-$ events was selected from the inclusive sample by requiring $s'/s > 0.8$.

The numbers of events selected at each energy, together with the efficiencies and feedthrough of events from lower s' into the $s'/s > 0.8$ samples, all determined from Monte Carlo simulations, are shown in table 9.

The remaining background, which amounts to 5–13% in the inclusive samples and 2–7% in the non-radiative samples, is mainly from two-photon interactions; there are also contributions from electron and muon pairs. The total background contributions are shown in table 9, together with numbers of selected events and resulting cross-sections.

The main sources of systematic uncertainty in the cross-section measurements arise from the efficiency and background estimation. The error in the efficiency has been estimated using high statistics samples of LEP1 data, that in the background by comparing data and Monte Carlo distributions of the selection variables after loosening some of the cuts.

The observed angular distribution of the τ^- is shown in figure 7(c) for the $s'/s > 0.01$ sample and figure 7(d) for the $s'/s > 0.8$ sample, for all centre-of-mass energies combined. Monte Carlo events were used to correct for efficiency and background, including feedthrough of events from lower s'/s into the non-radiative samples. The corrected angular distributions at each energy are given in table 5. The forward-backward asymmetries were evaluated by counting the corrected numbers of events, as for the muons. Systematic errors were assessed by comparing different methods of determining the asymmetry: using tracks, electromagnetic clusters or both to determine the τ angles. The total systematic error, including the contribution from the correction for interference between initial- and final-state radiation, is below 0.01 in all cases, much smaller than the statistical errors. The measured values are shown in table 8. In the same way as for the muons, we combine the 130 and 136 GeV data for the asymmetry measurements. From table 8 it can be seen that for the non-radiative sample at 133 GeV there is only one event in the backward hemisphere which after correction for efficiency, background and acceptance would yield an unphysical value of the asymmetry.

Combined asymmetries from the $\mu^+\mu^-$ and $\tau^+\tau^-$ channels were obtained, assuming μ–τ universality, by forming a weighted average of the corrected numbers of forward and backward events observed in the two channels at each energy. The combined values are shown in table 8.

3.6 The Fraction R_b of $b\bar{b}$ Events

To measure R_b, the ratio of the cross-section for $b\bar{b}$ production to the hadronic cross-section, we have performed b-flavour tagging for the hadronic events with $s'/s > 0.8$, selected as described in section 3.2. In addition we rquire at least seven tracks that pass standard track quality requirements, and the polar angle of the thrust direction to fulfil $|\cos\theta| < 0.9$ for the 161 and 172 GeV data, $|\cos\theta| < 0.8$ for the 130–136 GeV data. This acceptance cut ensures that a large proportion of tracks are within the acceptance of the silicon microvertex detector, which had a different geometry for the two sets of data.

$\tau^+\tau^-$ $(s'/s > 0.01)$				
	130.25 GeV	136.22 GeV	161.34 GeV	172.12 GeV
Events	31	25	59	32
Efficiency (%)	39.4±1.1	38.4±1.0	33.9±0.9	32.6±0.9
Background (pb)	0.56±0.14	0.51±0.13	0.29±0.08	0.43±0.11
$\sigma_{\rm meas}$ (pb)	27.7±5.0±0.9	23.9±4.8±0.8	16.7±2.2±0.5	8.4±1.5±0.4
$\sigma_{\rm corr}$ (pb)	27.6±5.0±0.9	23.8±4.8±0.8	16.6±2.2±0.5	8.4±1.5±0.4
$\sigma_{\rm SM}$ (pb)	22.0	18.8	11.3	9.6
$\tau^+\tau^-$ $(s'/s > 0.8)$				
	130.25 GeV	136.22 GeV	161.34 GeV	172.12 GeV
Events	12	12	38	25
Efficiency (%)	55.2±1.5	56.1±1.6	56.9±1.5	56.8±1.5
Feedthrough (%)	8.5±0.4	7.2±0.4	4.6±0.1	4.2±0.1
Background (pb)	0.24±0.08	0.22±0.08	0.08±0.03	0.16±0.04
$\sigma_{\rm meas}$ (pb)	6.9±2.0±0.3	7.3±2.1±0.3	6.3±1.0±0.2	3.9±0.8±0.1
$\sigma_{\rm corr}$ (pb)	6.8±2.0±0.3	7.2±2.1±0.3	6.2±1.0±0.2	3.9±0.8±0.1
$\sigma_{\rm SM}$ (pb)	8.0	6.9	4.4	3.8

Table 9: Numbers of selected events, efficiencies, backgrounds, feedthrough of events from lower s' to the $s'/s > 0.8$ samples and measured cross-sections for $\tau^+\tau^-$ events. The errors on efficiencies and background include Monte Carlo statistics and systematic effects. The cross-sections labelled $\sigma_{\rm meas}$ are the measured values without the correction for interference between initial- and final-state radiation, those labelled $\sigma_{\rm corr}$ are with this correction. In some cases, the results are the same to the quoted precision. The first error on each measured cross-section is statistical, the second systematic. The Standard Model predictions, $\sigma_{\rm SM}$, are from the ZFITTER [25] program.

The b-tagging technique is based on the relatively long lifetime (~ 1.5 ps) of bottom hadrons, which allows the detection of secondary vertices significantly separated from the primary vertex. The primary vertex for each event was reconstructed using a χ^2 minimization method incorporating as a constraint the average beam spot position, determined from tracks and the LEP beam orbit measurement system. Although the beam spot is less precisely determined than at LEP 1, the resulting error on the primary vertex position is still small compared to the errors on the reconstructed secondary vertex positions. The secondary vertex reconstruction was the same as adopted in [41], but the minimum number of tracks forming a vertex was reduced from four to three. Vertices were reconstructed in the x–y plane. Tracks used for secondary vertex reconstruction were required to have a momentum greater than 500 MeV. In addition, the impact parameter in the x–y plane relative to the reconstructed primary vertex was required to satisfy $|d_0| < 0.3\,$cm, and its error $\sigma_{d_0} < 0.1\,$cm. This mainly removes badly measured tracks and, for example, tracks from $\rm K^0$ or Λ decays.

For each reconstructed secondary vertex, the decay length L was defined as the distance of the secondary vertex from the primary vertex in the plane transverse to the beam direction, constrained by the direction of the total momentum vector of the tracks assigned to the secondary vertex. The decay length was taken to be positive if the secondary vertex was displaced from the primary vertex in the same hemisphere as the momentum sum of the charged

particles at the vertex, and negative otherwise. The distribution of decay length significance, defined as L divided by its error σ_L, combining data from all centre-of-mass energies, is shown in figure 9(a), superimposed on the Monte Carlo simulation.

A 'folded tag' [41] was used in this analysis in order to reduce the light flavour component and the sensitivity to detector resolution uncertainties. Each hadronic event is divided into two hemispheres by the plane perpendicular to the thrust axis, and the hemispheres are examined separately. Each hemisphere is assigned a 'forward tag' if it contains a secondary vertex with a decay length significance $L/\sigma_L > 3$, or a 'backward tag' if it contains a vertex with a decay length significance $L/\sigma_L < -3$. Neglecting background in the hadronic sample, the difference between the number of forward and backward tagged hemispheres $N_t - \overline{N}_t$ in a sample of $N_{\rm had}$ hadronic events can be expressed as:

$$N_t - \overline{N}_t = 2N_{\rm had}[(\epsilon_{\rm b} - \overline{\epsilon}_{\rm b})R_{\rm b} + (\epsilon_{\rm c} - \overline{\epsilon}_{\rm c})R_{\rm c} + (\epsilon_{\rm uds} - \overline{\epsilon}_{\rm uds})(1 - R_{\rm b} - R_{\rm c})] \qquad (5)$$

where $(\epsilon_{\rm b} - \overline{\epsilon}_{\rm b})$, $(\epsilon_{\rm c} - \overline{\epsilon}_{\rm c})$ and $(\epsilon_{\rm uds} - \overline{\epsilon}_{\rm uds})$ are the differences between the forward and backward tagging efficiencies. The difference for $\rm b\overline{b}$ events $(\epsilon_{\rm b} - \overline{\epsilon}_{\rm b})$ is about a factor of five bigger than that for $\rm c\overline{c}$ events $(\epsilon_{\rm c} - \overline{\epsilon}_{\rm c})$, and a factor of fifty bigger than that for light quark events $(\epsilon_{\rm uds} - \overline{\epsilon}_{\rm uds})$. $R_{\rm c}$ is the ratio of the cross-section for $\rm c\overline{c}$ production to the hadronic cross-section and was computed using ZFITTER. Due to the limited statistics compared with the LEP1 data, a double tag technique cannot be applied in this analysis and one has to rely on a single tag method. Therefore the hemisphere tagging efficiency differences were determined from Monte Carlo, and are shown in table 10; the efficiencies vary only slightly with energy. The errors on these are predominantly systematic. The largest contributions to the systematic errors come from the uncertainties in Monte Carlo modelling of b and c fragmentation and decay, and from track parameter resolution. The b and c fragmentation and decay parameters were estimated by following the prescriptions of reference [42]. The effect of track parameter resolution was evaluated by varying the resolution in the transverse plane by 20%, in analogy to the procedure described in reference [41]. At the three centre-of-mass energy points the expected contribution from four-fermion background was subtracted, as described above for hadronic events. Within this background, only W-pair events are expected to contribute to the tagged sample. The probability for a W-pair event to be tagged was estimated from Monte Carlo to be (7.8±0.4)% at 161 GeV and (8.3±0.4)% at 172 GeV. The errors reflect the uncertainty of charm fragmentation in the W hadronic decay. After four-fermion background subtraction, b purities of the tagged sample of the order of 70% are obtained.

The numbers of selected events, tagged hemispheres and resulting values of $R_{\rm b}$ are shown[6] in table 10. The systematic error on $R_{\rm b}$ is dominated by the uncertainty on the tagging efficiencies. The other important systematic contributions result from Monte Carlo statistics and detector resolution. To check the understanding of the systematic errors, the analysis was repeated on data collected at the Z peak during 1996. The resulting measurement of $R_{\rm b}$ is in excellent agreement with the OPAL published value [41], differing by (0.7±1.7)%, where the error is purely statistical.

The measured values of $R_{\rm b}$ at each energy are compared to the Standard Model prediction in figure 9(b). Values for the $\rm b\overline{b}$ cross-section, derived from the measurements of the hadronic cross-section and $R_{\rm b}$, are given in table 10.

[6]The results presented here supersede those in reference [2]. In particular the statistical errors on $R_{\rm b}$ in reference [2] were calculated incorrectly.

$\mathrm{b\overline{b}}$			
	133.17 GeV	161.34 GeV	172.12 GeV
Events	255	328	296
Forward tags	61	76	66
Backward tags	10	20	25
$(\epsilon_\mathrm{b} - \overline{\epsilon}_\mathrm{b})$	0.414±0.023	0.402±0.021	0.395±0.022
$(\epsilon_\mathrm{c} - \overline{\epsilon}_\mathrm{c})$	0.075±0.006	0.079±0.006	0.080±0.006
$(\epsilon_\mathrm{uds} - \overline{\epsilon}_\mathrm{uds})$	0.0059±0.0015	0.0074±0.0019	0.0085±0.0021
$R_\mathrm{b}^\mathrm{meas}$	0.199±0.040±0.013	0.168±0.040±0.011	0.136±0.048±0.010
$R_\mathrm{b}^\mathrm{corr}$	0.195±0.039±0.013	0.162±0.039±0.011	0.131±0.046±0.010
R_b^SM	0.182	0.169	0.165
$\sigma_{\mathrm{b\overline{b}}}$ (pb)	12.5±2.6±0.9	5.8±1.4±0.4	3.5±1.4±0.3
$\sigma_{\mathrm{b\overline{b}}}^\mathrm{SM}$ (pb)	12.7	5.7	4.6

Table 10: Numbers of selected events, forward and backward tags, tagging efficiency differences and measured values of R_b. The values labelled $R_\mathrm{b}^\mathrm{meas}$ have not been corrected for interference between initial- and final-state radiation, those labelled $R_\mathrm{b}^\mathrm{corr}$ include this correction. The value of the $\mathrm{b\overline{b}}$ cross-section, after correction for interference, is also given. The errors on the tagging efficiency differences include Monte Carlo statistics and systematic effects, the latter being dominant. The first error on R_b or $\sigma_{\mathrm{b\overline{b}}}$ is statistical, the second systematic. The Standard Model predictions, R_b^SM, $\sigma_{\mathrm{b\overline{b}}}^\mathrm{SM}$, are from the ZFITTER [25] program.

4 Comparison with Standard Model Predictions

We compare our measurements with Standard Model predictions taken from the ALIBABA program for electron pairs, and the ZFITTER program for all other final states, with input parameters m_Z=91.1863 GeV, m_top=175 GeV, m_Higgs=300 GeV, $\alpha_\mathrm{em}(m_\mathrm{Z})$=1/128.896 and $\alpha_\mathrm{s}(m_\mathrm{Z})$=0.118. We use ZFITTER version 5.0, with a small modification to the code to ensure that the s' cut is applied to fermion pair emission in the same way as it is to photon emission[7]. Measured values of cross-sections, presented in tables 2, 4, 7, 9 and 10, are shown in figure 10. The measurements are consistent with the Standard Model expectations. The asymmetry measurements, presented in tables 6 and 8, are shown in figure 11, while the corrected angular distributions for hadrons are shown in figure 12 and for electron pairs in figure 13. We have combined the differential cross-sections for muon and tau pairs, and show the average in figure 14. The measured angular distributions and asymmetry values are in satisfactory agreement with the Standard Model expectations.

In figure 15 we show R_inc, defined as the ratio of measured hadronic cross-section to the theoretical muon pair cross-section, as a function of centre-of-mass energy. The muon pair cross-sections are calculated using ZFITTER, as described above. The hadronic cross-sections used here are somewhat different from the measurements presented in section 3.2. We use an inclusive cross-section, $\sigma(\mathrm{q\overline{q}X})$, which is measured in a similar manner to the inclusive

[7] We use default flag settings, except `BOXD`=1, `CONV`=1, `INTF`=0 and `FINR`=0. The effect of the `BOXD` flag is to include the contribution of box diagrams, which are significant at LEP2 energies; the setting of the other flags was discussed in sections 2.2 and 2.3.

hadronic cross-section described above, but without subtraction of the W-pair contribution. The observed cross-section is corrected using an efficiency which includes the effect of W-pair events to give a total cross-section which is the sum of the two-fermion cross-section plus the cross-section for W-pair production with at least one of the W bosons decaying hadronically. This cross-section is thus an inclusive measurement of hadron production in e^+e^- annihilation, in which production thresholds (e.g. for WW, ZZ or new particles) can be seen. The measured values of this cross-section and the ratio $R_{\rm inc}$ are given in table 11. In figure 15 the measured values of $R_{\rm inc}$ are compared with the prediction of ZFITTER, which does not include W-pair production, and also with a theoretical prediction $R_{\rm inc}^{\rm SM}$ including the expected contributions from WW and ZZ events, calculated using GENTLE [45] and FERMISV [14] respectively. The effect of W-pair production is clear.

In figure 15 and table 11 we also show $R_{\rm Born}$, the ratio of the measured hadronic cross-section for $s'/s > 0.8$, corrected to the Born level, to the theoretical muon pair cross-section at the Born level. The correction of the measured cross-section is performed using ZFITTER, and for both the numerator and denominator 'Born level' means the improved Born approximation of ZFITTER. Far below the Z resonance, this ratio becomes the usual R_γ that has been measured by many experiments at lower energy. Some of these low energy measurements [46] are also shown in figure 15. The measurements close to the Z peak have been corrected to our definition of $R_{\rm Born}$ for this figure.

$\mathbf{q\bar{q}X}$				
	130.25 GeV	136.22 GeV	161.34 GeV	172.12 GeV
$\sigma_{\rm corr}$ (pb)	317±11±5	264±10±4	153±4±2	138±4±2
$R_{\rm inc}$	14.4±0.5	14.0±0.6	13.6±0.4	14.4±0.5
$R_{\rm inc}^{\rm SM}$	15.0	14.5	13.6	14.2
$R_{\rm Born}$	7.9±0.6	9.0±0.7	7.9±0.5	6.9±0.5
$R_{\rm Born}^{\rm SM}$	9.5	8.9	7.5	7.2

Table 11: Measured cross-sections for $q\bar{q}X$, after correcting for interference between initial- and final-state radiation. The first error shown is statistical, the second systematic. Also listed are the ratios $R_{\rm inc}$ and $R_{\rm Born}$, as defined in the text, where statistical and systematic errors have been combined, and their respective Standard Model predictions.

4.1 Influence on Electroweak Precision Measurements

In references [1,2] non-radiative data above the Z resonance were used to constrain the size of the interference terms between photon exchange and Z exchange processes, which have amplitudes of similar magnitude. Using the ZFITTER [25] and SMATASY [47] programs, we have repeated the model-independent fits to OPAL data described in references [1,2], including all the measurements of the non-radiative hadronic cross-section and combined $\mu^+\mu^-$ and $\tau^+\tau^-$ asymmetry presented here. In addition, we have included the measurements of the muon and tau pair non-radiative cross-sections; these were not used in the fits in references [1,2]. In the fit, the parameters $j_{\rm had}^{\rm tot}$ and $j_\ell^{\rm fb}$, determining the sizes of the hadronic and leptonic γZ-interference respectively, have been left free (see reference [1] for more discussion of these parameters and

details of the fit). In the Standard Model, j_{had}^{tot} and j_{ℓ}^{fb} have the values 0.216 ± 0.011 and 0.799 ± 0.001 respectively, for a top quark mass of 175 GeV and Higgs boson mass of 300 GeV, where the uncertainties in this prediction come from varying m_{Higgs} in the range 70–1000 GeV, $\alpha_s(m_Z)$ in the range 0.112–0.124, and m_Z, m_{top}, and $\alpha_{em}(m_Z)$ in ranges taken from reference [48].

The results of the fit, which has a χ^2 of 81.5 for 112 degrees of freedom, are given in table 12. For comparison, the table also shows the results of the fit presented in [1] to OPAL data collected at LEP 1 alone, and the Standard Model predictions for j_{had}^{tot} and j_{ℓ}^{fb}. Since the γZ-interference vanishes on the Z peak, the inclusion of data far away from the Z resonance considerably reduces the uncertainty of j_{had}^{tot} [1]. The inclusion of the 130-161 GeV data reduced the uncertainty on j_{had}^{tot} by 55%; a further improvement of about 16% is observed by including the 172 GeV data presented here. As shown in reference [1], this improvement is much larger than that which would be obtained by the inclusion of the full LEP 1 off-peak data. The high energy data also reduce the correlation between fitted values of j_{had}^{tot} and the Z mass, as can be seen in table 12 and figure 16.

OPAL data sample	j_{had}^{tot}	m_Z (GeV)	j_{had}^{tot}, m_Z correlation	j_{ℓ}^{fb}
LEP 1 (1989-92) [36, 43, 44]	-0.18 ± 0.68	91.187 ± 0.013	-0.70	0.684 ± 0.053
LEP 1 + these data	-0.02 ± 0.26	91.184 ± 0.009	-0.31	0.715 ± 0.043
Standard Model	0.22 ± 0.01	—	—	0.799 ± 0.001

Table 12: Fitted values of the hadronic γZ-interference parameter, j_{had}^{tot}, the Z mass, m_Z, and the leptonic γZ-interference parameter, j_{ℓ}^{fb}, using different OPAL data samples. The m_Z values are quoted for the s-dependent Z-width.

4.2 Energy Dependence of α_{em}

The cross-section and asymmetry measurements for $s'/s > 0.8$ have been used to investigate the energy dependence of the electromagnetic coupling α_{em} within the framework of the Standard Model. Here the main information does not come from the γ-Z interference, studied in the fit described above, but from the pure s-channel photon exchange in the leptonic cross-sections.

For final state muon or tau pairs with $s' \sim s$, the photon exchange process, which is proportional to $\alpha_{em}^2(Q^2)$, dominates the Z exchange by factors of 2–4 at centre-of-mass energies of 130–172 GeV. The leptonic forward-backward asymmetries, reflecting the γ-Z interference, are somewhat less sensitive since they depend only linearly on $\alpha_{em}(Q^2)$. For hadronic final states at $s' \sim s$ the ratio between Z and photon exchange is about a factor of five larger than that for leptons, so that they are dominated by Z exchange, even at the highest energies presented here. In contrast to the charged leptons, quarks have a sizeable vector coupling to the Z, which depends on $\sin^2\theta_W(Q^2)$, which in turn is closely related to $\alpha_{em}(Q^2)$ via the Fermi constant G_F. For hadrons, changes to α_{em} affect the photon amplitude and Z amplitude (via the vector coupling) in opposite directions. At 133 GeV, the hadronic cross-section is still sensitive to α_{em} via the Z amplitude, while at larger centre-of-mass energies its sensitivity is considerably reduced due to the relatively increased photon amplitude.

To fit for $\alpha_{em}(\sqrt{s})$ at each centre-of mass energy, we form the χ^2 between our measurements and the Standard Model predictions calculated as a function of $\alpha_{em}(\sqrt{s})$ using ZFITTER,

keeping all other ZFITTER input parameters fixed to the values given above. The dependence of the vector coupling on $\alpha_{\rm em}$ is then effectively included in ZFITTER. In addition to performing a fit for each centre-of-mass energy we also perform a combined fit to all energies, in which $\alpha_{\rm em}$ runs with energy with a slope which corresponds to its fitted value. In this case, we quote as the result the value of $\alpha_{\rm em}$ at a centre-of-mass energy $\sqrt{s}$= 157.42 GeV, corresponding to the luminosity weighted average of $1/s$.

As inputs to the fits, we use the measured values of hadronic, muon pair and tau pair cross-sections, $R_{\rm b}$, and the combined muon and tau asymmetry values, for $s'/s > 0.8$, giving five measurements at each energy. The measurements at 130 and 136 GeV have been combined for this analysis. The correlation coefficients between all the measurements are given in table 13. The most significant correlations are between measurements of the same quantity at different energies arising from common efficiency and background systematics. The error on luminosity measurements gives rise to correlations between cross-section measurements at the same energy, and also, through the systematic error, to small correlations between cross-sections at different energies. The errors on the correction for interference between initial- and final-state radiation are assumed to be fully correlated.

The results of the fits, for the separate centre-of-mass energies and the combined fit, are shown in table 14, with the resulting values of $\alpha_{\rm em}(\sqrt{s})$ plotted in figure 17. The values are consistent with expectation. The asymmetry in the errors arises because the dependence of the asymmetries on $\alpha_{\rm em}$ is linear whereas the cross-sections and $R_{\rm b}$ have a quadratic dependence. In table 15 we show, for each measurement, the normalized residual before and after the combined fit and an estimate of the sensitivity to the value of $\alpha_{\rm em}$. The normalized residual is the difference between measured and predicted value divided by the measurement error, while the sensitivity estimate used here is the number of experimental standard deviations by which the prediction for the quantity changes if $1/\alpha_{\rm em}(157.42\ {\rm GeV})$ is varied by ± 1.0 from its Standard Model value. We see that the measurements of lepton cross-sections are the most sensitive to the value of $\alpha_{\rm em}$, while the influence of the hadronic variables is considerably smaller, as explained above. From the combined fit, we obtain a value of

$$1/\alpha_{\rm em}(157.42\ {\rm GeV}) = 119.9^{+5.1}_{-4.1},$$

where the error arises from the errors on the measurements. The error due to uncertainties in the input parameters to ZFITTER is negligible in comparison, being at most 0.04 for a variation of $m_{\rm Higgs}$ in the range 70–1000 GeV.

The fit described above uses measurements of cross-sections which depend on the measurement of luminosity, which itself assumes the Standard Model running of $\alpha_{\rm em}$ from ($Q^2 = 0$) to typically $Q^2 = (3.5\ {\rm GeV})^2$, where $1/\alpha_{\rm em} \simeq 134$. Therefore it measures running only from $Q \simeq 3.5$ GeV onwards. To become independent of this assumption, we have repeated the combined fit replacing the cross-sections for hadrons, muon and tau pairs with the ratios $\sigma(\mu\mu)/\sigma(\mathrm{q\overline{q}})$ and $\sigma(\tau\tau)/\sigma(\mathrm{q\overline{q}})$. This is possible since, above the Z peak, leptons and hadrons have a very different sensitivity to $\alpha_{\rm em}$, as explained above. The increased correlations between the input quantities have been taken into account. This fit yields a result of $1/\alpha_{\rm em}(157.42\ {\rm GeV}) = 119.9^{+6.6}_{-5.4} \pm 0.1$, with a χ^2/d.o.f. of 7.5/11, very close to the result obtained above but with somewhat larger errors. The second error comes from varying $\alpha_{\rm s}(m_{\rm Z})$ in the range 0.112 to 0.124. This measured value of $1/\alpha_{\rm em}$ is 2.6 standard deviations below the low energy limit of $137.0359979 \pm 0.0000032$ [50], indicating the running of $\alpha_{\rm em}$ from $Q^2 = 0$ independent of the luminosity measurement. There has been only one previous measurement [49] where the running of $\alpha_{\rm em}$ at large Q^2 has been measured dominantly from the photon propagator and not, as

	133.17 GeV					161.34 GeV					172.12 GeV				
	$\sigma(\mathrm{q\bar{q}})$	R_b	$\sigma(\mu\mu)$	$\sigma(\tau\tau)$	$A_\mathrm{FB}(\ell\ell)$	$\sigma(\mathrm{q\bar{q}})$	R_b	$\sigma(\mu\mu)$	$\sigma(\tau\tau)$	$A_\mathrm{FB}(\ell\ell)$	$\sigma(\mathrm{q\bar{q}})$	R_b	$\sigma(\mu\mu)$	$\sigma(\tau\tau)$	$A_\mathrm{FB}(\ell\ell)$
$\sigma(\mathrm{q\bar{q}})$	1.000	–0.004	0.005	0.003	–0.003	0.135	–0.006	–0.001	0.000	–0.003	0.118	–0.005	–0.001	–0.000	–0.003
R_b		1.000	0.001	0.001	0.001	–0.004	0.085	0.001	0.001	0.001	–0.003	0.067	0.001	0.001	0.002
$\sigma(\mu\mu)$			1.000	0.003	0.001	–0.000	0.001	0.012	0.001	0.001	–0.000	0.001	0.014	0.001	0.002
$\sigma(\tau\tau)$				1.000	0.001	–0.000	0.001	0.001	0.022	0.001	–0.000	0.001	0.001	0.020	0.001
$A_\mathrm{FB}(\ell\ell)$					1.000	–0.002	0.002	0.001	0.001	0.004	–0.002	0.001	0.001	0.001	0.004
$\sigma(\mathrm{q\bar{q}})$						1.000	–0.006	0.002	0.002	–0.003	0.122	–0.005	–0.001	0.000	–0.003
R_b							1.000	0.001	0.001	0.002	–0.005	0.057	0.001	0.001	0.002
$\sigma(\mu\mu)$								1.000	0.003	0.001	–0.000	0.001	0.014	0.001	0.002
$\sigma(\tau\tau)$									1.000	0.001	0.000	0.001	0.001	0.025	0.001
$A_\mathrm{FB}(\ell\ell)$										1.000	–0.002	0.001	0.001	0.001	0.004
$\sigma(\mathrm{q\bar{q}})$											1.000	–0.004	0.001	0.001	–0.003
R_b												1.000	0.001	0.001	0.002
$\sigma(\mu\mu)$													1.000	0.002	0.002
$\sigma(\tau\tau)$														1.000	0.001
$A_\mathrm{FB}(\ell\ell)$															1.000

Table 13: Correlation coefficients between the various measured quantities ($s'/s > 0.8$) at each energy.

on the Z peak [51], from the Standard Model relation between the weak and electromagnetic coupling constants. Using a slope corresponding to the fitted value, the combined fit result corresponds to a measurement of $1/\alpha_{\rm em}(m_{\rm Z}) = 121.4^{+6.0}_{-4.9} \pm 0.1$. This measurement is completely statistics limited, essentially independent of $m_{\rm Higgs}$, and does not rely on assumptions about the running of $\alpha_{\rm em}$ at low Q^2, which is the dominant uncertainty in the current value of $1/\alpha_{\rm em}(m_{\rm Z})$ of 128.90±0.09 [52]. If the error can be reduced by more than one order of magnitude with future statistics, a measurement such as this will lead to an improved knowledge of $1/\alpha_{\rm em}(m_{\rm Z})$.

	Fit		Standard Model	
$\sqrt{s}$ (GeV)	$1/\alpha_{\rm em}$	χ^2/d.o.f.	$1/\alpha_{\rm em}$	χ^2/d.o.f.
133.17	$116.9^{+7.6}_{-5.6}$	4.2/4	128.3	6.2/5
161.34	$115.5^{+8.2}_{-5.6}$	3.4/4	128.1	5.3/5
172.12	$128.7^{+13.5}_{-8.9}$	0.9/4	128.0	0.9/5
157.42	$119.9^{+5.1}_{-4.1}$	10.6/14	128.1	12.9/15

Table 14: Results of fits for $\alpha_{\rm em}$. The first three rows show the fits to data at each centre-of-mass energy, the last row the combined fit to all energies. The Standard Model values of $1/\alpha_{\rm em}$, and the χ^2 between the measurements and the Standard Model predictions are also given for comparison.

$\sqrt{s}$ (GeV)	Measurement	χ(SM)	χ(fit)	Sensitivity
133.17	$\sigma(\mathrm{q\overline{q}})$	–1.60	–1.29	0.047
	$R_{\rm b}$	0.31	0.42	0.011
	$\sigma(\mu\mu)$	1.85	1.37	0.045
	$\sigma(\tau\tau)$	–0.35	–0.79	0.042
	$A_{\rm FB}(\ell\ell)$	0.13	0.33	0.021
161.34	$\sigma(\mathrm{q\overline{q}})$	0.84	0.80	0.006
	$R_{\rm b}$	–0.16	–0.02	0.016
	$\sigma(\mu\mu)$	0.09	–0.59	0.068
	$\sigma(\tau\tau)$	1.74	1.29	0.046
	$A_{\rm FB}(\ell\ell)$	–1.24	–1.03	0.023
172.12	$\sigma(\mathrm{q\overline{q}})$	–0.33	–0.44	0.003
	$R_{\rm b}$	–0.73	–0.60	0.014
	$\sigma(\mu\mu)$	–0.39	–1.08	0.070
	$\sigma(\tau\tau)$	0.07	–0.46	0.054
	$A_{\rm FB}(\ell\ell)$	–0.34	–0.14	0.022

Table 15: Normalized residuals χ and sensitivities for the $\alpha_{\rm em}$ fit to the combined data. For each measured quantity we give the residual before and after the fit, and the sensitivity, as defined in the text.

5 Constraints on New Physics

5.1 Limits on Four-fermion Contact Interactions

In this section we use our measurements of non-radiative cross-sections and angular distributions at 130–172 GeV to place limits on possible four-fermion contact interactions. This analysis is similar to those presented previously [2,4]. Because the Standard Model cross-sections decrease as $1/s$, the sensitivity of the measurements to the contact interaction increases with centre-of-mass energy and so the inclusion of data at 172 GeV is expected to give improved limits. In addition, the analysis of the hadronic cross-section in references [2,4] assumed that the contact interaction is flavour blind. Here the study is extended to the case where the new physics couples exclusively to one up-type quark or one down-type quark.

5.1.1 Theoretical Expectation

The Standard Model could be part of a more general theory characterized by an energy scale Λ. The consequences of the theory would be observed at energies well below Λ as a deviation from the Standard Model which could be described by an effective contact interaction, as depicted in figure 18. In the context of composite models of leptons and quarks, the contact interaction is regarded as a remnant of the binding force between the substructure of fermions. If electrons were composite, such an effect would appear in Bhabha scattering ($e^+e^- \to e^+e^-$). If the other leptons and quarks shared the same type of substructure, the contact interaction would exist also in the processes $e^+e^- \to \mu^+\mu^-, e^+e^- \to \tau^+\tau^-$ and $e^+e^- \to q\overline{q}$. Alternatively, a four-fermion contact interaction could be a good description of deviations from the Standard Model due to the exchange of a new very heavy boson of mass m_X if $m_X \gg \sqrt{s}$. More generally, the contact interaction is considered to be a convenient parametrization to describe possible deviations from the Standard Model which may be caused by some new physics. The concept of contact interactions with a universal energy scale Λ is also used in ep and $p\overline{p}$ collisions to search for substructure of quarks or new heavy particles coupling to quarks or gluons.

In the framework of a contact interaction [53] the Standard Model Lagrangian for $e^+e^- \to f\overline{f}$ is extended by a term describing a new effective interaction with an unknown coupling constant g and an energy scale Λ:

$$\mathcal{L}^{\text{contact}} = \frac{g^2}{(1+\delta)\Lambda^2} \sum_{i,j=L,R} \eta_{ij} [\bar{e}_i \gamma^\mu e_i][\bar{f}_j \gamma_\mu f_j] \qquad (6)$$

where $\delta = 1$ for $e^+e^- \to e^+e^-$ and $\delta = 0$ otherwise. Here $e_L(f_L)$ and $e_R(f_R)$ are chirality projections of electron (fermion) spinors, and η_{ij} describes the chiral structure of the interaction. The parameters η_{ij} are free in these models, but typical values are between -1 and $+1$, depending on the type of theory assumed [54]. Here we consider the same set of models as in reference [4]. In addition we consider three other models: LL + RR ($\eta_{LL} = \eta_{RR} = \pm 1$, $\eta_{LR} = \eta_{RL} = 0$) and LR + RL ($\eta_{LL} = \eta_{RR} = 0$, $\eta_{LR} = \eta_{RL} = \pm 1$) [7,55] which are parity-conserving combinations consistent with the limits from atomic parity violation experiments, and $\overline{\mathcal{O}}_{DB}$ ($\eta_{LL} = \pm 1$, $\eta_{RR} = \pm 4$, $\eta_{LR} = \eta_{RL} = \pm 2$) [56].

Equation (6) can be rewritten in terms of the parameter $\varepsilon = (g^2/4\pi)/\Lambda^2$. In this case the

differential cross-section can be expressed as

$$\frac{\mathrm{d}\sigma}{\mathrm{d}\cos\theta} = \sigma_{\mathrm{SM}}(s,t) + C_2^0(s,t)\varepsilon + C_4^0(s,t)\varepsilon^2 \ . \tag{7}$$

Here $t = -s(1-\cos\theta)/2$ and θ is the polar angle of the outgoing fermion with respect to the e^- beam direction. The C_2^0 term describes the interference between the Standard Model and the contact interaction, the C_4^0 term is the pure contact interaction contribution. Their exact form depends on the type of fermion in the final state and the particular model chosen, and is given, for example, in reference [4][8]. If the underlying process is the exchange of a new heavy scalar particle, X, then equation (6) and equation (7) are good approximations of the process so long as $m_{\mathrm{X}} \gg \sqrt{s}$. Limits on the energy scale of the new interaction are extracted assuming $\mathrm{g}^2/4\pi = 1$.

In order to compare the models with the data the lowest order expression given in equation (7) was modified to include electroweak and QCD effects, and experimental cuts and acceptances were taken into account. The Standard Model cross-section σ_{SM} has been calculated using ALIBABA for the $\mathrm{e^+e^-}$ final state and ZFITTER for all other final states. Standard Model parameters were fixed to the values given in section 4. The errors on these quantities are negligible compared to the statistical precision of the data.

The dominant part of the electroweak corrections is due to initial-state radiation, which was taken into account by convolving the theoretical cross-section with the effects of photon radiation according to [57]. Initial-state radiation was calculated up to order α^2 in the leading log approximation with soft photon exponentiation, and the order α leading log final state QED correction was applied. Other electroweak corrections were taken into account by evaluating the cross-sections with the appropriate value of $\sin^2\theta_{\mathrm{W}}^{\mathrm{eff}}$. For the hadronic cross-section, QCD effects were taken into account by multiplying the electroweak-corrected cross-section by $\delta_{\mathrm{QCD}} = 1 + \alpha_{\mathrm{s}}/\pi + 1.409(\alpha_{\mathrm{s}}/\pi)^2$.

5.1.2 Analysis and Results

We have fitted the data presented here on the angular distributions for the non-radiative $\mathrm{e^+e^-} \to \mathrm{e^+e^-}$, $\mathrm{e^+e^-} \to \mu^+\mu^-$, $\mathrm{e^+e^-} \to \tau^+\tau^-$ processes, the non-radiative cross-sections for $\mathrm{e^+e^-} \to \mathrm{q\overline{q}}$, and the measurements of R_{b}. In the case of the leptonic angular distributions, a maximum likelihood fit was used, where the total sample of candidate events was fitted with the theoretical prediction plus the background. The number of events predicted in each bin of $\cos\theta$ is given by

$$N_k^{\mathrm{pred}}(\varepsilon, r, \cos\theta) = (1+r)\left[\sigma_k(\varepsilon)E_k(\cos\theta) + \sigma_{\mathrm{bgd}}^{\mathrm{pred},k}(\cos\theta)\right] L_k \ , \tag{8}$$

where $\sigma_k(\varepsilon)$ is the cross-section at the centre-of-mass energy point k, which is a function of the free parameter ε, $E_k(\cos\theta)$ is the correction factor for experimental efficiency, $\sigma_{\mathrm{bgd}}^{\mathrm{pred},k}(\cos\theta)$ is the predicted background cross-section, and L_k is the integrated luminosity. The background cross-section is evaluated including efficiency and detector acceptances for the different background processes. The factor r is a scaling factor which takes uncertainties from systematic errors into account. It allows the overall normalisation to vary within bounds set by the appropriate

[8] Equation (2) in reference [4] has a typographical error: the factor $4s$ on the left-hand side should be replaced by $2s$.

systematic errors [4]. We derive 95% confidence limits from the values of ε corresponding to a change in the likelihood of 1.92 with respect to the minimum. In the case of the hadronic and $b\overline{b}$ cross-sections, we used a χ^2 fit to the measured values, incorporating the correlations between the measurements as for the $\alpha_{\rm em}$ fit. In this case the 95% confidence limits correspond to a change in χ^2 of 3.84. In the case of the hadronic cross-section, we fit both for the case where the new physics couples equally to all five flavours and under the assumption that the new interaction couples only to one flavour.

The results are shown in table 16 and are illustrated graphically in figure 19; the notation for the different models is identical to reference [4]. The values for $b\overline{b}$ are obtained by fitting the cross-sections for $b\overline{b}$ production, and there is no requirement on whether or not the new interaction couples to other flavours. By contrast, those for up-type quarks and down-type quarks are obtained by fitting the hadronic cross-sections assuming the new interaction couples only to one flavour. Most of the fitted values of ε show no significant deviation from zero, indicating agreement with the Standard Model. However, the quadratic form of the cross-section (equation (7)) can lead to two local minima, and in a few cases the local minimum near zero gives the higher χ^2 or $-\log$(likelihood). As an example, in figure 20 we show the negative log likelihood curve for the fit to the e^+e^- angular distributions, and the χ^2 curve for the fit to the hadronic cross-sections assuming couplings to one up-type quark only, in both cases for the VV model. In the former case the positive interference between the Standard Model and contact interaction amplitudes results in a curve with only a single minimum, whereas in the latter case the negative interference results in two local minima. As can be seen in figure 20(b), one of these is near zero, but the second one gives the lower χ^2. In this case, we quote 0.39 as the central value of ε, while the limits on Λ are derived from the points $\varepsilon = 0.44$ and $\varepsilon = -0.05$ where $\Delta\chi^2$ is 3.84 above the right-hand and left-hand minimum respectively.

The two sets of values Λ_+ and Λ_- shown in table 16 correspond to positive and negative values of ε respectively, reflecting the two possible signs of η_{ij} in equation (6). As before, the data are particularly sensitive to the VV and AA models; the combined data give limits on Λ in the range 4.7–7.7 TeV for these models, roughly 1 TeV higher than those for 130–161 GeV data alone. For the other models the limits generally lie in the range 2–5 TeV, approximately 0.5 TeV above those from previous data. Those for the $\overline{\mathcal{O}}_{\rm DB}$ model are larger (3–12 TeV) because the values of the η parameters are larger for these models. The limits obtained here are complementary to those obtained in $p\overline{p}$ collisions [58]. They are superior to published contact interaction bounds from ep collisions at HERA [59], and severely constrain interpretations of the recently reported excess of events at high momentum transfer at HERA [5].

5.2 Limits on Heavy Particles

The contact interaction analysis is an appropriate framework for searching for effects arising from the exchange of a new particle with mass $m_{\rm X} \gg \sqrt{s}$. For lower mass ranges, $\sqrt{s} \lesssim m_{\rm X} < \Lambda$, we search for signs of new physics not within the framework of the contact interaction, but under the explicit assumption that the new phenomena are due to a heavy particle, which couples to leptons and quarks. Such a particle could be a leptoquark [60] or a squark in supersymmetric theories with R-parity violation [61]. Beyond the kinematic limit for direct production, such a new particle might be seen through a change of the total cross-section in the process $e^+e^- \to q\overline{q}$ via a t-channel exchange diagram as depicted in figure 18. The allowed leptoquark states can be classified according to spin and weak isospin I. We denote scalar particles S_I and vector particles

Channel		LL	RR	LR	RL	VV	AA	LL+RR	LR+RL	$\overline{\mathcal{O}}_{\mathrm{D}}$
		$[\pm1,0,0,0]$	$[0,\pm1,0,0]$	$[0,0,\pm1,0]$	$[0,0,0,\pm1]$	$[\pm1,\pm1,\pm1,\pm1]$	$[\pm1,\pm1,\mp1,\mp1]$	$[\pm1,\pm1,0,0]$	$[0,0,\pm1,\pm1]$	$[\pm1,\pm4,$
e^+e^-	ε_0	$-0.041^{+0.068}_{-0.062}$	$-0.039^{+0.069}_{-0.063}$	$0.017^{+0.048}_{-0.043}$	$0.017^{+0.048}_{-0.043}$	$0.000^{+0.015}_{-0.015}$	$-0.033^{+0.033}_{-0.046}$	$-0.022^{+0.036}_{-0.035}$	$0.009^{+0.023}_{-0.022}$	0.000^{+}
	Λ_+	3.0	3.0	2.9	2.9	5.8	5.6	4.3	4.3	8.6
	Λ_-	2.5	2.5	3.9	3.9	5.8	2.5	3.4	5.4	8.5
$\mu^+\mu^-$	ε_0	$0.013^{+0.051}_{-0.053}$	$0.014^{+0.056}_{-0.059}$	$0.043^{+0.064}_{-0.079}$	$0.043^{+0.064}_{-0.079}$	$0.010^{+0.021}_{-0.021}$	$-0.004^{+0.026}_{-0.026}$	$0.007^{+0.028}_{-0.028}$	$0.023^{+0.038}_{-0.040}$	0.004^{+}
	Λ_+	3.0	2.9	2.5	2.5	4.4	4.6	4.0	3.2	6.7
	Λ_-	3.3	3.0	1.5	1.5	5.6	4.3	4.6	4.0	8.3
$\tau^+\tau^-$	ε_0	$0.027^{+0.063}_{-0.065}$	$0.030^{+0.068}_{-0.073}$	$0.018^{+0.088}_{-0.404}$	$0.018^{+0.088}_{-0.404}$	$0.010^{+0.026}_{-0.025}$	$0.011^{+0.035}_{-0.034}$	$0.014^{+0.035}_{-0.034}$	$0.009^{+0.051}_{-0.057}$	0.005^{+}
	Λ_+	2.6	2.5	2.4	2.4	4.1	3.5	3.5	3.1	6.2
	Λ_-	3.0	2.8	1.5	1.5	4.9	4.2	4.3	1.6	7.4
$\ell^+\ell^-$	ε_0	$0.002^{+0.035}_{-0.035}$	$0.002^{+0.038}_{-0.038}$	$0.023^{+0.036}_{-0.036}$	$0.023^{+0.036}_{-0.036}$	$0.005^{+0.011}_{-0.011}$	$-0.009^{+0.017}_{-0.017}$	$0.001^{+0.019}_{-0.018}$	$0.012^{+0.018}_{-0.018}$	0.002^{+}
	Λ_+	3.7	3.6	3.2	3.2	6.2	6.4	5.2	4.6	9.3
	Λ_-	3.9	3.7	4.4	4.4	7.6	4.8	5.4	6.2	11.
$q\overline{q}$	ε_0	$-0.131^{+0.097}_{-0.045}$	$0.080^{+0.057}_{-0.145}$	$-0.019^{+0.131}_{-0.074}$	$0.176^{+0.041}_{-0.070}$	$0.042^{+0.029}_{-0.075}$	$-0.069^{+0.050}_{-0.022}$	$-0.054^{+0.094}_{-0.038}$	$0.103^{+0.032}_{-0.080}$	0.029^{+}
	Λ_+	3.4	2.4	2.6	2.0	3.3	4.9	3.5	2.5	4.8
	Λ_-	2.2	3.0	2.8	3.7	4.3	3.1	2.9	4.1	7.7
combined	ε_0	$-0.004^{+0.032}_{-0.035}$	$-0.006^{+0.034}_{-0.038}$	$0.023^{+0.036}_{-0.036}$	$0.026^{+0.037}_{-0.033}$	$0.005^{+0.011}_{-0.011}$	$-0.011^{+0.016}_{-0.017}$	$-0.001^{+0.018}_{-0.018}$	$0.013^{+0.018}_{-0.018}$	0.002^{+}
	Λ_+	4.2	4.1	3.3	3.2	6.2	6.9	5.3	4.5	9.2
	Λ_-	3.7	3.5	4.4	5.0	7.7	4.7	5.3	6.5	11.
$b\overline{b}$	ε_0	$-0.021^{+0.043}_{-0.049}$	$-0.065^{+0.116}_{-0.240}$	$-0.045^{+0.143}_{-0.146}$	$0.052^{+0.214}_{-0.105}$	$-0.021^{+0.039}_{-0.176}$	$-0.013^{+0.026}_{-0.032}$	$-0.015^{+0.031}_{-0.036}$	$0.031^{+0.109}_{-0.093}$	-0.018
	Λ_+	4.0	2.8	2.4	1.7	4.6	5.2	4.7	2.2	5.9
	Λ_-	2.8	1.6	1.9	2.8	2.0	3.4	3.3	2.9	3.8
$u\overline{u}$	ε_0	$0.018^{+0.069}_{-0.059}$	$0.555^{+0.075}_{-0.102}$	$-0.022^{+0.356}_{-0.132}$	$-0.132^{+0.266}_{-0.114}$	$0.387^{+0.029}_{-0.035}$	$0.287^{+0.037}_{-0.051}$	$0.010^{+0.039}_{-0.035}$	$-0.051^{+0.215}_{-0.081}$	0.126^{+}
	Λ_+	1.1	1.2	1.5	1.9	1.5	1.7	3.3	2.0	2.6
	Λ_-	3.3	2.8	2.1	1.8	4.5	4.2	4.2	2.3	6.4
$d\overline{d}$	ε_0	$-0.701^{+0.081}_{-0.065}$	$-0.311^{+0.340}_{-0.103}$	$0.033^{+0.154}_{-0.310}$	$0.317^{+0.097}_{-0.178}$	$-0.216^{+0.074}_{-0.044}$	$-0.287^{+0.051}_{-0.037}$	$-0.487^{+0.058}_{-0.046}$	$0.151^{+0.076}_{-0.165}$	-0.045
	Λ_+	3.2	2.3	1.9	1.4	3.6	4.2	3.7	1.9	4.7
	Λ_-	1.1	1.4	1.7	2.4	1.8	1.7	1.3	2.5	3.4

Table 16: Results of the contact interaction fits to the angular distributions for non-radiative $e^+e^- \to e^+e^-$, $e^+e^- \to \mu^+\mu^-$, $e^+e^- \to \tau^+\tau^-$, the cross-sections for $e^+e^- \to q\overline{q}$ and the measurements of R_b presented here. The combined results include all leptonic angular distributions and the hadronic cross-sections. The numbers in square brackets are the values of $[\eta_{LL},\eta_{RR},\eta_{LR},\eta_{RL}]$ which define the models. ε_0 is the fitted value of $\varepsilon = 1/\Lambda^2$, $\Lambda_\pm$ are the 95% confidence level limits. The units of Λ are TeV, those of ε_0 are TeV^{-2}.

V_I. Isomultiplets with different hypercharges are distinguished by a tilde, as in reference [6]. The coupling strength of the leptoquark is given by a coupling constant g_L or g_R, where L and R refer to the chirality of the lepton. The two scalar states S_0 and $S_{1/2}$ and the two vector states V_0 and $V_{1/2}$ can in principle couple to both left and right chiralities. The product $g_L \cdot g_R$ is constrained very strongly by low energy processes [6]. Therefore in this analysis only one coupling at a time is assumed to be non-zero.

In a t-channel reaction the exchange of S_0 and $\tilde{S}_{1/2}$ are equivalent to the exchange of an R-parity violating down-type squark and up-type antisquark respectively. The coupling to electrons is given by the term $\lambda'_{1jk} L_1 Q_j D^c_k$ of the superpotential [62], where the indices denote the family of the particles involved. L_1 and Q_j are the SU(2) doublet lepton and quark superfields and D^c_k denotes a down-type antiquark singlet superfield. The coupling constant λ'_{1jk} is equivalent to g_L in the leptoquark case since the lepton involved is left-handed. In the limit of very large masses, $m_X \gg \sqrt{s}$, the leptoquark coupling constant g_{LQ} is related to the contact interaction coupling constant g_{CI} by $g_{LQ}/m_X = g_{CI}/\Lambda$.

The cross-section for $e^+e^- \rightarrow q\overline{q}$ including t-channel exchange of a leptoquark has been calculated by several authors, for example references [6–8]. It can be written as

$$\frac{d\sigma}{d\cos\theta} = \frac{N_c}{128\pi s} \sum_{i,k=L,R} \rho_{ik} |f_{ik}|^2 \qquad (9)$$

where the colour factor $N_c = 3$, ρ_{ik} are the spin density matrix elements and f_{ik} are the helicity amplitudes for the process $e^-_i e^+ \rightarrow q_k \overline{q}$. The helicity amplitudes used here are taken from reference [6].

In order to compare the model with data the lowest order expression given above was evaluated taking electroweak corrections into account as described in section 5.1 for the contact interaction analysis. No QCD corrections to the heavy particle propagator or vertex corrections were included. Standard Model cross-sections were calculated using ZFITTER.

5.2.1 Analysis and Results

In order to derive a limit on the mass and coupling of a heavy particle which couples to quarks and leptons, we calculate the χ^2 between the measured non-radiative hadronic cross-sections and the model predictions. The predicted cross-section depends on the mass of the heavy particle and its coupling constant. Varying the mass in steps of 25 GeV, for each value we find the coupling constant which minimizes χ^2, and determine the 95% confidence limit on the coupling corresponding to a change in χ^2 of 3.84. We assume the presence of only one leptoquark multiplet at a time. As mentioned above, only one coupling, either g_L or g_R, is assumed to be non-zero. In the case of S_1, V_1 with g_L, and $S_{1/2}$, $V_{1/2}$ with g_R, two states of the isospin multiplet contribute to the hadronic cross-section. Their masses are assumed to be degenerate.

We perform the analysis for two cases. In the first case we consider all non-radiative hadronic events, assuming a non-vanishing coupling to one quark family. In the second case we use the cross-sections for $b\overline{b}$ production as described in section 3.6 considering all possible leptoquark couplings to the b quark.

The results from the analysis of the hadronic cross-sections are presented in figure 21(a) and (b) for the possible scalar leptoquark states. The 95% confidence limits are shown as a

function of the mass m_X and the coupling constant g_L or g_R of the new particle. The limits on g_L for S_0 are equivalent to limits on the Yukawa couplings λ'_{1jk} of supersymmetric models with R-parity violation with $j = 1,2$ and $k = 1,2,3$, where k is the family index of the exchanged squark. The limits on $\tilde{S}_{1/2}$ derived from the hadronic event sample are also limits on λ'_{1jk} with $j = 1,2,3$ and $k = 1,2$, where j is the family index of the exchanged squark. Results from the analysis of the hadronic cross-sections for the vector leptoquark states are shown in figure 22(a) and (b). We do not show limits on the S_0 (V_0) leptoquark with coupling g_R (g_L) because the effect of these particles on the hadronic cross-section at these energies is too small.

Figures 21(c) and 22(c) give the limits on scalar and vector leptoquarks respectively, derived in the analysis of the $b\bar{b}$ cross-sections. Most of these limits are considerably more stringent than those from the total cross-section analysis. The limits are weaker for the $V_{1/2}$ leptoquark with coupling g_R and the V_1 leptoquark with coupling g_L because in these cases two leptoquarks of the isospin multiplet contribute to the hadronic cross-section, but only one of these couples to b quarks. The limit on $\tilde{S}_{1/2}$ is equivalent to a limit on λ'_{1j3} with $j = 1,2,3$.

As can be seen in the figures our analysis is sensitive to leptoquark masses much higher than the beam energy. Direct searches at the Tevatron can exclude scalar and vector leptoquarks with Yukawa couplings down to $\mathcal{O}(10^{-7})$ up to masses of ≈ 225 GeV [63]. Our limits extend this excluded region for large couplings.

As mentioned above, in the limit of very large mass, the leptoquark and contact interaction couplings are related by $g_{LQ}/m_X = g_{CI}/\Lambda$. Where the cross-section formula of a leptoquark exchange corresponds to one of the investigated contact interaction models we have checked the consistency of the two analyses by calculating limits on the leptoquark coupling at masses of several TeV. We found excellent agreement.

5.3 Search for Charginos and Neutralinos Decaying into Light Gluinos

In general, a comparison between the observed number of non-radiative hadronic events and the Standard Model prediction may be used to constrain possible new particle production whose signature is similar to that of the non-radiative hadronic events. The upper limit on the excess in the observed number of events over the Standard Model prediction was determined to be 49.9 events at 95% confidence level, summing over all centre-of-mass energies and taking into account the correlated systematic errors between different centre-of-mass energies. The numbers of observed non-radiative hadronic events are listed in table 2, and the Standard Model prediction was calculated using ZFITTER with input parameters given in section 4. An example with a particular model of new particle production is presented here.

In supersymmetric extensions of the Standard Model, the supersymmetric partners of the gluons are Majorana fermions called gluinos. Experiments at the TEVATRON have excluded a gluino of mass up to about 150 GeV, independent of squark mass [64, 65], if missing energy is a relevant signature. However, a relatively long-lived very light gluino with mass less than 1 GeV might not be completely excluded by any experiment [66].

The supersymmetric partners of the weak gauge and Higgs bosons mix to form charginos and neutralinos. Chargino and neutralino pairs ($\tilde{\chi}_i^+\tilde{\chi}_j^-$, $i,j = 1,2$ and $\tilde{\chi}_i^0\tilde{\chi}_j^0$, $i,j = 1,2,3,4$) can be produced in e^+e^- annihilation via s-channel virtual γ or Z, or in t-channel slepton exchange. The cross-section for chargino pair production is typically a few picobarns at $\sqrt{s} = 172$ GeV, although, if the sneutrino mass is less than 100 GeV, the cross-section can be significantly

reduced by interference between the s-channel and t-channel diagrams. In the usual SUSY scenario, $\tilde{\chi}_i^{\pm}$ decays into a virtual W boson and a neutralino. The cross-section for neutralino pair production is typically a fraction of picobarn at $\sqrt{s} = 172$ GeV for each process. Normally $\tilde{\chi}_i^0$ ($i = 2,3,4$) are assumed to decay into a virtual Z boson and a lighter neutralino. The lightest neutralino is usually expected to be the lightest supersymmetric particle and is stable, however this is unimportant for the present analysis.

Searches for charginos and neutralinos at various experiments have been carried out with an implicit assumption that light gluinos do not exist, so that the decay of charginos or neutralinos leads to signatures of large missing energy [67–70]. If light gluinos exist and squark masses are comparable to the W boson mass, charginos and neutralinos decay dominantly into $\mathrm{q\overline{q}'\tilde{g}}$ (where the q and $\overline{\mathrm{q}}'$ are the same flavour in the neutralino case) through a virtual squark by the strong interaction [66]. For larger squark masses, $m_{\tilde{\mathrm{q}}} \simeq 1.5 m_{\mathrm{W}}$, the squark propagator reduces the decay width into $\mathrm{q\overline{q}'\tilde{g}}$, and this becomes comparable to the $\mathrm{W}^*\tilde{\chi}^0$ or $\mathrm{Z}^*\tilde{\chi}^0$ mode[9]. Since the gluino hadronizes into many hadrons, the signature of such chargino or neutralino events is very similar to ordinary $\mathrm{q\overline{q}}$ events or WW hadronic decay events. Therefore, as proposed in reference [66], we have used the hadronic cross-section measurements for $s'/s > 0.8$ presented in section 3.2 to place limits on any possible contribution from chargino or neutralino pair production in which gauginos decay into $\mathrm{q\overline{q}'\tilde{g}}$. This method has the advantage of being insensitive to details of gluino fragmentation which would cause a significant uncertainty in a search for an excess of multijet events.

The SUSY partners of SU(3), SU(2) and U(1) gauge bosons of the Standard Model (gauginos) are assumed to have the same mass at the Grand Unification mass scale. Masses of these gauginos at the weak scale are determined by the renormalization group equations. As a result, the ratios of the SU(3), SU(2) and U(1) gaugino masses at the weak scale ($M_3 : M_2 : M_1$) are proportional to the strength of the gauge couplings at the weak scale ($\alpha_3 : \alpha_2 : \alpha_1$). Therefore, if the gluino, which is the SU(3) gaugino, is very light (≤ 1 GeV) at the weak scale, all the other gauginos are also very light. We assume $M_3 = M_2 = M_1 = 0$. Then the chargino and neutralino pair cross-sections depend on three SUSY parameters: the Higgsino mixing parameter μ, the ratio of the two vacuum expectation values $\tan\beta$ and the sneutrino mass $m_{\tilde{\nu}}$. We have calculated the cross-sections using the formulae in reference [71]. We assume that the sneutrino mass is larger than the current limit of 43 GeV [72].

To determine the limits, the total number of $\tilde{\chi}_i^+\tilde{\chi}_j^-$ ($i,j = 1,2$) and $\tilde{\chi}_i^0\tilde{\chi}_j^0$ ($i,j = 2,3,4$) events expected at each centre-of-mass energy was calculated from the cross-sections, the integrated luminosity and the detection efficiency. We assume that the branching fractions of $\tilde{\chi}_{1,2}^{\pm} \to \mathrm{q\overline{q}'\tilde{g}}$ and $\tilde{\chi}_{2,3,4}^0 \to \mathrm{q\overline{q}\tilde{g}}$ are 100% and that the detection efficiency for chargino events with $s'/s > 0.8$ is the same as that for $\mathrm{q\overline{q}}$ events at each centre-of-mass energy[10]. We make a similar assumption

[9]The two body decays $\tilde{\chi}_i^{\pm} \to \tilde{\nu}\ell^{\pm}$ or $\tilde{\chi}_i^0 \to \tilde{\nu}\nu$ are in principle possible if $\tilde{\nu}$ is lighter than $\tilde{\chi}_i^{\pm}$ or $\tilde{\chi}_i^0$ respectively. However, assuming $\tilde{\mathrm{q}}$ and $\tilde{\nu}$ masses are almost degenerate in the parameter space considered in this analysis, as is the case in the Minimal Supersymmetric Standard Model, $\tilde{\chi}_i^{\pm} \to \tilde{\mathrm{q}}\overline{\mathrm{q}}'$ or $\tilde{\chi}_i^0 \to \tilde{\mathrm{q}}\overline{\mathrm{q}}$ followed by $\tilde{\mathrm{q}} \to \mathrm{q\tilde{g}}$ will be the dominant decay.

[10]Note that no cuts have been applied to remove hadronic W-pair events. If such cuts had been made, this might have removed chargino pairs. Therefore the assumption that the efficiency is the same is justified. A small decrease of $\mathcal{O}(5-10\%)$ on the s' cut efficiency is e.g. predicted in Monte Carlo simulations of $\mathrm{WW} \to \mathrm{K_L^0 K_L^0 + X}$, for high-mass $\mathrm{K_L^0 K_L^0}$ pairs, when the energy deposits in the hadron calorimeter are ignored. Assuming similar fragmentation behaviour for gluinos and strange quarks [66], the missing energy caused by possible invisible decay products of light gluino bound states is therefore not expected to be large enough to reduce the efficiency of the s' cut significantly.

about the detection efficiency for neutralino pairs, except when $m_{\tilde{\chi}^0_2} < 10$ GeV, where the decay multiplicity could be low. We conservatively assume the efficiency is zero for $\tilde{\chi}^0_2\tilde{\chi}^0_2$ events if $m_{\tilde{\chi}^0_2} < 10$ GeV. If $m_{\tilde{\chi}^0_2} < 3$ GeV, the decay $\tilde{\chi}^0_2 \to \gamma\tilde{\chi}^0_1$ may be significant, which could affect our detection efficiency; therefore we have conservatively assumed the efficiency to be zero for $\tilde{\chi}^0_2\tilde{\chi}^0_j$ events ($j = 3, 4$) if $m_{\tilde{\chi}^0_2} < 3$ GeV.

We first consider the case where the difference between the observed and expected numbers of hadronic events is due to the production of charginos ($\tilde{\chi}^+_i\tilde{\chi}^-_j, i, j = 1, 2$) only. This corresponds to a SUSY model with the looser condition $M_3 = M_2 = 0$ with no restriction on M_1 [66]. The 95% confidence level lower limit obtained on the μ parameter as a function of $\tan\beta$ for this case is shown in figure 23.

We then consider $M_3 = M_2 = M_1 = 0$ [66] and calculate the total number of chargino and neutralino events with the assumptions above. We derive limits on the SUSY parameter μ as a function of $\tan\beta$. The entire μ–$\tan\beta$ region is excluded. Therefore in this particular model these excluded parameter regions imply the exclusion of a light gluino under the assumptions that the branching fractions of $\tilde{\chi}^\pm_{1,2} \to \mathrm{q}\overline{\mathrm{q}}'\tilde{\mathrm{g}}$ and $\tilde{\chi}^0_{2,3,4} \to \mathrm{q}\overline{\mathrm{q}}\tilde{\mathrm{g}}$ are 100% and that the detection efficiency for chargino events and neutralino events (with $m_{\tilde{\chi}^0_2} > 10$ GeV) is the same as that for $\mathrm{q}\overline{\mathrm{q}}$ events with $s'/s > 0.8$ at each centre-of-mass energy. This limit would continue to hold even if smaller branching ratios or a slightly reduced efficiency of the s' cut were to decrease the total number of expected events by 23%.

6 Conclusions

We have presented new measurements of the production of events with two-fermion hadronic and leptonic final states in $\mathrm{e^+e^-}$ collisions at a centre-of-mass energy of 172 GeV, and updated similar measurements at 130–161 GeV. Special attention has been paid to the treatment of the interference between initial- and final-state radiation, and the contribution from four-fermion production. The measured rates and distributions are all consistent with the Standard Model expectations. In a model-independent fit to the Z lineshape, the inclusion of data at 172 GeV provides an improved constraint on the size of the interference between Z and photon amplitudes. Within the framework of the Standard Model, the data have been used to measure the electromagnetic coupling constant, giving $1/\alpha_{\mathrm{em}}(157.42\ \mathrm{GeV}) = 119.9^{+5.1}_{-4.1}$, compatible with expectation.

We have used these data to place limits on possible deviations from the Standard Model represented by effective four-fermion contact interactions. Limits are obtained on the energy scale Λ generally in the range 2–7 TeV, assuming $\mathrm{g}^2/4\pi = 1$. We have searched for the effect of a new heavy particle which might be exchanged in the t-channel. Limits are obtained on the coupling constants $\mathrm{g_L}$, $\mathrm{g_R}$ between typically 0.2 and 0.6 for masses below ~ 200 GeV. These limits can be interpreted both as limits on leptoquarks, or in some cases as limits on squarks in supersymmetric theories with R-parity violation. Compared to previous searches we are able to improve existing limits in particular in the high mass region $m_{\mathrm{X}} > 250\,\mathrm{GeV}$. Limits have also been placed on chargino and neutralino decays to light gluinos in supersymmetric extensions of the Standard Model.

Acknowledgements

We would like to thank F. Caravaglios, H. Dreiner, G.F. Giudice and R. Rückl for helpful discussions concerning the use of these measurements in searching for effects of the t-channel exchange of new particles, and G. Farrar for help in setting limits on light gluino production. We are grateful to G. Altarelli for comments and suggestions on the contact interactions.

We particularly wish to thank the SL Division for the efficient operation of the LEP accelerator at all energies and for their continuing close cooperation with our experimental group. We thank our colleagues from CEA, DAPNIA/SPP, CE-Saclay for their efforts over the years on the time-of-flight and trigger systems which we continue to use. In addition to the support staff at our own institutions we are pleased to acknowledge the
Department of Energy, USA,
National Science Foundation, USA,
Particle Physics and Astronomy Research Council, UK,
Natural Sciences and Engineering Research Council, Canada,
Israel Science Foundation, administered by the Israel Academy of Science and Humanities,
Minerva Gesellschaft,
Benoziyo Center for High Energy Physics,
Japanese Ministry of Education, Science and Culture (the Monbusho) and a grant under the Monbusho International Science Research Program,
German Israeli Bi-national Science Foundation (GIF),
Bundesministerium für Bildung, Wissenschaft, Forschung und Technologie, Germany,
National Research Council of Canada,
Hungarian Foundation for Scientific Research, OTKA T-016660, T023793 and OTKA F-023259.

References

[1] OPAL Collab., G. Alexander et al., Phys. Lett. **B376** (1996) 232.

[2] OPAL Collab., K. Ackerstaff et al., Phys. Lett. **B391** (1997) 291.

[3] ALEPH Collab., D. Buskulic et al., Phys. Lett. **B378** (1996) 373;
L3 Collab., M. Acciarri et al., Phys. Lett. **B370** (1996) 195;
L3 Collab., M. Acciarri et al., CERN-PPE/97-52, May 1997, submitted to Phys. Lett. B.

[4] OPAL Collab., G. Alexander et al., Phys. Lett. **B387** (1996) 432.

[5] H1 Collab., C. Adloff et al., Z. Phys. **C74** (1997) 191;
ZEUS Collab., J. Breitweg et al., Z. Phys. **C74** (1997) 207.

[6] J. Kalinowski, R. Rückl, H. Spiesberger and P.M. Zerwas, Z. Phys. **C74** (1997) 595.

[7] G. Altarelli, J. Ellis, G.F. Giudice, S. Lola and M.L. Mangano, CERN-TH/97-40, `hep-ph/9703276`, March 1997.

[8] H. Dreiner and P. Morawitz, `hep-ph/9703279 v2`, March 1997;
H. Dreiner, private communication.

[9] T. Sjöstrand, Comput. Phys. Commun. **82** (1994) 74.

[10] OPAL Collab., G. Alexander et al., Z. Phys. **C69** (1996) 543.

[11] S. Jadach, W. Placzek, and B.F.L. Ward, Phys. Lett. **B390** (1997) 298.

[12] S. Jadach, B.F.L. Ward and Z. Wąs, Comput. Phys. Commun. **79** (1994) 503.

[13] J. Fujimoto et al., Comput. Phys. Commun. **100** (1997) 128.

[14] J. Hilgart, R. Kleiss, and F. Le Diberder, Comp. Phys. Comm. **75** (1993) 191.

[15] F.A. Berends, R. Pittau and R. Kleiss, Comput. Phys. Commun. **85** (1995) 437.

[16] R. Engel and J. Ranft, Phys. Rev. **D54** (1996) 4244.

[17] A. Buijs et al., Comput. Phys. Commun. **79** (1994) 523.

[18] OPAL Collab. K. Ackerstaff et al., Z. Phys. **C74** (1997) 33.

[19] G. Marchesini et al., Comput. Phys. Commun. **67** (1992) 465.

[20] J.A.M. Vermaseren, Nucl. Phys. **B229** (1983) 347.

[21] F.A. Berends and R. Kleiss, Nucl. Phys. **B186** (1981) 22.

[22] D. Karlen, Nucl. Phys. **B289** (1987) 23.

[23] J. Allison et al., Nucl. Instrum. Methods **A317** (1992) 47.

[24] S. Jadach, E. Richter-Wąs, B.F.L. Ward and Z. Wąs, Comput. Phys. Commun. **70** (1992) 305.

[25] D. Bardin et al., CERN-TH 6443/92 (May 1992); Phys. Lett. **B255** (1991) 290; Nucl. Phys. **B351** (1991) 1; Z. Phys. **C44** (1989) 493;
we use ZFITTER version 5.0 with default parameters, except `BOXD`=1, `CONV`=1, `INTF`=0 and `FINR`=0, and with the following input parameters: $m_{\rm Z}$=91.1863 GeV, $m_{\rm top}$=175 GeV, $m_{\rm Higgs}$=300 GeV, $\alpha_{\rm em}(m_{\rm Z})$=1/128.896, $\alpha_{\rm s}(m_{\rm Z})$=0.118.

[26] R.G. Stuart, Phys. Rev.**D56** (1997) 1515.

[27] T. Kinoshita, J. Math. Phys. **3** (1962) 650;
T.D. Lee and M. Nauenberg, Phys. Rev. **133** (1964) B1549.

[28] A.L. Kataev, Phys. Lett. **B287** (1992) 209.

[29] W. Beenakker et al., Nucl. Phys. **B349** (1991) 323.

[30] OPAL Collab., K. Ahmet et al., Nucl. Instrum. Methods **A305** (1991) 275.

[31] P.P. Allport et al., Nucl. Instrum. Methods **A324** (1993) 34;
P.P. Allport et al., Nucl. Instrum. Methods **A346** (1994) 476.

[32] B.E. Anderson et al., IEEE Trans. Nucl. Sci. **41** (1994) 845.

[33] M. Arignon et al., Nucl. Instrum. Methods **313** (1992) 103;
M. Arignon et al., Nucl. Instrum. Methods **333** (1993) 330.

[34] J.T. Baines et al., Nucl. Instrum. Methods **A325** (1993) 271;
D.G. Charlton, F. Meijers, T.J. Smith and P.S. Wells, Nucl. Instrum. Methods **A325** (1993) 129.

[35] The LEP Energy Working Group, 'LEP Energy Calibration in 1996', LEP Energy Group/97-01, March 1997; 'Energies for LEP1.5 run', LEP Energy Group/97-04, July 1997;
`http://www.cern.ch/LEPECAL/reports/reports.html`.

[36] OPAL Collab., P.D. Acton et al., Z. Phys. **C58** (1993) 219.

[37] Particle Data Group, R.M. Barnett et al., Phys. Rev. **D54** (1996) 1.

[38] N. Brown and W.J. Stirling, Phys. Lett. **B252** (1990) 657;
S. Bethke, Z. Kunszt, D. Soper and W.J. Stirling, Nucl. Phys. **B370** (1992) 310;
S. Catani et al., Phys. Lett. **B269** (1991) 432;
N. Brown and W.J. Stirling, Z. Phys. **C53** (1992) 629.

[39] OPAL Collab. M.Z.Akrawy et al., Phys. Lett. **B253** (1990) 511.

[40] OPAL Collab., K. Ackerstaff et al., Phys. Lett. **B389** (1996) 416.

[41] OPAL Collab., K. Ackerstaff et al., Z. Phys. **C74** (1997) 1.

[42] The LEP Experiments: ALEPH, DELPHI, L3 and OPAL, Nucl. Instrum. Methods **A378** (1996) 101.

[43] OPAL Collab., R. Akers et al., Z. Phys. **C61** (1994) 19.

[44] OPAL Collab., G. Alexander et al., Z. Phys. **C52** (1991) 175.

[45] D. Bardin et al., Nucl. Phys. Proc. Suppl. **37B** (1994) 148.

[46] HRS Collab., D. Bender et al., Phys. Rev. **D31** (1985) 1;
MAC Collab., E. Fernandez et al., Phys. Rev. **D31** (1985) 1537;
PLUTO Collab., C. Berger et al., Phys. Lett. **B81** (1979) 410;
CELLO Collab., H.J. Behrend et al., Phys. Lett.**B183** (1987) 400;
JADE Collab., W. Bartel et al., Phys. Lett. **B129** (1983) 145;
JADE Collab., W. Bartel et al., Phys. Lett.**B160** (1985) 337;
MARKJ Collab., B. Adeva et al., Phys. Rev. Lett. **50** (1983) 799;
MARKJ Collab., B. Adeva et al., Phys. Rev. **D34** (1986) 681;
TASSO Collab., R. Brandelik et al., Phys. Lett. **B113** (1982) 499;
TASSO Collab., M. Althoff et al., Phys. Lett. **B138** (1984) 441;
AMY Collab., T. Mori et al., Phys. Lett. **B218** (1989) 499;
TOPAZ Collab., I. Adachi et al., Phys. Rev. Lett. **60** (1988) 97;
VENUS Collab., H. Yoshida et al., Phys. Lett. **B198** (1987) 570;
TOPAZ Collab., K. Miyabayashi et al., Phys. Lett. **B347** (1995) 171.

[47] S. Kirsch and T. Riemann, Comput. Phys. Commun. **88** (1995) 89.

[48] LEP Electroweak Working Group and SLD Heavy Flavour Group, for the ALEPH, DELPHI, L3, OPAL, and SLD Collaborations, CERN-PPE/96-183, December 1996.

[49] TOPAZ Collab., I. Levine et al., Phys. Rev. Lett. **78** (1997) 424.

[50] M.E. Cage et al., IEEE Trans. Instrum. Meth. **38** (1989) 284.

[51] S. Banerjee and S.N. Ganguli, Z. Phys. **C57** (1993) 229.

[52] S. Eidelmann and F. Jegerlehner, Z. Phys. **C67** (1995) 585;
H. Burkhardt and B. Pietrzyk, Phys. Lett. **B356** (1995) 398;
see also
M.L. Swartz, Phys. Rev. **D53** (1996) 5268;
R. Alemany et al., LAL 97-02, February 1997.

[53] E. Eichten, K. Lane and M. Peskin, Phys. Rev. Lett. **50** (1983) 811.

[54] See for example *Contact interactions and new heavy bosons at HERA: a model independent analysis*, P. Haberl, F. Schrempp, H.U. Martyn, in Proceedings, Physics at HERA, **vol. 2**, (1991) 1133.

[55] F. Caravaglios, CERN-TH 97-104, `hep-ph/9706288`, June 1997;
V. Barger, K. Cheung, K. Hagiwara and D. Zeppenfeld, MADPH-97-991, `hep-ph/9703311`, March 1997;
N.Di Bartolomeo and M. Fabbrichesi, SISSA-34-97-EP, `hep-ph/9703375`, March 1997, submitted to Phys. Lett. B.

[56] G.J. Gounaris, D.T. Papadamou and F.M. Renard, THES-TP 97/02, `hep-ph/9703281`, March 1997, submitted to Phys. Rev. D.

[57] M. Martinez and R. Miquel, Z. Phys. **C53** (1992) 115.

[58] CDF Collab., F. Abe et al., Fermilab-Pub-97/171-E, May 1997, submitted to Phys. Rev. Lett..

[59] H1 Collab., T. Ahmed et al., Phys. Lett. **B353** (1995) 578.

[60] W. Buchmüller, R. Rückl, D. Wyler, Phys. Lett. **B191** (1987) 442;
J. L. Hewett, T. Rizzo, Phys. Rev. **D36** (1987) 3367.

[61] For an overview see for example H. Dreiner and G.G. Ross, Nucl. Phys. **B410** (1993) 188;
G.G. Ross, J.W.F. Valle, Phys. Lett. **B151** (1985) 375.

[62] J. Wess, J. Bagger, *Supersymmetry and Supergravity* (Princeton University Press, 1983);
H.P. Nilles, Phys. Rep. **110** (1984) 1;
H.E. Haber, G.E. Kane, Phys. Rep. **117** (1985) 75;
R. Barbieri, Riv. Nuovo Cim. **11** (1988) 1;
P. West, *Introduction to Supersymmetry and Supergravity* (World Scientific, 1986).

[63] CDF Collab., F. Abe et al., Phys. Rev. **D48** (1993) 3939;
CDF Collab., F. Abe et al., Phys. Rev. Lett. **75** (1995) 1012;
CDF Collab., F. Abe et al., Phys. Rev. Lett. **78** (1997) 2906;
D0 Collab., S. Abachi et al., Phys. Rev. Lett. **75** (1995) 3618;
D0 Collab., B. Abbott et al., Fermilab-Pub-97/252-E, `hep-ex 9707033`, July 1997, submitted to Phys. Rev. Lett..

[64] CDF Collab., F. Abe et al., Phys. Rev. **D56** (1997) 1357.

[65] D0 Collab., S. Abachi et al, Phys. Rev. Lett. **75** (1995) 618.

[66] G.R. Farrar, "e^+e^- Cross Section and Exclusion of Massless Electroweak Gauginos", RU-97-20, `hep-ph/9706393`, June 1997, submitted to Phys. Lett. B.

[67] OPAL Collab., G. Alexander et al., Phys. Lett. **B377** (1996) 181.

[68] OPAL Collab., K. Ackerstaff et al., Phys. Lett. **B389** (1996) 616.

[69] ALEPH Collab., D. Buskulic et al., Phys. Lett. **B373** (1996) 246;
DELPHI Collab., P. Abreu et al., Phys. Lett. **B382** (1996) 323 ;
L3 Collab., M. Acciarri et al., Phys. Lett. **B377** (1996) 289.

[70] CDF Collab., F. Abe et al., Phys. Rev. Lett. **76** (1996) 4307;
D0 Collab., S. Abachi et al., Phys. Rev. Lett. **76** (1996) 2228.

[71] A. Bartl, H. Fraas and W. Majerotto, Z. Phys. **C30** (1986) 441;
A. Bartl, H. Fraas and W. Majerotto, Z. Phys. **C41** (1988) 475;
A. Bartl, H. Fraas, W. Majerotto and B. Mösslacher, Z. Phys. **C55** (1992) 257.

[72] ALEPH Collab., D. Decamp et al., Phys. Rep. **216** (1992) 253.

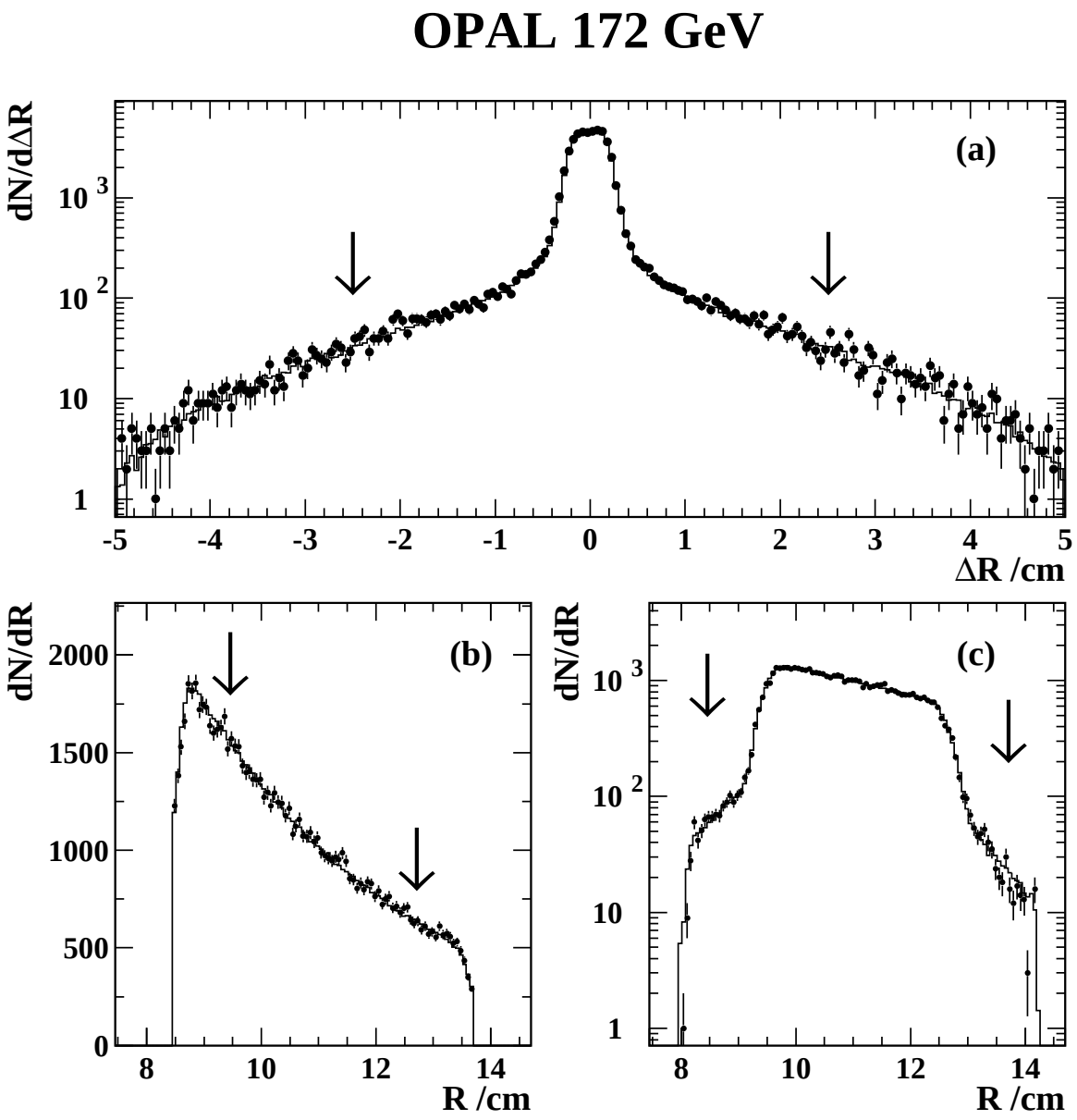

Figure 1: (a) The distribution of the difference in radial coordinate between the two clusters in Bhabha scattering events used for the silicon-tungsten luminosity measurement at 172 GeV. Distributions of the radial coordinates of clusters for (b) the 'narrow' side and (c) the 'wide' side calorimeter. Distributions are shown after all cuts except the acollinearity cut in (a) and the inner and outer radial acceptance cuts, on that side, in (b) and (c). Points show the data, while the histograms show the Monte Carlo expectation. The arrows show the positions of the cuts which define the acceptance.

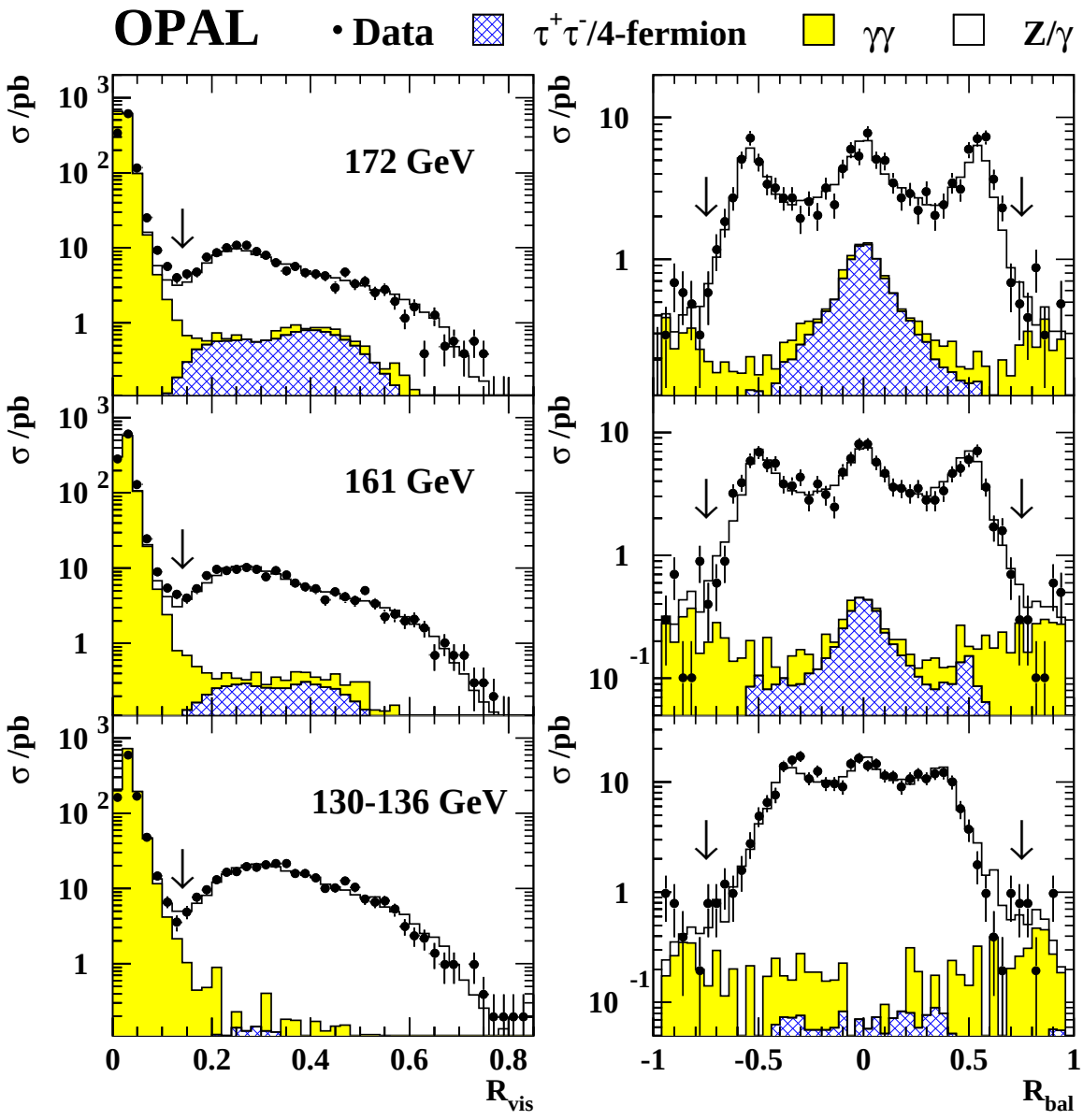

Figure 2: The distributions of $R_{\rm vis}$, the ratio of the total energy deposited in the electromagnetic calorimeter to the centre-of-mass energy, and $R_{\rm bal}$, the energy imbalance along the beam direction, for hadronic events at each energy. Distributions are shown after all event selection cuts except the cut on that quantity. The positions of the cuts are indicated by the arrows. Points show the data and histograms the Monte Carlo expectations, normalized to the integrated luminosity of the data, with light shading indicating background from two-photon events and cross-hatching indicating other backgrounds, mainly four-fermion (including WW) and $\tau^+\tau^-$ events.

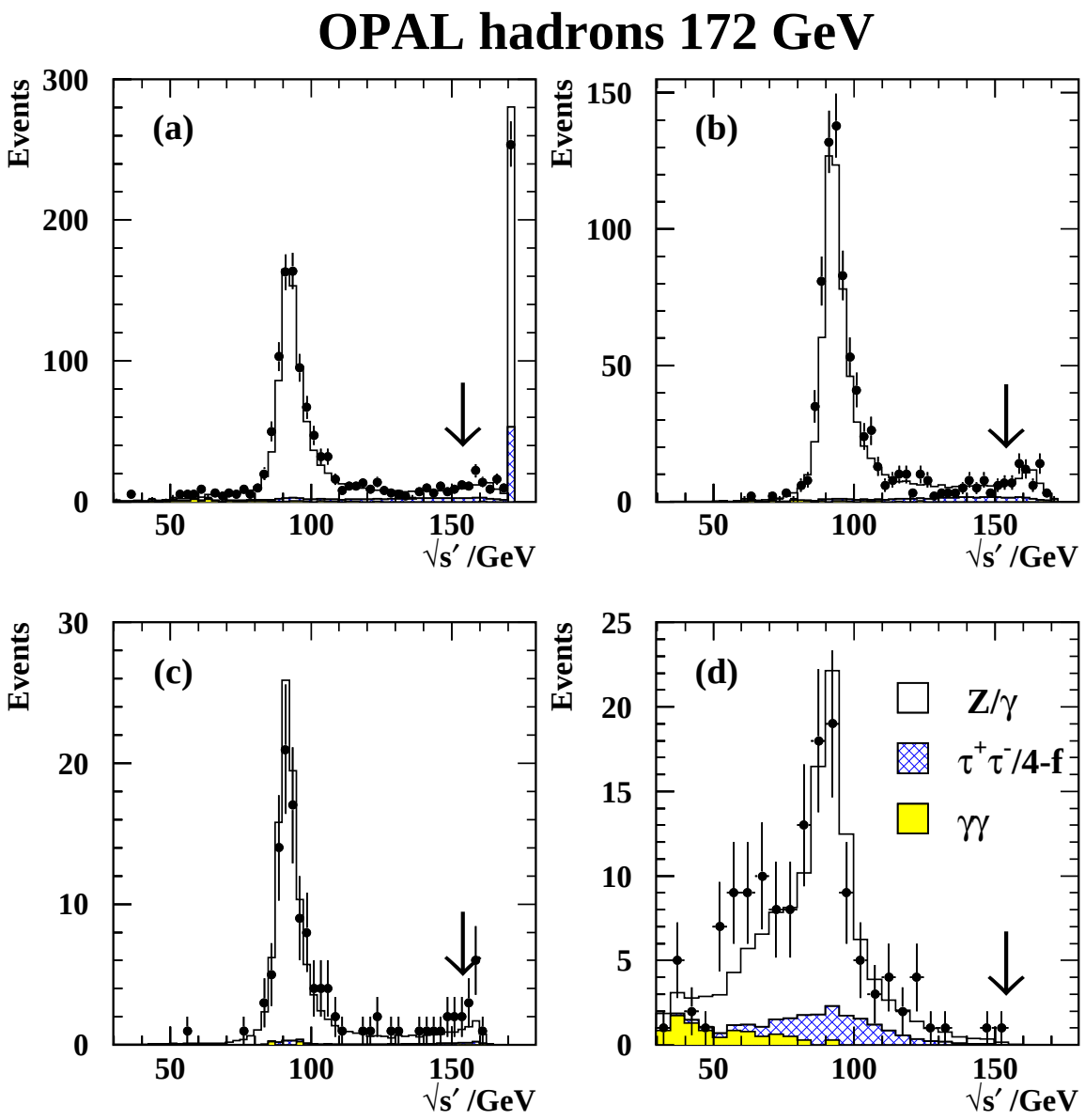

Figure 3: Distributions of effective centre-of-mass energy $\sqrt{s'}$ reconstructed for hadronic events at 172 GeV. The distributions are shown (a) for all events, (b) for events with one photon along the beam axis, (c) for events with one photon in the electromagnetic calorimeter and (d) for events with more than one photon. In each case the points show the data and the histogram the Monte Carlo prediction normalized to the luminosity of the data. The arrows indicate the position of the cut used to select 'non-radiative' events.

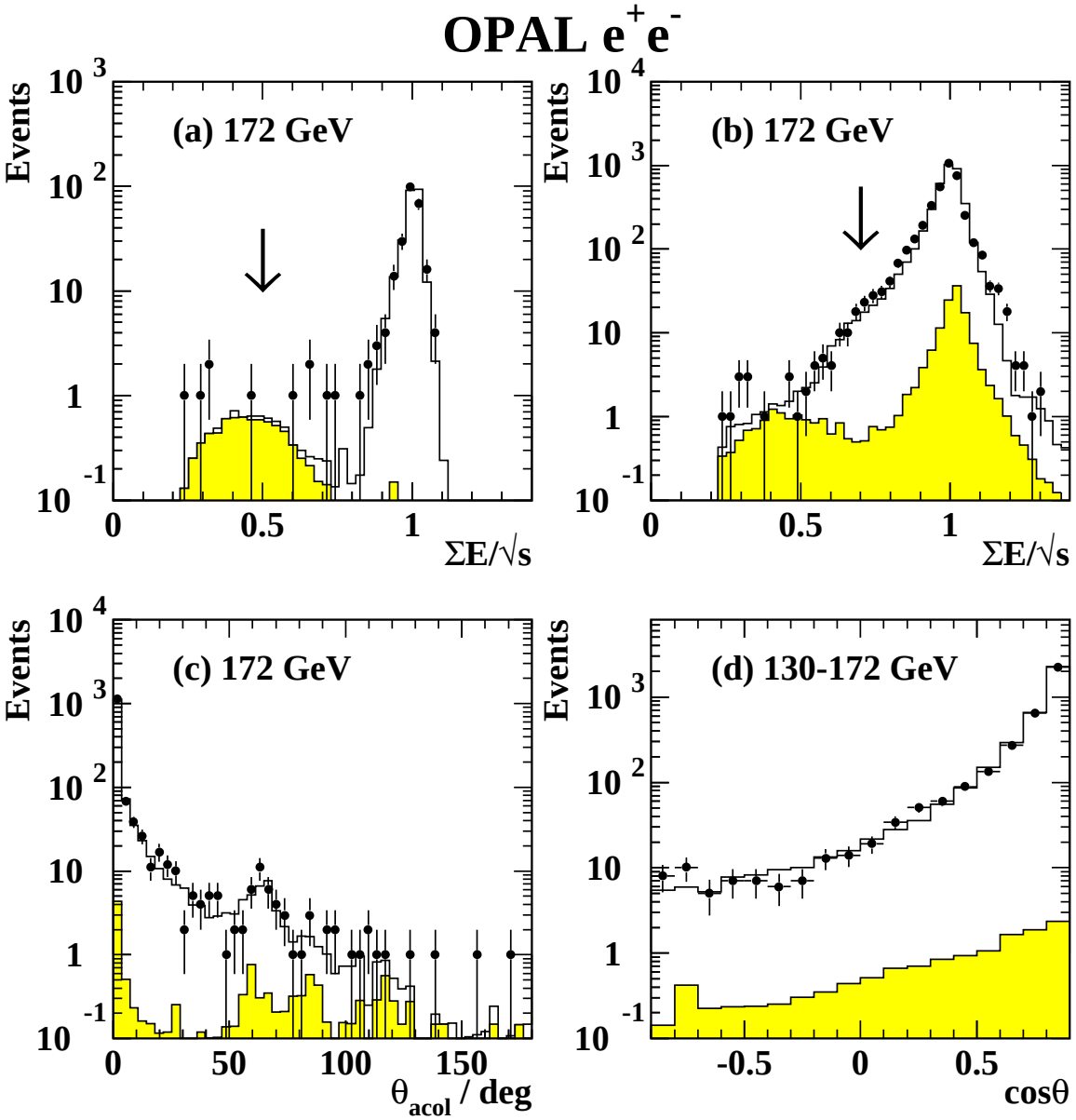

Figure 4: (a) The distribution of the ratio of total electromagnetic calorimeter energy to the centre-of-mass energy for $e^+e^- \to e^+e^-$ events in acceptance region B, $|\cos\theta_{e^-}| < 0.7$ and $\theta_{\rm acol} < 10°$, at 172 GeV. (b) The same distribution for the large acceptance selection, C, $|\cos\theta| < 0.96$ and $\theta_{\rm acol} < 10°$, at 172 GeV. Distributions are shown after all cuts except the one on total electromagnetic calorimeter energy; the arrows indicate the positions of the cuts on this quantity. (c) The acollinearity angle distribution for events satisfying the inclusive selection, in the acceptance region A, $|\cos\theta_{e^+}| < 0.9$, $|\cos\theta_{e^-}| < 0.9$, at 172 GeV. The cut on acollinearity angle has not been applied. (d) Observed distribution of $\cos\theta$ of the outgoing electron in e^+e^- events with $\theta_{\rm acol} < 10°$. All centre-of-mass energies have been summed for this plot. In each case, the points show the data and the histograms the Monte Carlo expectations, normalized to the integrated luminosity of the data, with the background contributions shaded.

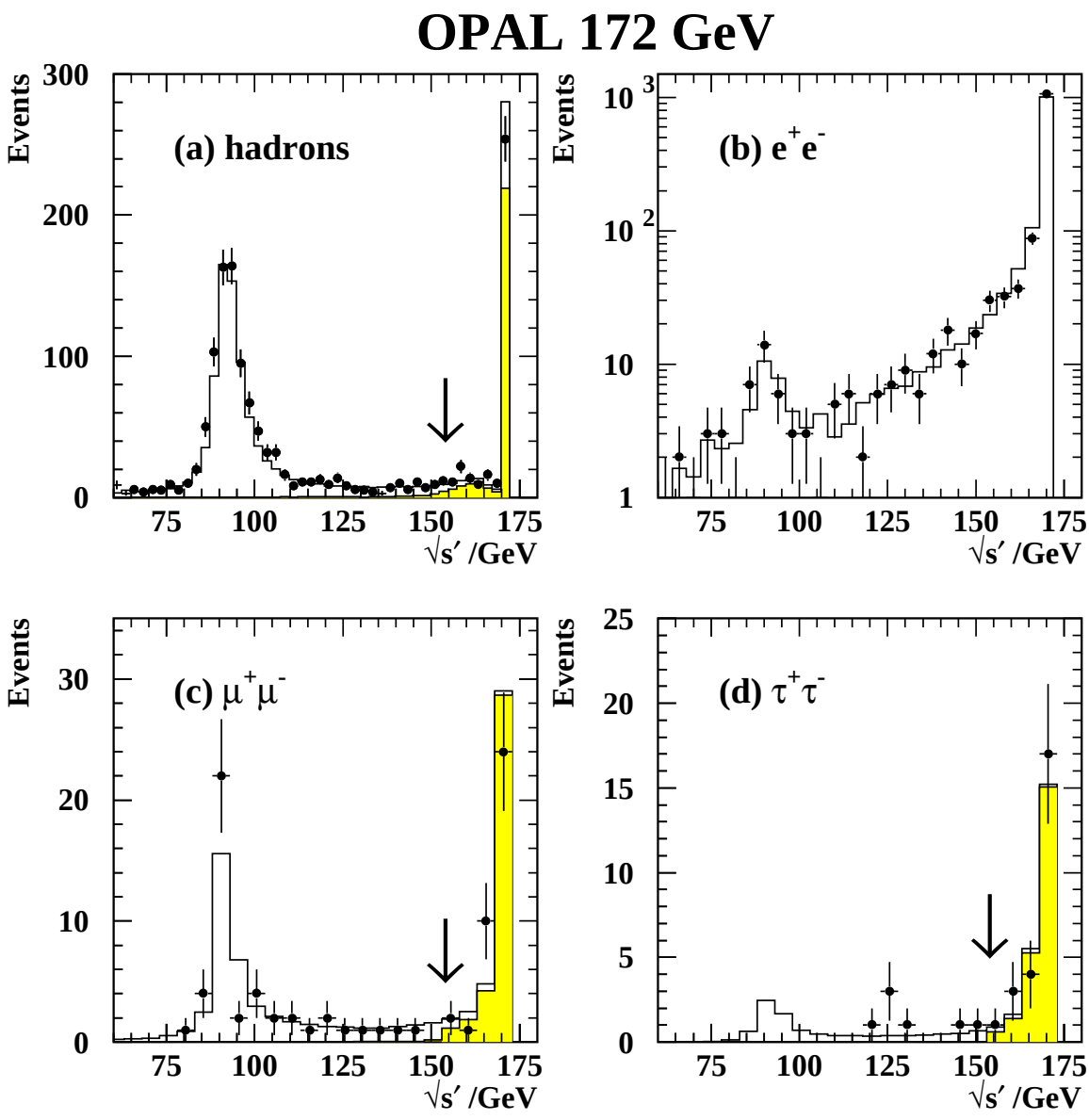

Figure 5: The distributions of $\sqrt{s'}$ for (a) hadronic events, (b) electron pair events with $|\cos\theta_{e^+}| < 0.9$, $|\cos\theta_{e^-}| < 0.9$ and $\theta_{\rm acol} < 170°$, (c) muon pair and (d) tau pair events at 172 GeV. In each case, the points show the data and the histogram the Monte Carlo prediction, normalized to the integrated luminosity of the data, with the contribution from events with true $s'/s > 0.8$ shaded in (a), (c) and (d). The arrows in (a), (c) and (d) show the position of the cut used to select 'non-radiative' events.

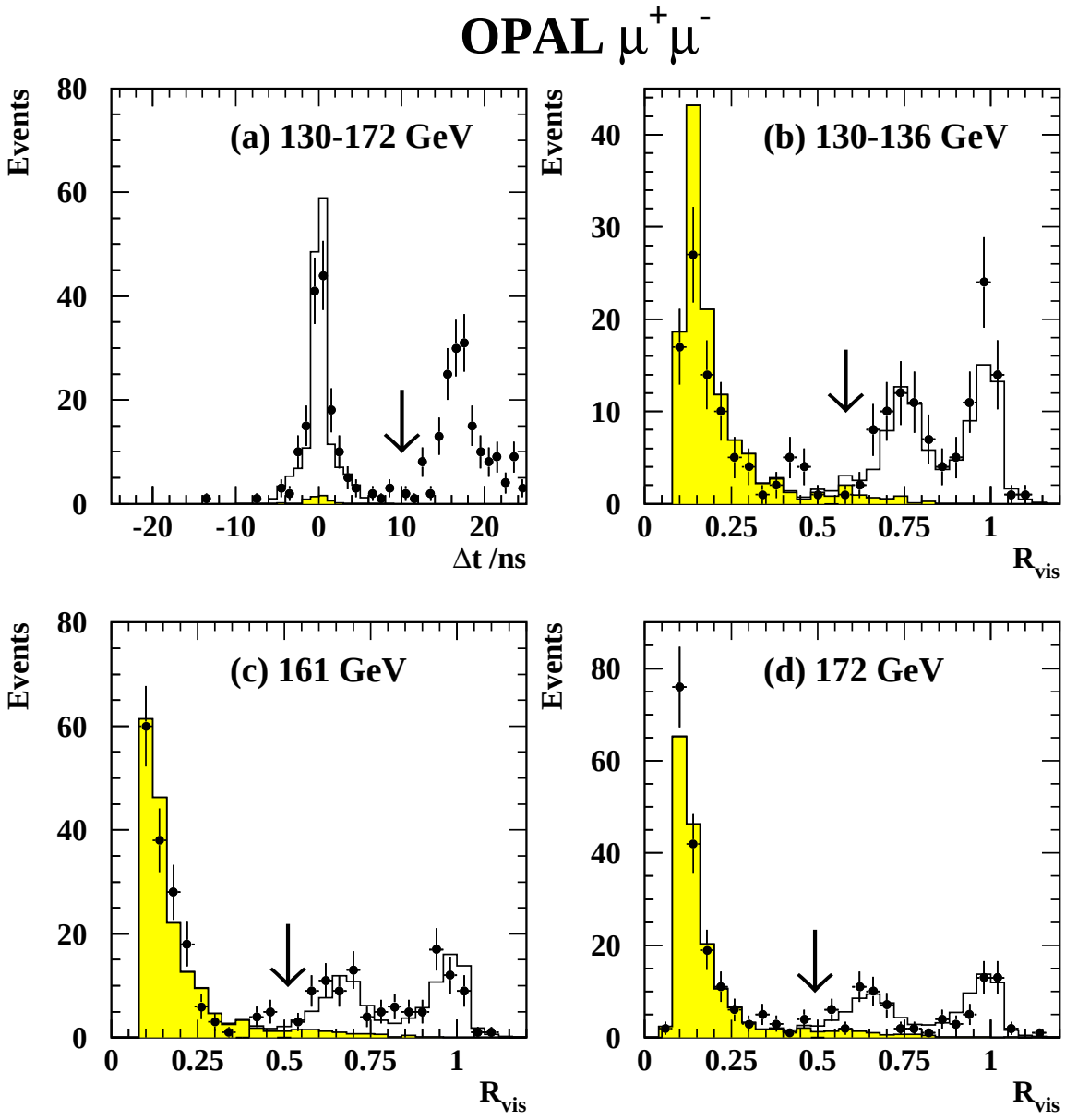

Figure 6: (a) The time difference between hits in back-to-back TOF counters for muon pair candidates; data from all energies have been included in this figure. (b) The distribution of the ratio of the visible energy to the centre-of-mass energy for muon pair events at 130–136 GeV. (c) and (d) show similar distributions at 161 and 172 GeV. In each case, the points show the data and the histogram the Monte Carlo expectation, normalized to the integrated luminosity of the data, with the background contribution shaded. The arrows show the positions of the cuts, which for the $R_{\rm vis}$ distributions are positioned 0.15 below the expected value for radiative return events where the photon is undetected.

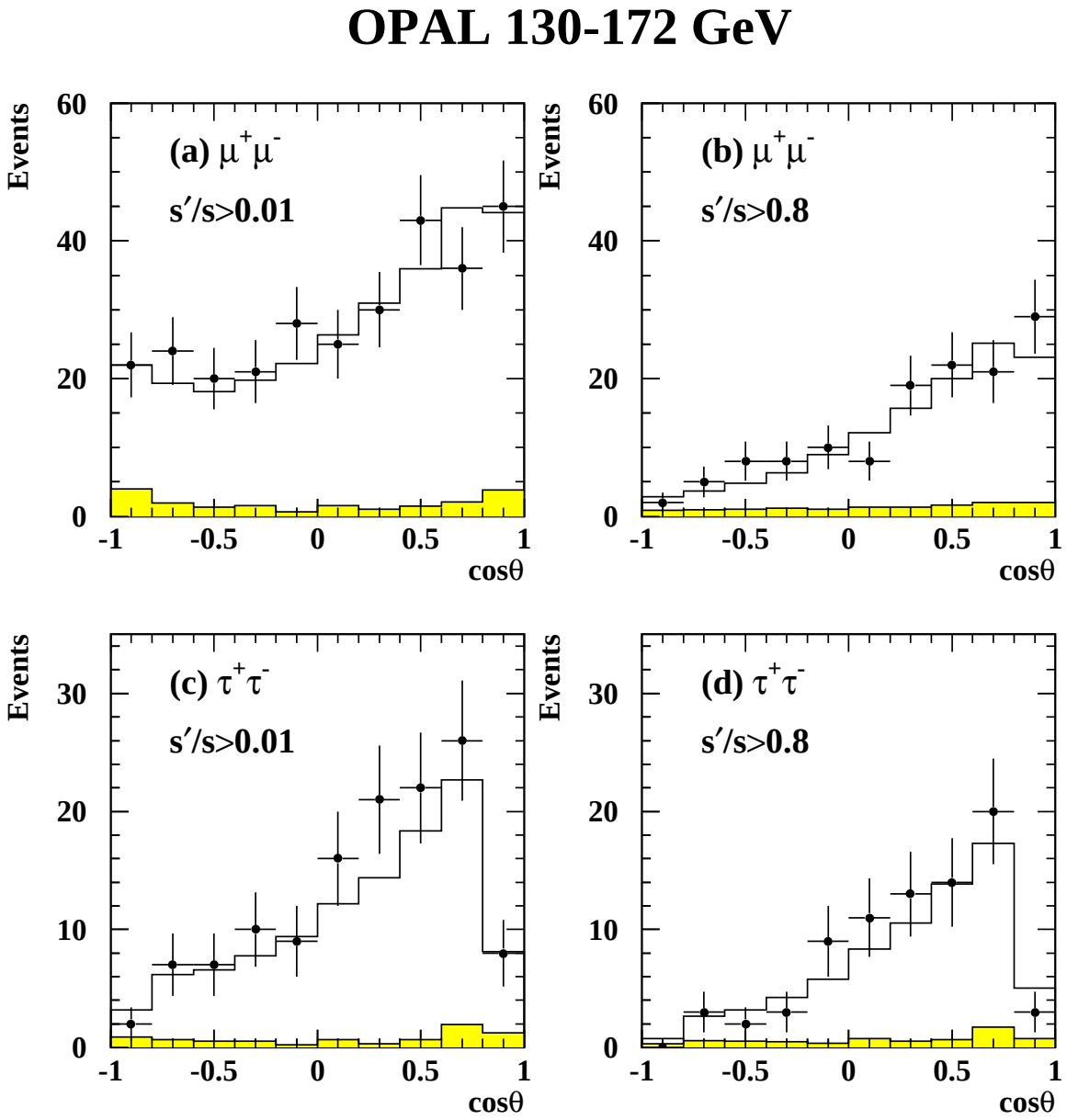

Figure 7: Observed distributions of $\cos\theta$ of the outgoing negative lepton in muon and tau pair events. (a) and (b) show muon pair events with $s'/s > 0.01$ and $s'/s > 0.8$ respectively, (c) and (d) tau pair events with $s'/s > 0.01$ and $s'/s > 0.8$. The points show data for all energies combined, while the histograms show the Monte Carlo expectations, formed by summing the predictions at each energy normalized to the measured integrated luminosity values. The background contributions (including feedthrough from lower s' in the $s'/s > 0.8$ cases) are shaded.

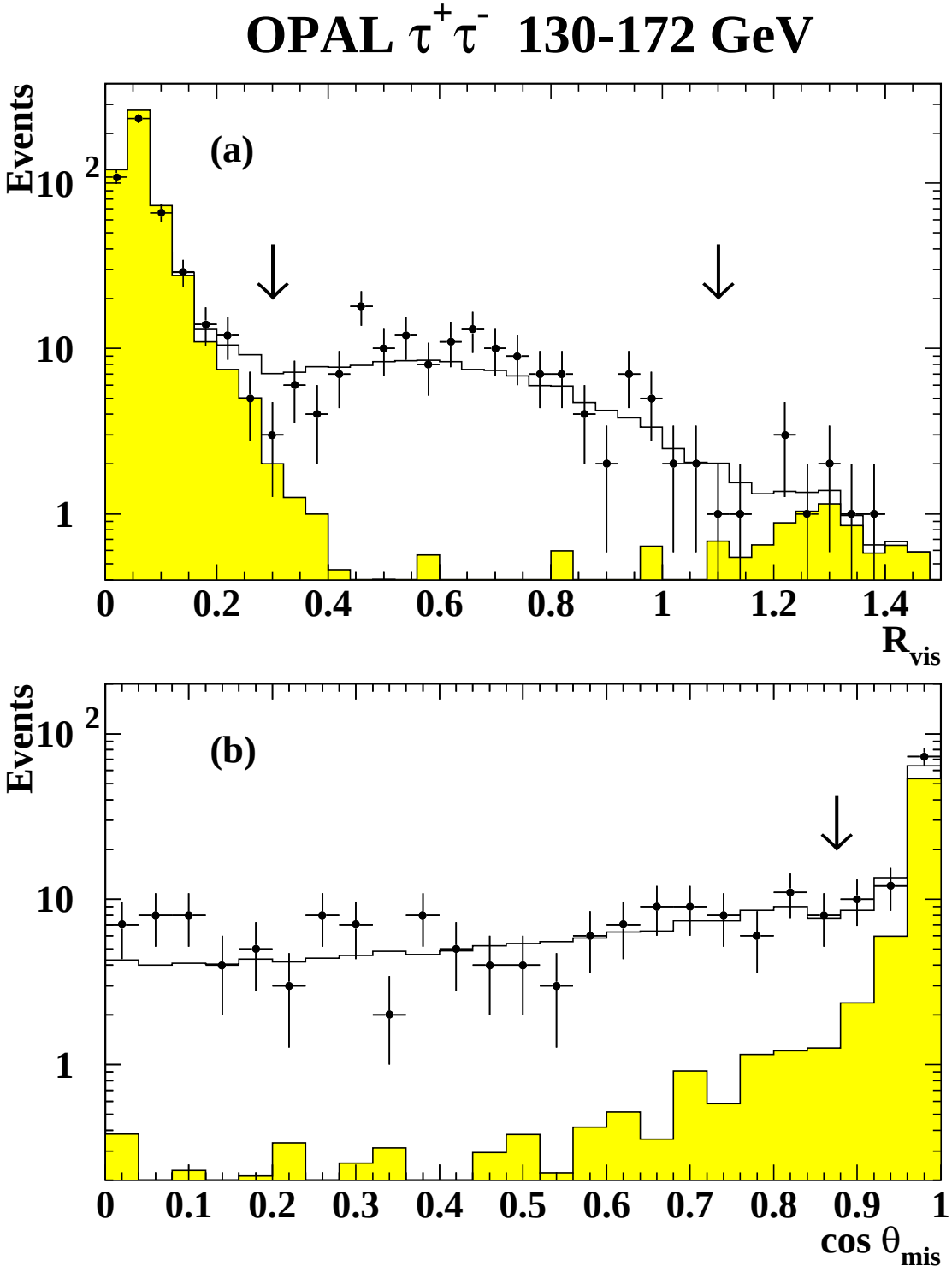

Figure 8: (a) The distribution of the ratio of the visible energy to the centre-of-mass energy for tau pair events. Note that visible energy here is defined as the scalar sum of track momenta plus electromagnetic calorimeter energy, with no correction for double counting. (b) Distribution of $\cos\theta$ of the missing momentum vector, calculated using electromagnetic clusters, for tau pair candidates. Data from all energies have been included in this figure. In each case, the points show the data and the histogram the Monte Carlo expectation, normalized to the integrated luminosity of the data, with the background contribution shaded. The arrows show the positions of the cuts.

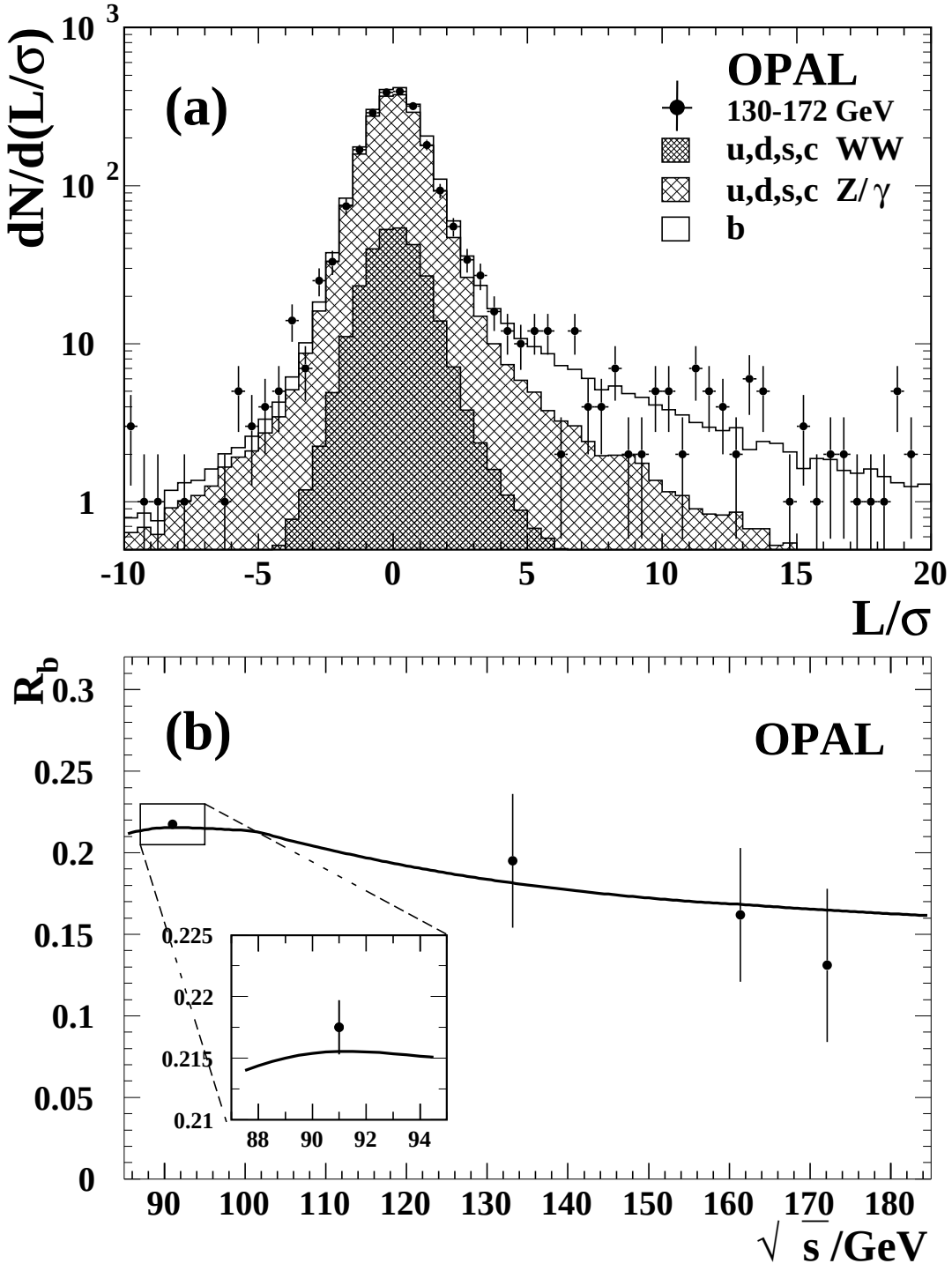

Figure 9: (a) Decay length significance distribution for all centre-of-mass energies combined. The points show the data, the histogram the Monte Carlo prediction. (b) $R_{\rm b}$ as a function of the centre-of-mass energy. The points show the measurements presented here, and the value [41] obtained on the Z peak. The errors are statistical and systematic, summed in quadrature. The solid line is the ZFITTER prediction for $s'/s > 0.8$.

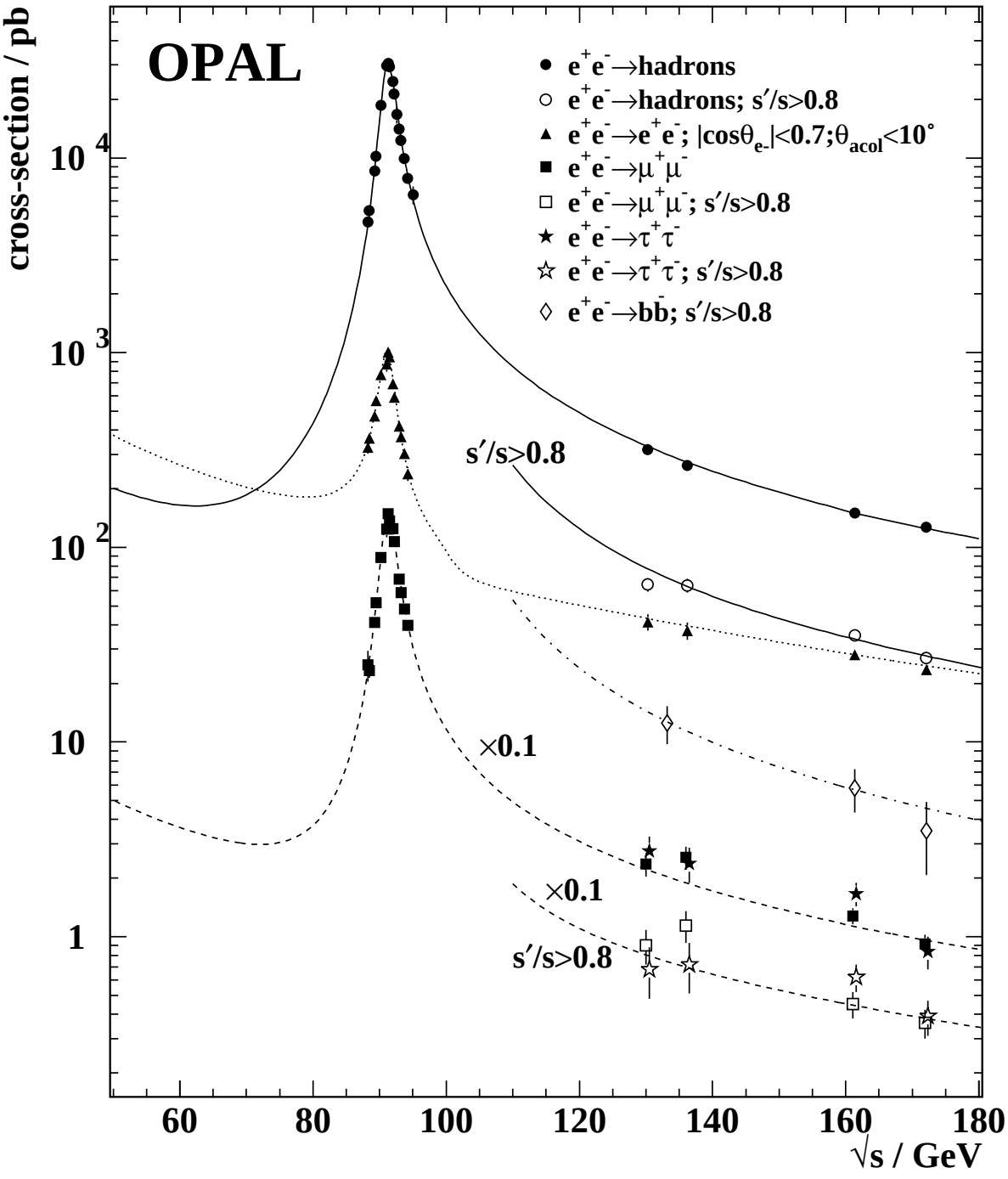

Figure 10: Measured total cross-sections ($s'/s > 0.01$) for different final states at lower energies [36, 43, 44], and this analysis. Cross-section measurements for hadrons, $b\bar{b}$, muon and tau pairs for $s'/s > 0.8$ from this analysis are also shown. The cross-sections for $\mu^+\mu^-$ and $\tau^+\tau^-$ production have been reduced by a factor of ten for clarity. The curves show the predictions of ZFITTER for hadronic (solid), $b\bar{b}$ (dot-dashed), $\mu^+\mu^-$ and $\tau^+\tau^-$ (dashed) final states and that of ALIBABA for the e^+e^- final state (dotted).

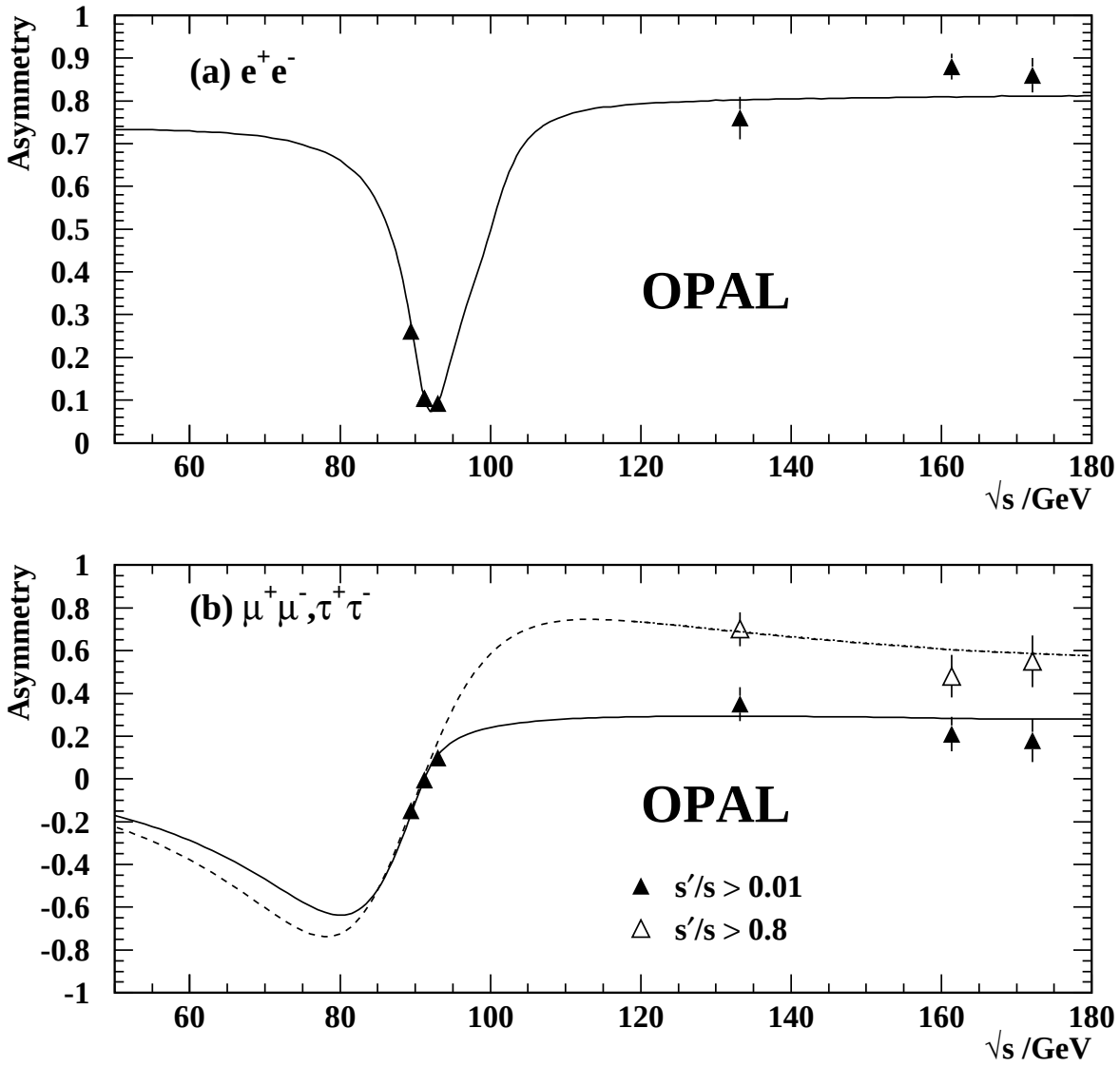

Figure 11: (a) Measured forward-backward asymmetry for electron pairs with $|\cos\theta_{e^-}| < 0.7$ and $\theta_{\rm acol} < 10^\circ$, as a function of $\sqrt{s}$. The curve shows the prediction of ALIBABA. (b) Measured asymmetries for all ($s'/s > 0.01$) and non-radiative ($s'/s > 0.8$) samples as functions of $\sqrt{s}$ for $\mu^+\mu^-$ and $\tau^+\tau^-$ events (combined). The curves show ZFITTER predictions for $s'/s > 0.01$ (solid) and $s'/s > 0.8$ (dotted), as well as the Born-level expectation without QED radiative effects (dashed). The expectation for $s'/s > 0.8$ lies extremely close to the Born curve, such that it appears indistinguishable on this plot.

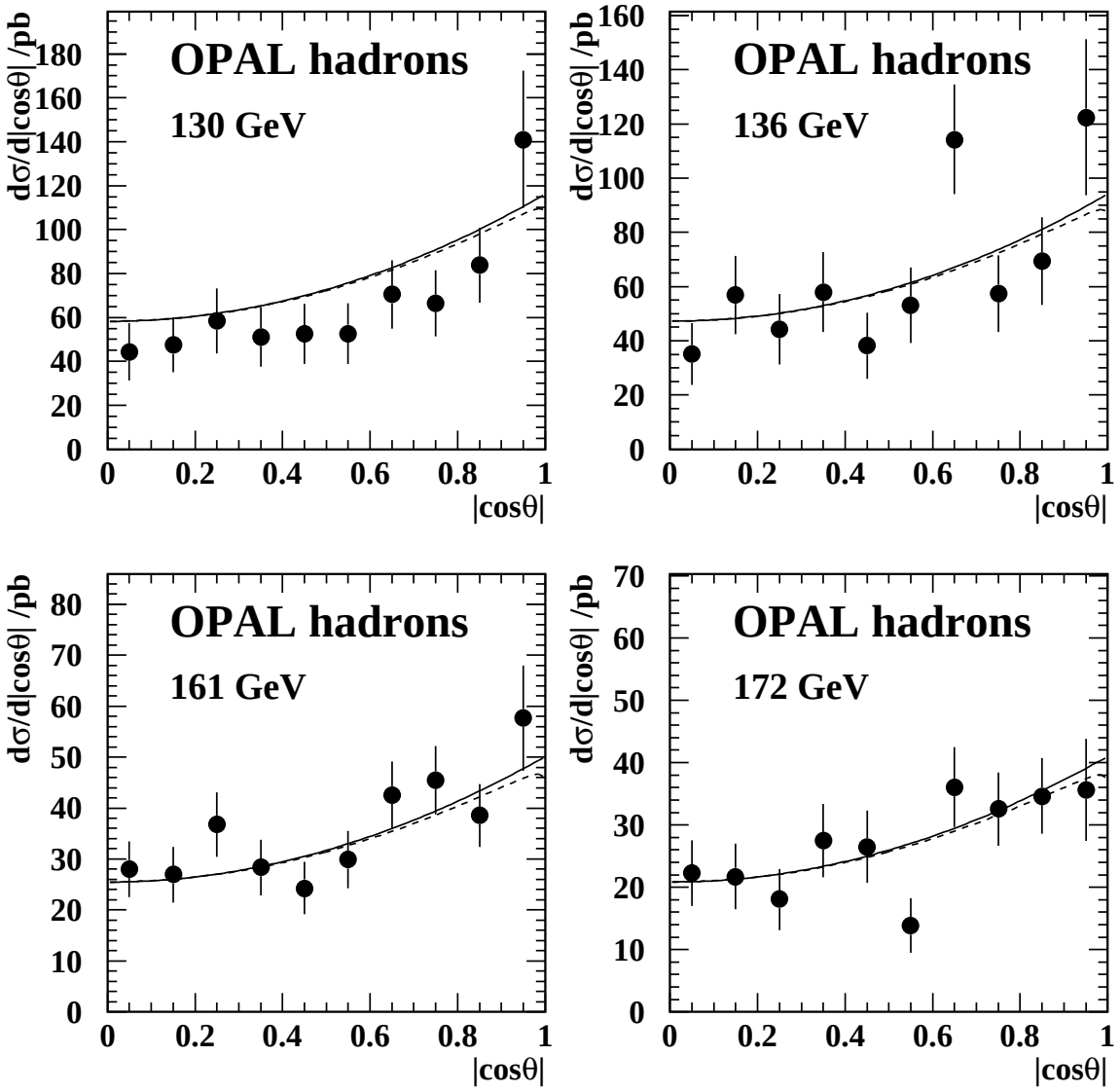

Figure 12: Angular distributions for hadronic events with $s'/s > 0.8$. The data points show the measurements corrected to the direction of the primary quark/antiquark, and corrected to no interference between initial- and final-state radiation. The curves show the predictions of the ZFITTER program with no interference between initial- and final-state radiation (solid) and with interference (dashed).

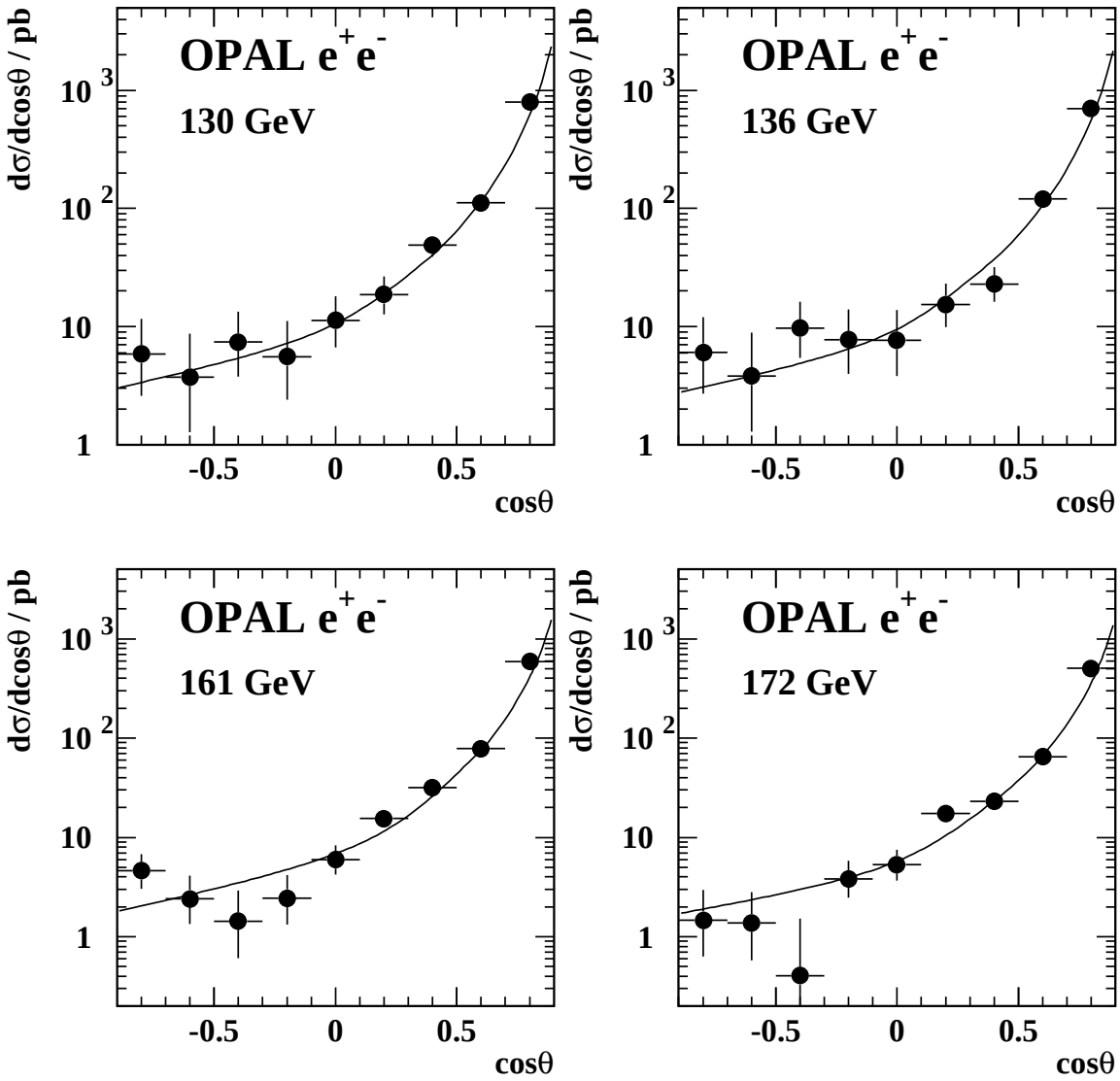

Figure 13: Angular distributions for e^+e^- events with $\theta_{\rm acol} < 10°$. The points show the data, the curves the predictions of the ALIBABA program.

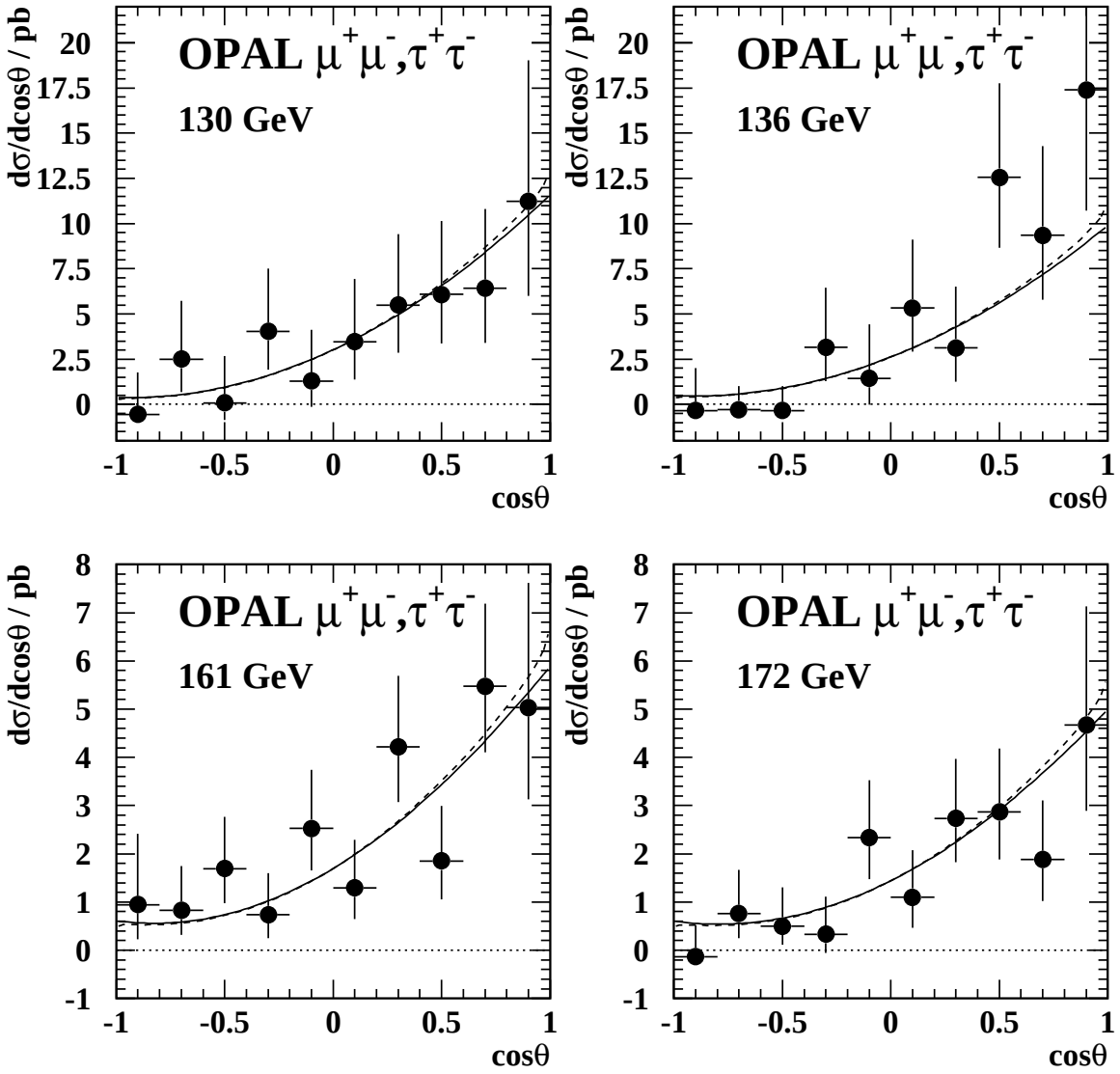

Figure 14: Angular distributions for $\mu^+\mu^-$ and $\tau^+\tau^-$ events with $s'/s > 0.8$. The data points show the measurements, which have been formed as a weighted average of the $\mu^+\mu^-$ and $\tau^+\tau^-$ distributions corrected to no interference between initial- and final-state radiation. The curves show the predictions of the ZFITTER program with no interference between initial- and final-state radiation (solid) and with interference (dashed).

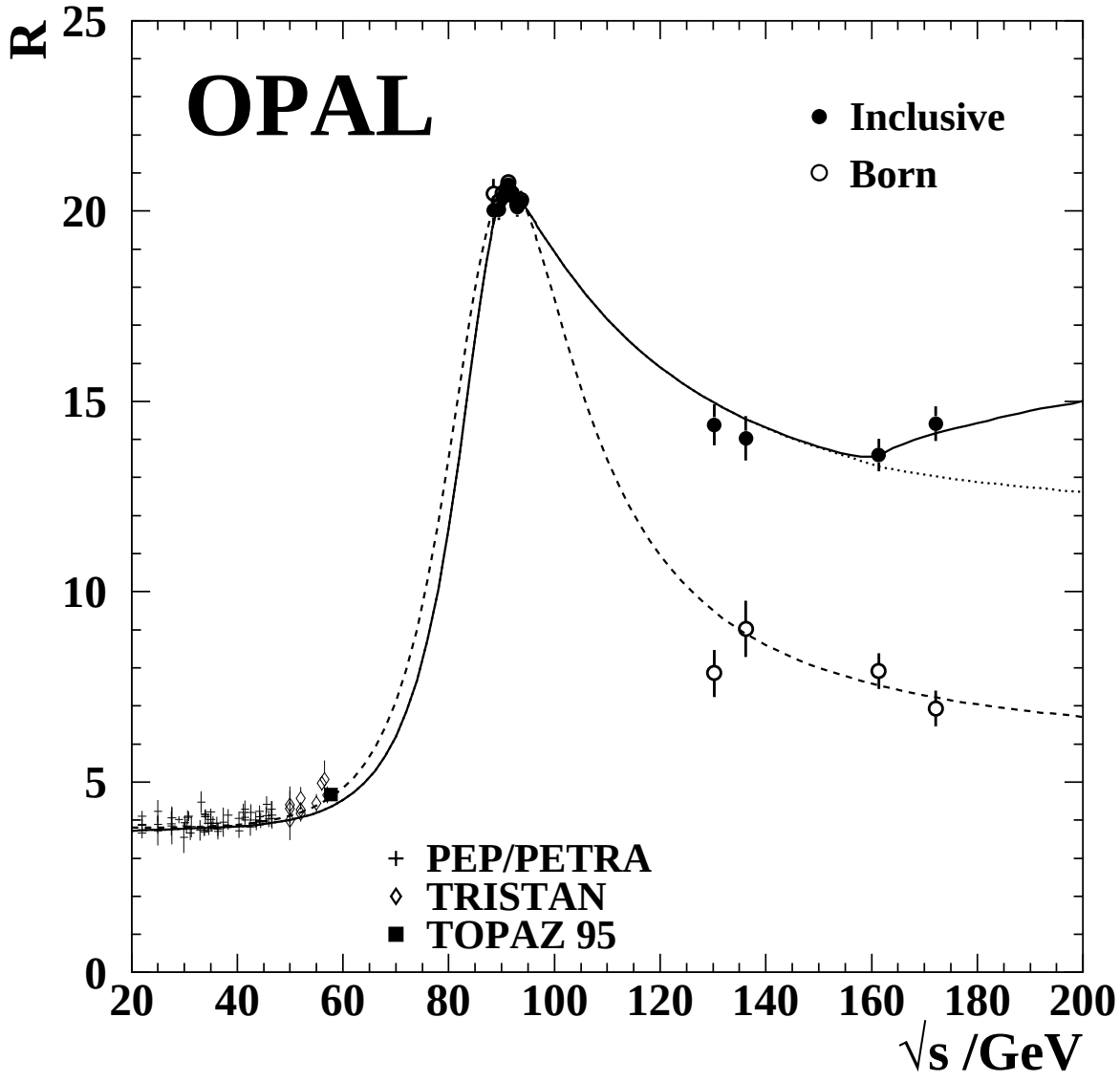

Figure 15: Ratio of measured hadronic cross-sections to theoretical muon pair cross-sections as a function of centre-of-mass energy. Values are shown for the inclusive cross-section, $\sigma(\mathrm{q\overline{q}X})$ and for the Born level cross-section, as described in the text. The dotted and dashed curves show the predictions of ZFITTER for these cross-sections, while the solid curve also includes the contributions from W-pairs calculated using GENTLE and from Z-pairs calculated using FERMISV. Measurements at lower energies are from references [36,43,44,46].

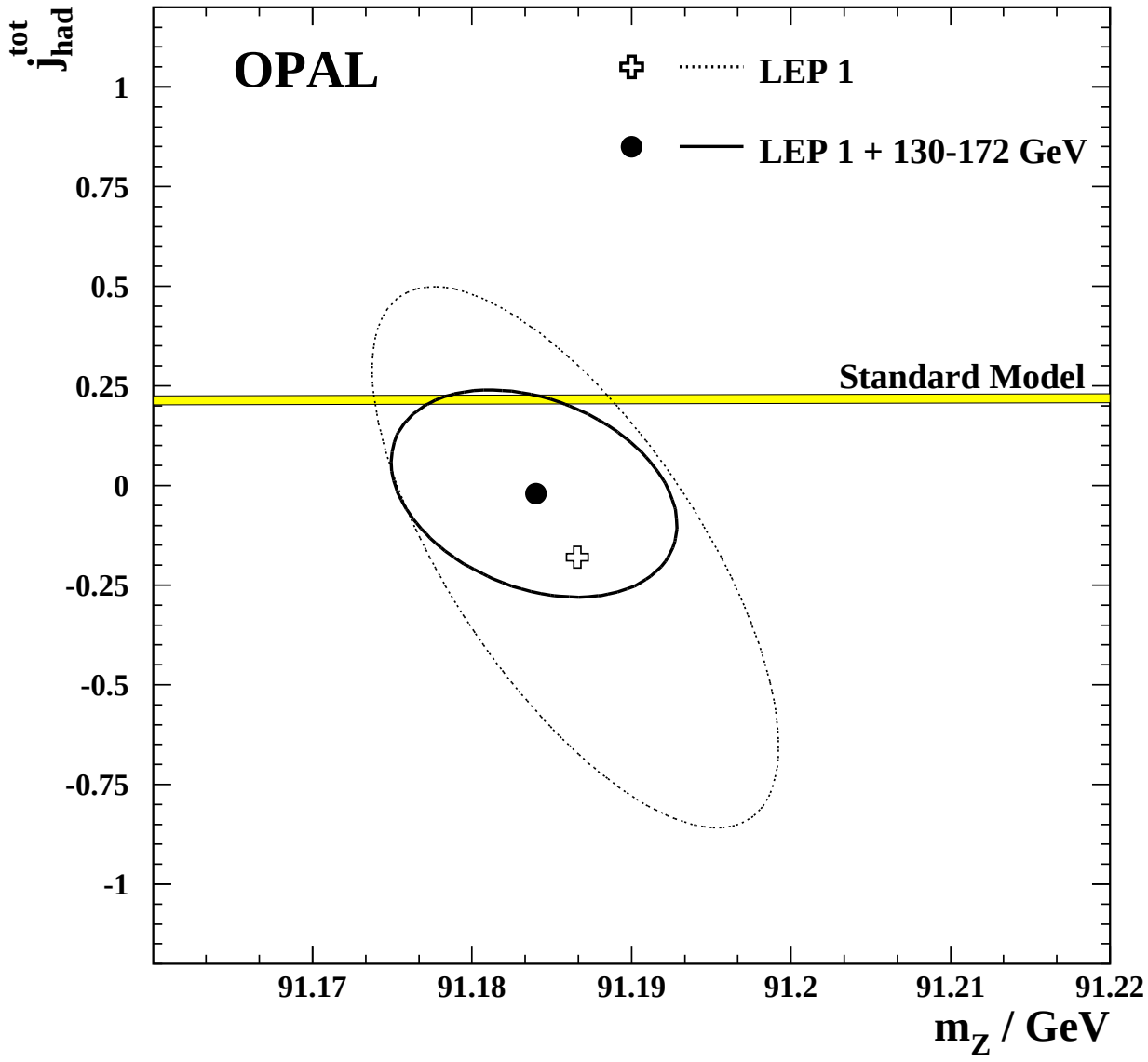

Figure 16: Central values and one standard deviation contours (39% probability content) in the j^{tot}_{had} vs. m_Z plane resulting from model-independent fits to the OPAL data samples described in section 4.1. The horizontal band shows the Standard Model expectation $j^{tot}_{had} = 0.216 \pm 0.011$ for a top quark mass of 175±5 GeV and a Higgs mass range of 70-1000 GeV.

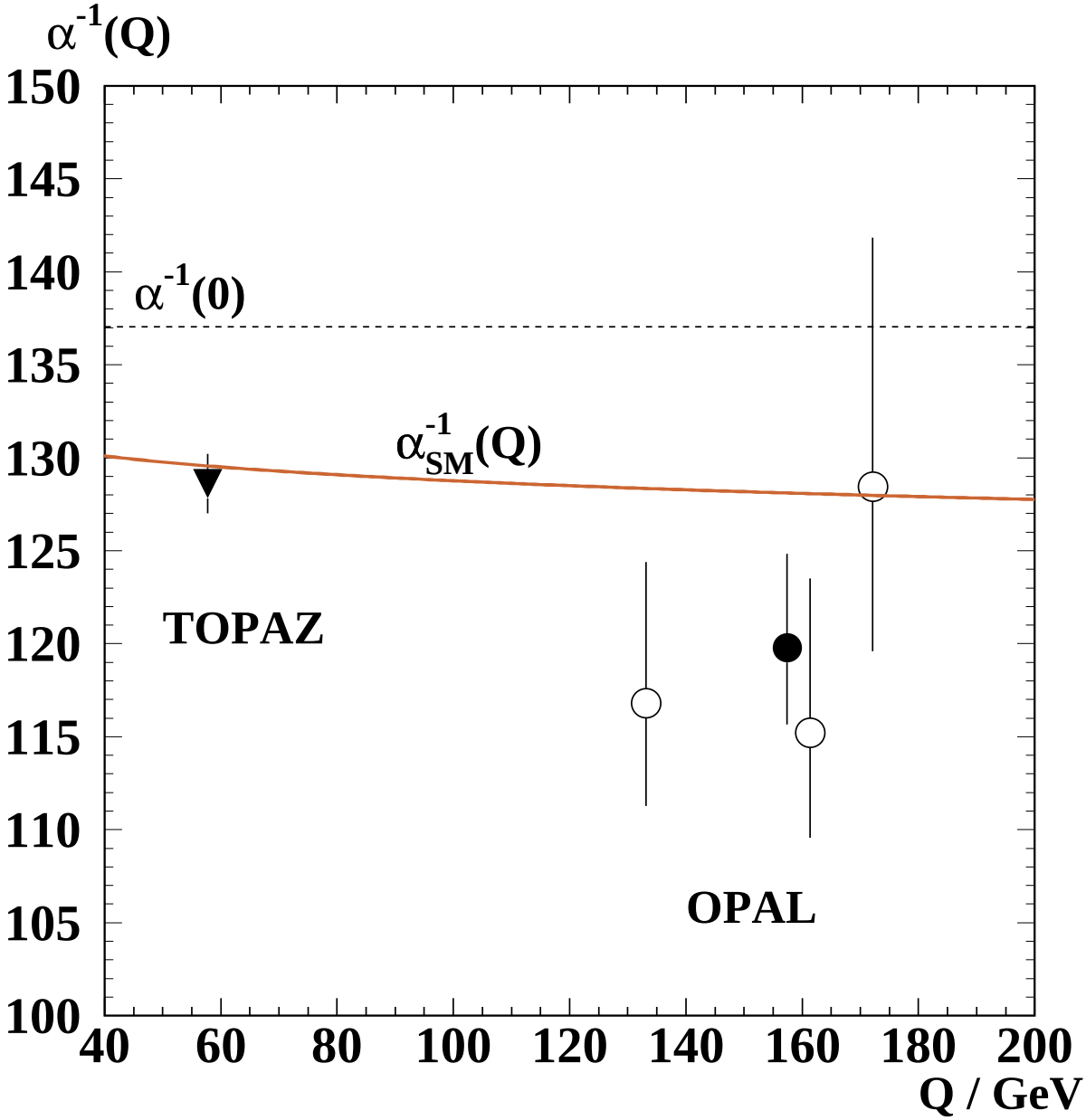

Figure 17: Fitted values of $1/\alpha_{\rm em}$ as a function of Q, which is $\sqrt{s}$ for the OPAL fits. The open circles show the results of the fits at each centre-of-mass energy, the closed circle the result of the combined fit. The value obtained by the TOPAZ experiment [49] is also shown for comparison. The solid line shows the Standard Model expectation, with the thickness representing the uncertainty, while the value of $1/\alpha_{\rm em}(0)$ is shown by the dashed line.

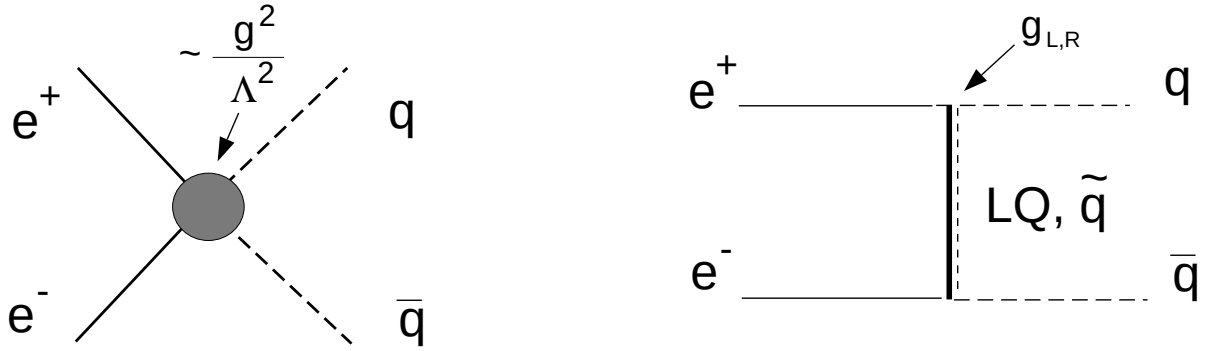

Figure 18: Feynman diagram representing a generic contact interaction (left) and the exchange of a leptoquark or a squark in a t-channel diagram in an e^+e^- collision.

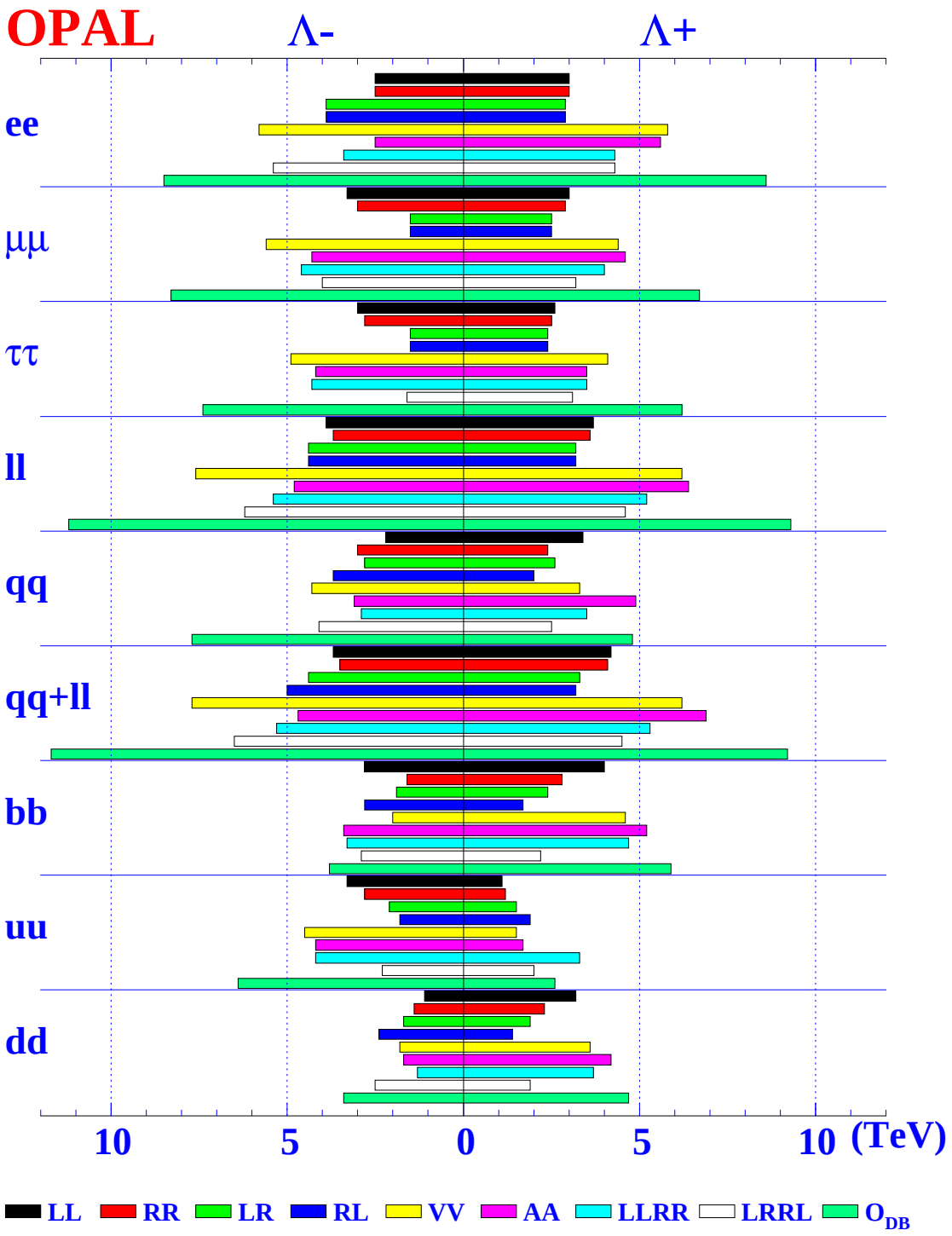

Figure 19: 95% confidence level limits on the energy scale Λ resulting from the contact interaction fits. For each channel, the bars from top to bottom indicate the results for models LL to $\overline{\mathcal{O}}_{\rm DB}$ in the order given in the key.

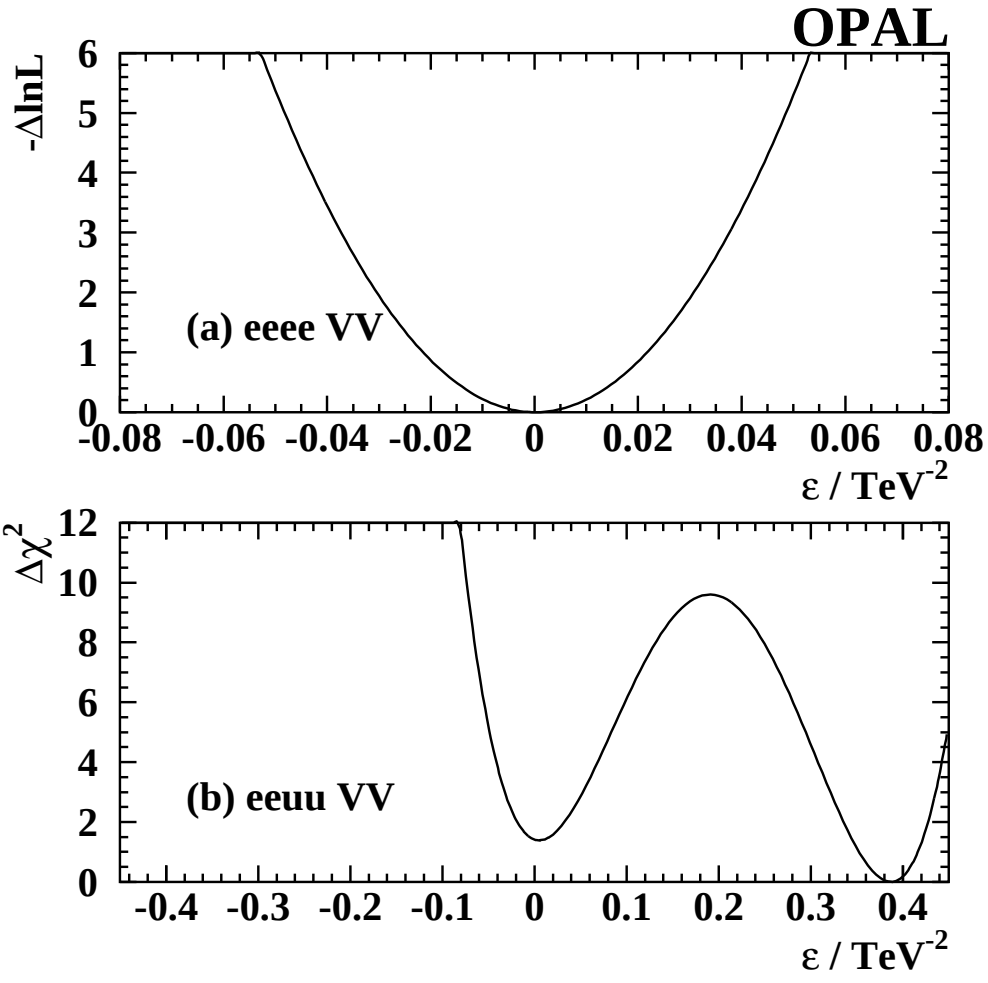

Figure 20: (a) Negative log likelihood curve for the contact interaction fit to the e^+e^- angular distribution for the VV model. (b) χ^2 curve for the contact interaction fit to the hadronic cross-section, assuming coupling to only one up-type quark, for the same model.

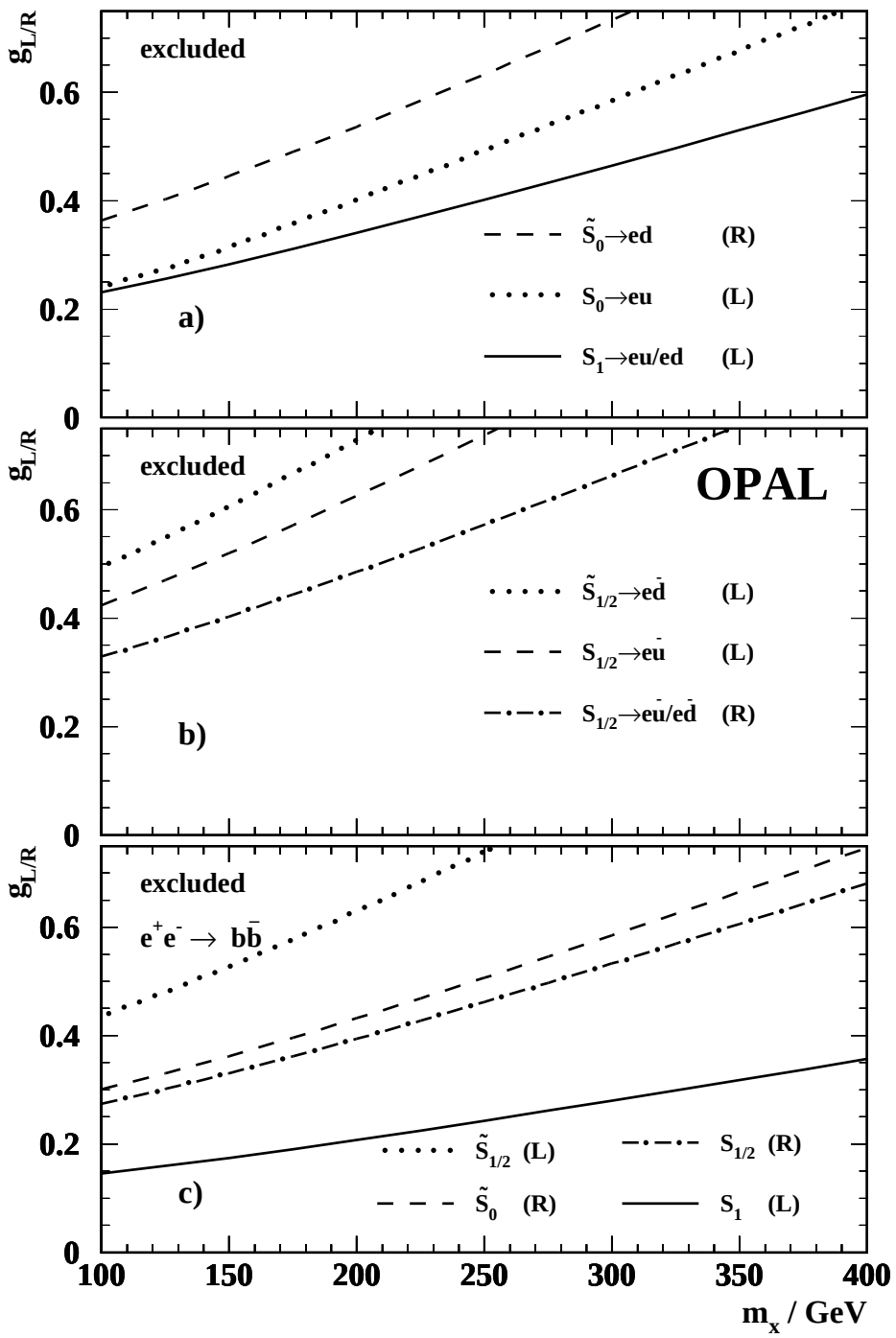

Figure 21: 95% confidence exclusion limits on g_L or g_R as a function of m_X, for various possible scalar leptoquarks. (a) and (b) show limits on leptoquarks coupling to a single quark family, derived from the hadronic cross-sections. (c) shows limits on leptoquarks coupling to b quarks only, derived from the $b\bar{b}$ cross-sections. The excluded regions are above the curves in all cases. The letter in parenthesis after the different leptoquark types indicates the chirality of the lepton involved in the interaction. The limits on the S_0 and $\tilde{S}_{1/2}$ leptoquarks can be interpreted as those on R-parity violating $\tilde{d}_R$ and $\tilde{u}_L$ squarks respectively.

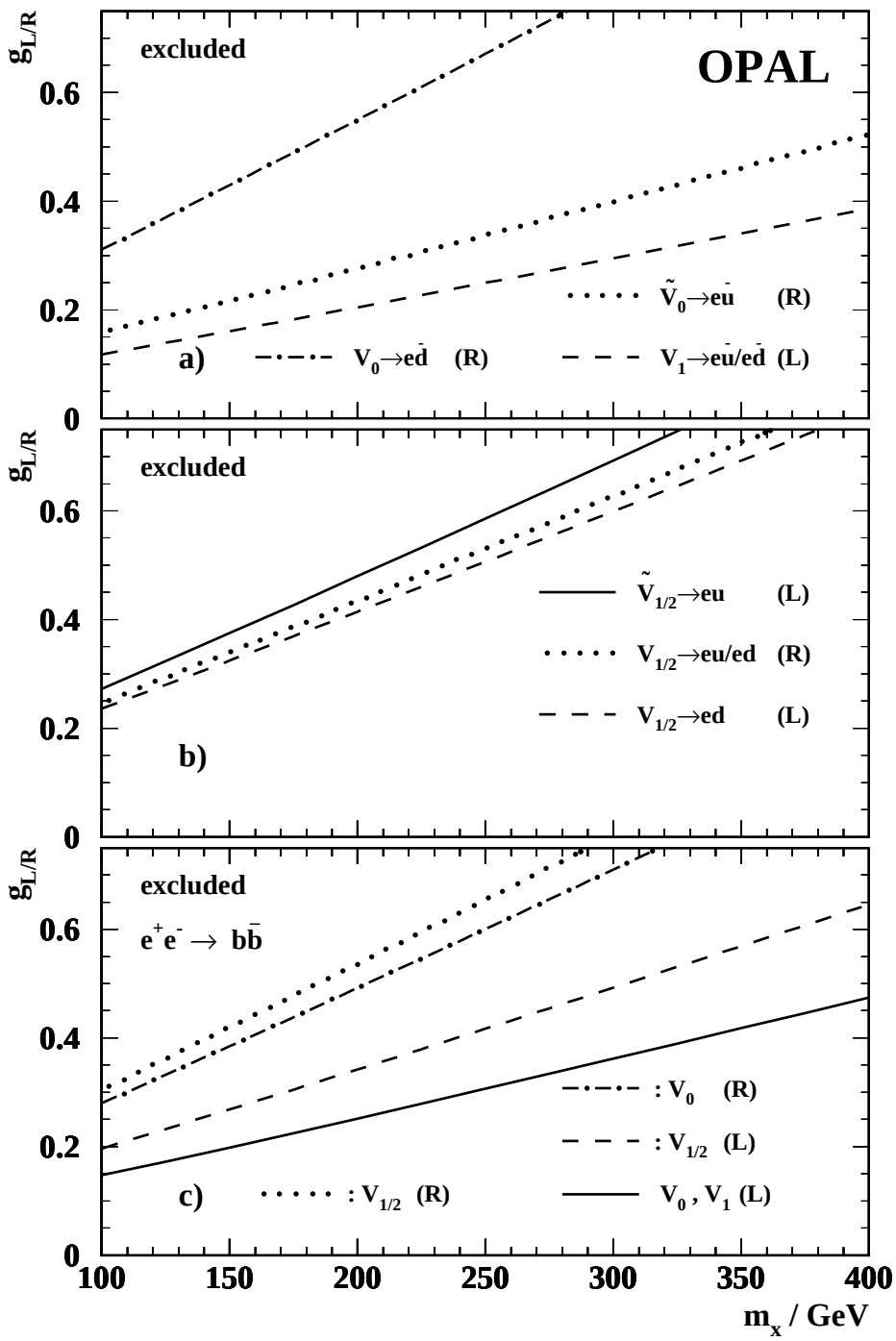

Figure 22: 95% confidence exclusion limits on g_L or g_R as a function of m_X, for various possible vector leptoquarks. (a) and (b) show limits on leptoquarks coupling to a single quark family, derived from the hadronic cross-sections. (c) shows limits on leptoquarks coupling to b quarks only, derived from the $b\bar{b}$ cross-sections. The excluded regions are above the curves in all cases. The letter in parenthesis after the different leptoquark types indicates the chirality of the lepton involved in the interaction.

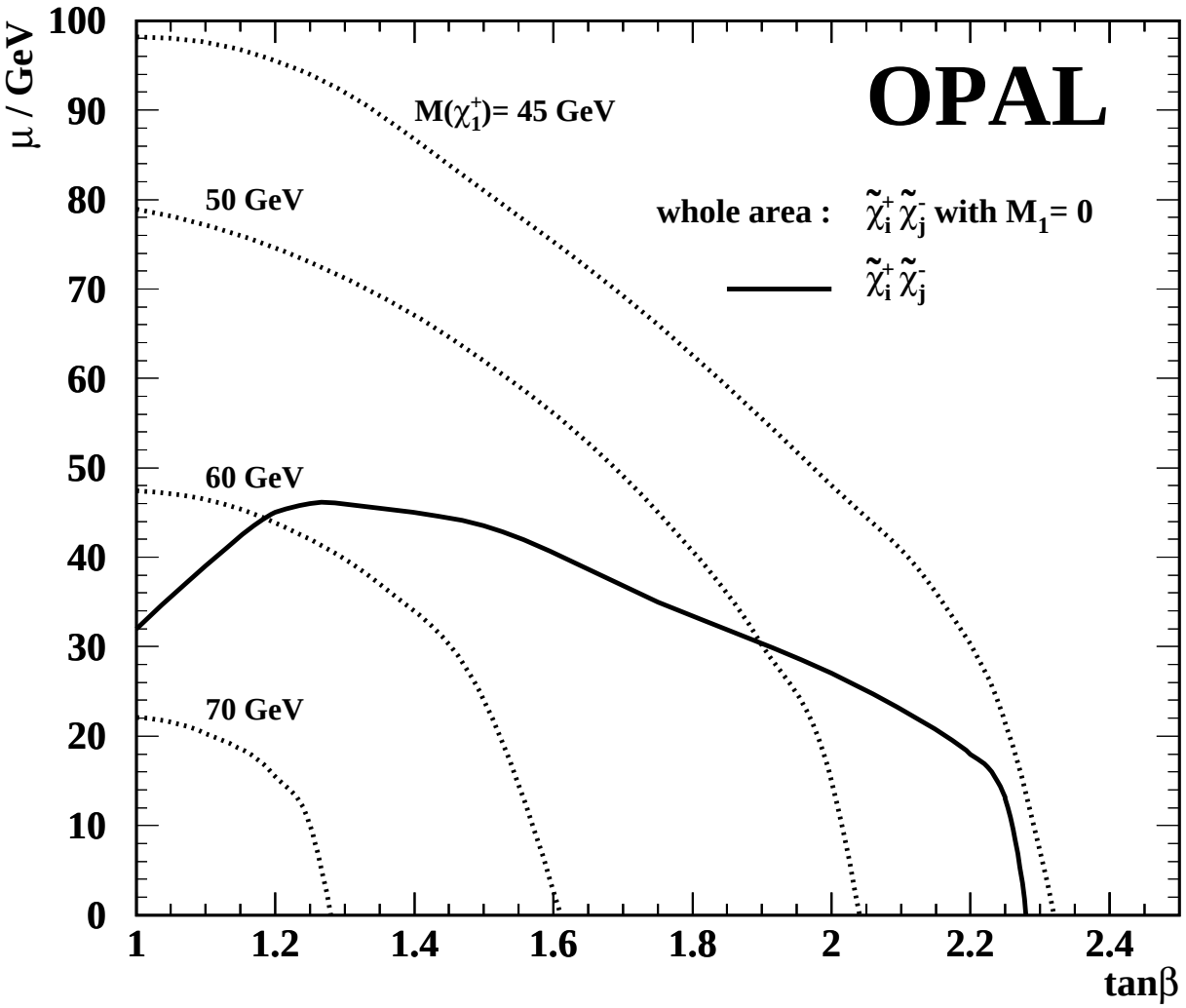

Figure 23: The 95% confidence level lower limit of μ as a function of $\tan\beta$ calculated assuming $M_2 = M_3 = 0$, with no restriction on M_1. The region above the solid curve is excluded. The sneutrino mass is assumed to be larger than the current limit of 43 GeV, and the decay branching fraction of $\tilde{\chi}^{\pm} \to q\overline{q}'\tilde{g}$ is assumed to be 100%. The contours for chargino masses $m_{\tilde{\chi}^{\pm}} = 45$ GeV, 50 GeV, 60 GeV and 70 GeV are also shown with dotted lines. With the additional restriction $M_1 = 0$, the existence of light gluinos is excluded everywhere in the μ–$\tan\beta$ plane.